DEVELOPMENT OF EXPERIMENTAL STATION AT THE SIAM PHOTON LABORATORY FOR ULTRA-THIN MAGNETIC FILMS RESEARCH

Moragote Buddhakala

A Thesis Submitted in Partial Fulfillment of the Requirements
for the Degree of Doctor of Philosophy in Physics
Suranaree University of Technology
Academic Year 2007

การพัฒนาสถานีทดลองด้านโฟโตอิมิสชัน ณ ห้องปฏิบัติการแสงสยาม สำหรับงานวิจัยแผ่นฟิล์มแม่เหล็กบาง

นายมรกต พุทธกาล

วิทยานิพนธ์นี้เป็นส่วนหนึ่งของการศึกษาตามหลักสูตรปริญญาวิทยาศาสตรดุษฎีบัณฑิต
สาขาวิชาฟิสิกส์
มหาวิทยาลัยเทคโนโลยีสุรนารี
ปีการศึกษา 2550

DEVELOPMENT OF EXPERIMENTAL STATION AT THE SIAM PHOTON LABORATORY FOR ULTRA-THIN MAGNETIC FILMS RESEARCH

Suranaree University of Technology has approved this thesis submitted in partial fulfillment of the requirements for the Degree of Doctor of Philosophy.

Thesis Examining Committee

(Assoc. Prof. Dr. Prapun Manyum)
Chairperson

(Asst. Prof. Dr. Prayoon Songsiriritthigul)
Member (Thesis Advisor)

(Dr. Hideki Nakajima)
Member

(Prof. Dr. Sukit Limpijumnong)
Member

(Dr. Saroj Rujirawat)
Member

(Assoc. Prof. Dr. Saowanee Rattanaphani)
Vice Rector for Academic Affairs

(Assoc. Prof. Dr. Sompong Thammathaworn)
Dean of Institute of Science

มรกต พุทธกาล : การพัฒนาสถานีทดลองด้านโฟโตอิมิสชัน ณ ห้องปฏิบัติการแสงสยาม สำหรับงานวิจัยแผ่นฟิล์มแม่เหล็กบาง (DEVELOPMENT OF THE PHOTOEMISSION EXPERIMENTAL STATION AT THE SIAM PHOTON LABORATORY FOR ULTRA-THIN MAGNETIC FILMS RESEARCH)
อาจารย์ที่ปรึกษา : ผู้ช่วยศาสตราจารย์ ดร.ประยูร ส่งสิริฤทธิกุล, 134 หน้า.

ระบบลำเลียงแสง 4 ของห้องปฏิบัติการแสงสยามได้ถูกปรับแต่งให้สามารถใช้งานได้โดยมีคุณลักษณะเป็นไปตามที่ได้ออกแบบไว้ คือค่าความสามารถในการแยกแยะความยาวคลื่นแสงที่ได้มีค่าสูงถึง 5000 พร้อมกับได้มีการลดสัดส่วนของแสงในอันดับที่สูงโดยถูกทำให้มีสัดส่วนน้อยลง และได้มีการปรับปรุงสถานีทดลองด้านโฟโตอิมิสชันของระบบลำเลียงแสง 4 เพื่อสนองความต้องการของผู้ใช้ที่เพิ่มขึ้น โดยมีการพัฒนานำระบบต่อเชื่อมห้องสุญญากาศหลายห้องเข้ามาใช้ เพื่อที่จะทำให้การใช้แสงซินโครตรอนในเทคนิคโฟโตอิมิสชันมีประสิทธิภาพมากขึ้น และทำให้สามารถใช้เทคนิคต่างๆ ที่ไม่ต้องนำออกจากสุญญากาศในลักษณะที่ขนานกัน และที่สำคัญคือเทคนิคการวัดต่างๆ สามารถใช้งานในลักษณะที่ไม่ต้องนำสารตัวอย่างออกจากระบบสุญญากาศ นอกเหนือจากเทคนิคโฟโตอิมิสชันแบบแยกแยะและแบบไม่แยกแยะเชิงมุมแล้ว เทคนิคมาตรฐานที่สามารถใช้ได้คือ สเปกโทรสโกปีของโฟโตอิเล็กตรอนที่เกิดจากแสงอัลตราไวโอเลตและรังสีเอกซ์ สเปกโทรสโกปีของออเจอร์อิเล็กตรอน และการเลี้ยวเบนของอิเล็กตรอนพลังงานต่ำ ระบบการเตรียมแผ่นฟิล์มบางของโลหะ โดยเทคนิคการปลูกผลึกหรือการทับถมด้วยลำโมเลกุล ได้ถูกพัฒนาขึ้นและได้ต่อเชื่อมเข้าเป็นส่วนหนึ่งของสถานีทดลองใหม่ที่ถูกพัฒนาขึ้นนี้ ได้ทำการแสดงให้เห็นว่าสถานีทดลองใหม่นี้สามารถใช้งานได้ตั้งแต่การเตรียมผิวหน้าสาร การสร้างแผ่นฟิล์มบางของโลหะสารแม่เหล็ก โดยเทคนิคการปลูกผลึกหรือการทับถมด้วยลำโมเลกุล ตลอดจนการวิเคราะห์แผ่นฟิล์มบางโดยไม่มีการนำสารตัวอย่างออกจากสุญญากาศได้อย่างสำเร็จ ระบบดังกล่าวเปิดโอกาสสำหรับงานวิจัยด้านแผ่นฟิล์มบางสารแม่เหล็ก

สาขาวิชาฟิสิกส์ ลายมือชื่อนักศึกษา
ปีการศึกษา 2550 ลายมือชื่ออาจารย์ที่ปรึกษา

MORAGOTE BUDDHAKALA : DEVELOPMENT OF THE
PHOTOEMISSION EXPERIMENTAL STATION AT THE SIAM
PHOTON LABORATORY FOR ULTRA-THIN MAGNETIC FILMS
RESEARCH. THESIS ADVISOR : ASST. PROF. PRAYOON
SONGSIRIRITTHIGUL, Ph.D. 134 PP.

ULTRA-THIN FILMS/PHOTOEMISSION/BEAMLINE/MONOCHROMATOR

The BL4 beamline at the Siam Photon Laboratory has been optimized to meet the designed resolving power of 5000. Suppression of high-order lights has also been demonstrated. The experimental station of the BL4 beamline has been upgraded to serve the increasing demands of users. The demand for more efficient use of allocated synchrotron light beamtime can now be satisfied with the use of a multi-UHV-chamber system to allow photoemission measurements using synchrotron light to be performed in parallel with the preparation and/or with *in situ* surface analysis of other samples. More importantly, the techniques are *in situ* techniques. Standard surface-sensitive techniques available, in addition to AIPES and ARPES using synchrotron light, are UPS, XPS, AES and LEED. Finally, a metal molecular beam epitaxy/deposition system has been developed and connected to the multi-UHV-chamber system. The growth/deposition of magnetic ultra-thin films on Si(100) and Cu(110) substrates and *in-situ* characterizations of the substrates and films have successfully been demonstrated. The system provides research opportunity in the area of ultra-thin magnetic films.

School of Physics Student's Signature______________________

Academic Year 2007 Advisor's Signature______________________

ACKNOWLEDGEMENTS

This thesis work could not have been completed without the generous support and advice of many persons. I would like to thank:

- My thesis advisor Asst. Prof. Dr. Prayoon Songsiriritthigul who has provided me the golden opportunity to experience R&D atmosphere at the Siam Photon Laboratory. Without his advice and never-ending support, this work would have not been possible.
- Manager of the BL4 beamline Dr. Hideki Nakajima at the Siam Photon Laboratory, who has given me useful guidance and technical assistance related to the instruments at the BL4 beamline.
- Assoc. Prof. Dr. Sompong Thammathaworn, the dean of Institue of Science, Suranaree University of Technology, for his support in various respects.
- Assoc. Prof. Dr. Prapun Manyum, the head of School of Physics, Suranaree University of Technology, for his kind support.
- NSRC staff, especially engineers in the beamline division, and my family for their help and encouragements.
- Rajamangala University of Technology Thanyaburi (RMUTT) and National Synchrotron Research Center (NSRC), for financial support.

Moragote Buddhakala

CONTENTS

Page

CONTENTS (Continued)

Page

CONTENTS (Continued)

Page

LIST OF TABLES

LIST OF FIGURES

Figure **Page**

LIST OF FIGURES (Continued)

LIST OF FIGURES (Continued)

Figure **Page**

LIST OF FIGURES (Continued)

Figure **Page**

LIST OF FIGURES (Continued)

LIST OF FIGURES (Continued)

CHAPTER I

INTRODUCTION

1.1 Introductory Remarks

Magnetism of matter is an interesting and complicated phenomenon because of the direct connection between magnetism and the electronic structure of matter. It took almost three centuries to study and describe quantitatively magnetism of matter. The main obstacles which had and some still have to be over come are the followings. First, the total magnetic moment of a piece of solid matter is made up of the orbital and spin contributions of individual electrons. A theoretical treatment of the electron spin requires the framework of relativistic quantum mechanics and can only be given within Dirac's theory. Second, magnetism in a solid is a purely quantum mechanical phenomenon, there is no way to explain within classical physics. The spin-dependent Coulomb type interaction, so-called exchange interaction, drives the formation of a long-range magnetically ordered ground state in the solid matter. Such interaction is a consequence of the collective behavior of a Fermion system. At present, theoretical procedures based on mean-field approaches yield a reasonable good description of the ferromagnetism at ground states. However, they usually fail to reliably predict the excited states, which are probed in many experiments. Third, it is still difficult to predict magnetic anisotropies in crystalline materials from the first principles calculations though it has been known for a long time that a spin dependent interaction, the spin-orbit coupling, is one of the forces causing the anisotropies. Finally, from the observations, electrons in different energy levels may be responsible for magnetism of different materials. Rare earth magnets, for example, are understood that localized *f*-electrons contribute to magnetism. Thus these magnets are often described in atomic-like picture. For 3*d*-transition magnetic materials, the electron contributed to the magnetism are itinerant. The sharp distinction into localized and itinerant magnets represents only the two extreme aspects. In reality, any electronic system will reveal a mixture of localized and itinerant contributions. Thus a unified picture of magnetism is still highly required (Horn and Scheffler, 2000).

In addition to the fundamental interest, magnetic materials have been used in many different magnetic applications. Among various magnetic material systems, low-dimensional magnetic systems or thin films of magnetic materials have extensively been used and can be found in devices used in our daily life, for examples, the magnetic and magneto-optical recording media such as audiotape, videotape, memory disk, reading header of a hard drive. At present, research and development in the field of the low-dimensional magnetic systems is still driven by the demands of information technology. One of the primary demands is the increase of the areal information density on the storage media.

Thank to the advance of ultra-high vacuum (UHV) technology, very thin films of different materials may be grown on different substrates. The growth rate can be controlled to be in the sub-Angstrom/second range. The thickness of the films can also be controlled to be comparable to the size of atoms, and thus the degree of freedom of electrons in the films is reduced to 2-dimension. Combining this with patterning techniques, 1-dimensional magnetic systems can be obtained. In the low-dimensional magnetic systems, the electrons may behave differently from electrons in bulk of the same magnetic material resulting in different and, sometimes, surprising magnetic properties.

Several vacuum-based techniques have been adopted for synthesizing ultra-thin films of magnetic materials. Among those techniques, the molecular beam epitaxy (MBE) technique provides ultimate control over the growth process, allowing epitaxial growth of various material systems that do not exist in the nature. In some applications, where epitaxial growth is not necessary, molecular beam deposition (MBD) may be adopted to deposit very thin films.

The main goal of this thesis work is to extend research opportunities at the BL4 beamline (Songsiriritthigul, 2001) of the Siam Photon Laboratory not only for ultra thin magnetic films research but also for surface and interface research in general. A metal MBE/MBD system together with UHV-multi-chamber system consisting of an X-ray photoelectron spectroscopy (XPS) system, UHV sample transporters and load-lock systems have successfully been developed. Along the course of this thesis work, the performance of the BL4 beamline has successfully been pushed to its designed specifications. The resolving power of the monochromator of the BL4 beamline has been optimized to obtain the maximum designed resolving power.

1.2 Optical Path

Conventional refracting optical elements cannot be used in the VUV (vacuum ultraviolet) region because the absorption coefficient for all materials is very high in this region. Thus, reflecting optical elements such as mirrors and reflecting gratings are normally used in grazing incident geometry. When the grazing angles are used in conjunction with mirrors of various shapes of optical surface, the optical aberrations or deviations from a perfect image are inevitable. The aberrations are the results from the differences in the possible optical paths from one point to another via some geometrical surfaces. The aberrations result in the distorted image with appearance different from the object, or the source. The resolving powers of grating monochromators critically depend also on quality of the image on the exit slit and hence on controlling the aberrations or deviation from a perfect image. Thus, synchrotron light beamlines with high performance must be designed to minimize the optical aberrations as much as possible.

In 1657, the least time principle was proposed by P. de Fermat to explain the phenomena of refraction and reflection. The Fermat's principle postulates that the optical path from point *A* to point *B* must be an extremum. Figure 1.1 illustrates the application of Fermat's principle to the light path function. In the figure, the optical path function *F* for rays of light from the point *A* impinge on an optical surface *P(*ξ,ω,l) and form an image at point *B* is written as

$$F = \overline{AP} + \overline{PB} + G \tag{1.1}$$

where *G* is the groove function introduced when an optical element is a diffraction grating. The distance of $\overline{AP}$ and $\overline{PB}$ are given in polar coordinate by

$$\overline{AP} = \sqrt{r_1^2 + \omega^2 + l^2 - 2\omega r_1 \sin\alpha} \tag{1.2}$$

$$\overline{PB} = \sqrt{r_2^2 + \omega^2 + l^2 - 2\omega r_2 \sin\beta} \tag{1.3}$$

From the optical path function, focusing and imaging properties can be calculated. The conditions for all paths via the mirror surface *P(*ξ,ω,l) which lead to a focus are the followings:

$$\frac{\partial F}{\partial \omega} = 0 \qquad \text{(meridional focus),} \tag{1.4}$$

$$\frac{\partial F}{\partial \ell} = 0 \qquad \text{(sagittal focus).} \tag{1.5}$$

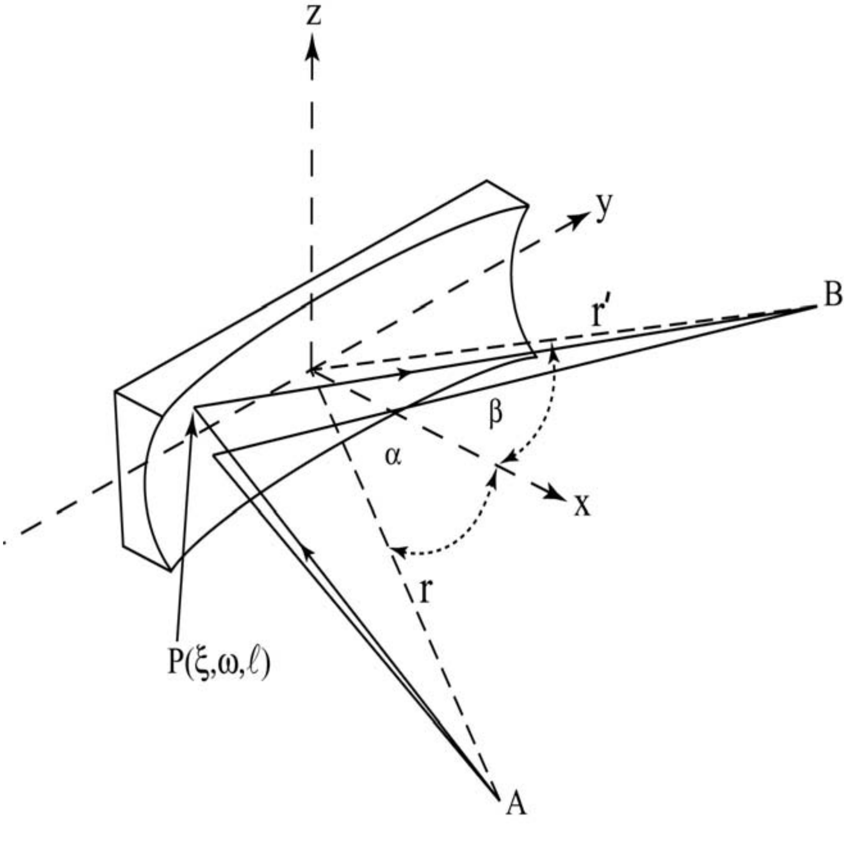

Figure 1.1 Rays of light from the source *A* formed an image at B via a surface *P(*ξ,ω,l) (Peatman, 1997).

The optical surface of an optical element can be expressed in the general form of a polynomial function as

$$\xi = \sum_{i=0}^{\infty} \sum_{j=0}^{\infty} a_{ij} \omega^i l^j \tag{1.6}$$

When the *x*-*y* plane is chosen as a symmetry plane, the coefficients $a_{00} = a_{10} = 0$; j = even. The a_{ij} coefficients for toroidal and spherical surfaces, the most-frequent-used surfaces, are given in Table 1.1. It should be noted that a spherical shape is considered as a special case of a toroidal surface, i.e. the case that $\rho = R$.

Table 1.1 The coefficients of a_{ij} for toroid and spherical surfaces.

a_{ij}	Toroid	Spherical
a_{02}	$\frac{1}{2\rho}$	$\frac{1}{2R}$
a_{04}	$\frac{1}{8\rho^3}$	$\frac{1}{8R^3}$
a_{12}	0	0
a_{20}	$\frac{1}{2R}$	$\frac{1}{2R}$
a_{22}	$\frac{1}{4R^2\rho}$	$\frac{1}{4R^3}$
a_{30}	0	0
a_{40}	$\frac{1}{8R^3}$	$\frac{1}{8R^3}$

The optical path given in equation (1.1) can be expressed into a power series of ω and l after substituting equations (1.2), (1.3) and (1.6) into equation (1.1).

$$F = F_{000} + \omega F_{100} + \frac{1}{2}\omega^2 F_{200} + \frac{1}{2}l^2 F_{020} + \frac{1}{2}\omega^3 F_{300} + \frac{1}{2}\omega l^2 F_{120} + \frac{1}{8}\omega^4 F_{400} + \frac{1}{4}\omega^2 l^2 F_{220}$$

$$+ \frac{1}{8}l^4 F_{040} + lF_{011} + \omega l F_{111} + \frac{1}{2}\omega F_{102} + \frac{1}{4}\omega^2 F_{202} + \frac{1}{2}\omega^2 l F_{211} + \ldots \tag{1.7}$$

where the F_{ijk} terms were first given by Noda, Namioka, and Seya in 1974, only the major F_{ijk} terms are shown below.

$$F_{000} = r + r' \tag{1.8}$$

$$F_{100} = Nk\lambda - (\sin\alpha + \sin\beta) \tag{1.9}$$

$$F_{200} = \left(\frac{\cos^2\alpha}{r}\right) + \left(\frac{\cos^2\beta}{r'}\right) - 2a_{20}(\cos\alpha + \cos\beta) \tag{1.10}$$

$$F_{020} = \frac{1}{r} + \frac{1}{r'} - 2a_{20}(\cos\alpha + \cos\beta) \tag{1.11}$$

$$F_{300} = \left[\frac{T(r,\alpha)}{r}\right]\sin\alpha + \left[\frac{T(r',\beta)}{r'}\right]\sin\beta - 2a_{30}(\cos\alpha + \cos\beta) \tag{1.12}$$

$$F_{120} = \left[\frac{S(r,\alpha)}{r}\right]\sin\alpha + \left[\frac{S(r',\beta)}{r'}\right]\sin\beta - 2a_{12}(\cos\alpha + \cos\beta) \tag{1.13}$$

$$\begin{aligned} F_{400} = {} & \frac{4T(r,\alpha)}{r^2}\sin^2\alpha - \frac{T^2(r,\alpha)}{r} + \frac{4T(r',\beta)}{r'^2}\sin^2\beta - \frac{T^2(r',\beta)}{r'} \\ & -8a_{30}\left[\frac{1}{r}(\sin\alpha\cos\alpha) + \frac{1}{r'}(\sin\beta\cos\beta)\right] - 8a_{40}(\cos\alpha + \cos\beta) + 4a_{20}^2\left[\frac{1}{r} + \frac{1}{r'}\right] \end{aligned} \tag{1.14}$$

…

where $T(r,\alpha) = (\cos 2\alpha / r) - 2a_{20}\cos\alpha$ and $S(r,\alpha) = (1/r) - 2a_{02}\cos\alpha$ $T(r',\beta) = (\cos 2\beta / r') - 2a_{20}\cos\beta$ and $S(r',\beta) = (1/r') - 2a_{02}\cos\beta$. N and k are the groove density of a classical grating and the order of diffraction, respectively.

1.3 Grating Monochromator

The grating equation is given by the F_{100} term of the optical path function. The sign convention for the diffraction angle β is shown in Figure 1.2. When angle α and β are on opposite side of the normal angle, they have opposite sign. The order of diffraction k is positive order, inside order, when the angle β is smaller than that of the zero-order beam.

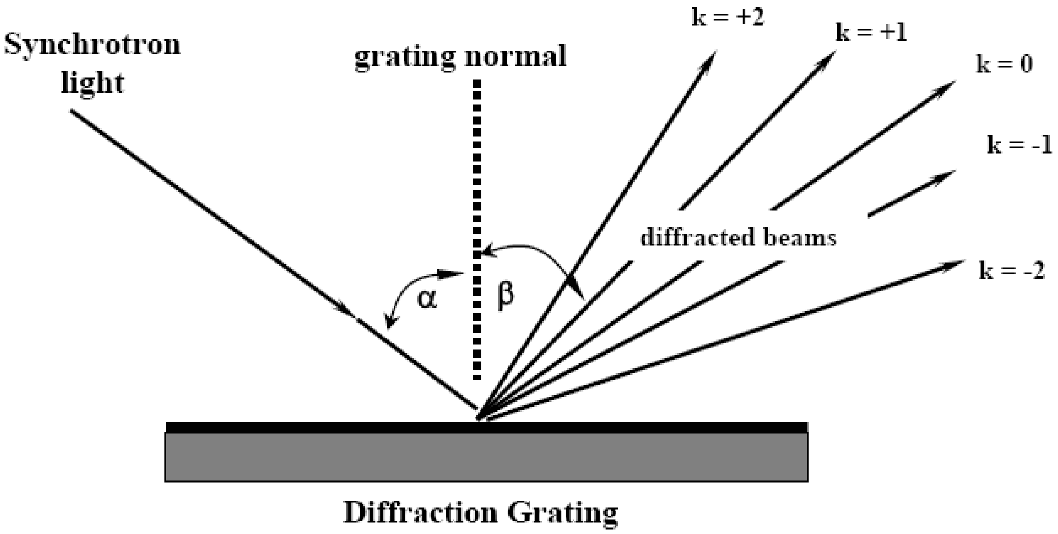

Figure 1.2 A diffraction grating showing the sign convention and diffraction orders.

Ideally, all F_{ijk} terms should be suppressed to make an optical system free of aberrations. In practice, it is not possible to make all F_{ijk} terms vanished over the whole operational spectral range, particular in the VUV region as the grazing incidence geometry is employed. Thus, the F_{ijk} terms are kept to be zero at some certain wavelengths to minimize the aberrations for the whole operational spectral range. In practice, only the first few major terms are considered in most optics design.

Except the F_{000}, all other F_{ijk} terms given above do not valid for aberration-corrected gratings such as the ones used in the monochromator of the BL4 beamline, which is a varied line-spacing plane grating (VLSPG), or a varied groove density plane grating. A small modification is need for VLSPG. The groove density of VLSPG is a function of the distance on the grating and along the axis in the dispersive plane, ω, as:.

$$N(\omega) = N_0(1 + a_1\omega + a_2\omega^2 + a_3\omega^3 + ...) \tag{1.15}$$

where N_0 is the groove density at the center of the grating and a_{i} (i = 1, 2, 3, …) are the space variation parameters. Substituting the groove density of VLSPG in eq.(1.1), one obtains the optical path as:

$$F = \overline{AP} + \overline{PB} + k\lambda\int_0^{\omega} N(\omega)d\omega \tag{1.16}$$

Substitution of the function of groove density, eq.(1.15), into eq.(1.16), the optical path can be expressed as eq.(1.7) with the most important F_{ijk} terms given by:

$$F_{000} = r + r' \tag{1.17}$$

$$F_{100} = Nk\lambda - (\sin\alpha + \sin\beta) \tag{1.18}$$

$$F_{200} = \frac{\cos^2\alpha}{r} + \frac{\cos^2\beta}{r'} + k\lambda N_0 a_1 \tag{1.19}$$

$$F_{300} = \frac{\sin\alpha\cos^2\alpha}{r^2} + \frac{\sin\beta\cos^2\beta}{r'^2} + \frac{2}{3}k\lambda N_0 a_2 \tag{1.20}$$

$$F_{120} = \frac{\sin\alpha}{r^2} + \frac{\sin\beta}{r'^2} \tag{1.21}$$

$$F_{400} = \frac{\cos^2\alpha}{r^3}(4\sin^2\alpha - \cos^2\alpha) + \frac{\cos^2\beta}{r'^3}(4\sin^2\beta - \cos^2\beta - \cos^2\beta) + 2k\lambda N_0 a_3 \tag{1.22}$$

It should be noted that for a plane optical surface, the radius of curvatures is infinite and the terms containing 1/R or 1/ρ vanish. The theoretical resolution, $\Delta\lambda / \lambda$ or $\Delta E / E$, may be obtained by taking a derivative the optical function with respect to the distance along the axis in the dispersive plane, i.e. ω. The resolution as a function of the F_{ijk} terms is given below:

$$\frac{\Delta\lambda}{\lambda} = \frac{1}{Nk\lambda}\left[\omega F_{200} + lF_{020} + \frac{3}{2}\omega^2 F_{300} + \frac{1}{2}l^2 F_{120} + \frac{1}{2}\omega^3 F_{400} + ...\right] \tag{1.23}$$

The major terms F_{200}, F_{300}, F_{120} and F_{400} are called defocus, coma, astigmatic and spherical aberrations, respectively. The relation between different types of the optical aberrations and the resolution, $\Delta\lambda/\lambda$, can explicitly be written as follow:

$$\left.\frac{\Delta\lambda}{\lambda}\right|_{Defocus} = \frac{\omega}{Nk\lambda} F_{200} \tag{1.24}$$

$$\left.\frac{\Delta\lambda}{\lambda}\right|_{Coma} = \frac{3}{2}\frac{\omega^2}{Nk\lambda} F_{300} \tag{1.25}$$

$$\left.\frac{\Delta\lambda}{\lambda}\right|_{Astigmatic} = \frac{1}{2}\frac{l^2}{Nk\lambda} F_{120} \tag{1.26}$$

$$\left.\frac{\Delta\lambda}{\lambda}\right|_{Spherical} = \frac{1}{2}\frac{\omega^3}{Nk\lambda} F_{400} \tag{1.27}$$

As already mentioned, the total resolution cannot be zero for the whole operational spectral range of the monochromator. However, it is possible to minimize the total resolution by making different optical aberrations vanished at certain photon energy. For a VLSPG monochromator, major aberrations are corrected by choosing proper spacing-variation parameters of VLSPG. The biggest aberration term is the meridional defocus term, i.e. the F_{200} term. By choosng proper two photon energies to make the defocusing term vanished, i.e.

$$F_{200}(E_1) = F_{200}(E_2) = 0\ . \tag{1.28}$$

The spacing variation parameter a_1 and the exit arm length of VLSPG, r_2, can be obtained through the following relationships:

$$a_1 = \frac{-1}{k\lambda_1 N_0}\left(\frac{\cos^2\alpha_1}{r_1} + \frac{\cos^2\beta_1}{r_2}\right) \tag{1.29}$$

$$r_2 = \frac{\lambda_2\cos^2\beta_1 - \lambda_1\cos^2\beta_2}{\lambda_1\cos^2\alpha_2 - \lambda_2\cos^2\alpha_1}\ r_1 \tag{1.30}$$

Similarly, the spacing variation parameters a_2 and a_3 are obtained by making the coma and spherical aberration terms vanished at photon energies E_3 and E_4, respectively. Thereafter, one obtains

$$a_2 = \frac{-3}{2k\lambda N_0}\left(\frac{\sin\alpha\cos^2\alpha}{r_1^2} + \frac{\sin\beta\cos^2\beta}{r_2^2}\right) \tag{1.31}$$

$$a_3 = \frac{-1}{2k\lambda N_0}\left(\frac{\cos^2\alpha}{r_1^3}(4\sin^2\alpha - \cos^2\alpha) + \frac{\cos^2\beta}{r_2^3}(4\sin^2\beta - \cos^2\beta\right) \tag{1.32}$$

The figure slope error of the grating and the slit width, in addition to the optical aberrations mentioned above, are also important contributions limiting the resolution of the monochromator. The figure slope error of the grating contributes to the resolution through the following formular,

$$\Delta\lambda/\lambda\big|_{slope} = (4.7\sigma_{se}\cos\beta)/\lambda Nk \tag{1.33}$$

where σ_{se} is the *root-mean-square* (*rms*) figure slope error of the grating. It is obvious to understand the relation between the slit width and the resolution that the resolution increases with increasing the slit width. The resolution as the function of the slit width can be derived directly from the grating equation, which are given as

$$\frac{\Delta\lambda}{\lambda} = \frac{1}{Nk\lambda}\left(\frac{\Delta S_1}{r}\cos\alpha\right) \tag{1.34}$$

$$\frac{\Delta\lambda}{\lambda} = \frac{1}{Nk\lambda}\left(\frac{\Delta S_2}{r'}\cos\beta\right) \tag{1.35}$$

where ΔS_1 and ΔS_2 are the width of the entrance and exit slits, respectively.

1.4 Vacuum

Vacuum has its root from Latin word “vacuus”, which means empty. However, there is no space which is perfectly empty. Vacuum is defined as a volume of space that has its gaseous pressure below the standard atmospheric pressure. The gaseous pressure is a quantity that depends primarily on the amount of gases molecules remaining in a volume of space. It should be noted that the pressure is caused by momentum transfer when gas molecules impinge on the vessel wall. Thus, the pressure is dependent also on temperature (i.e. gas velocity) and chemical composition (i.e. mass). From the kinetic theory, the gaseous pressure is given, mathematically, by

$$P = \frac{nRT}{V} \quad , \tag{1.36}$$

where *P* is the pressure exerted on the walls of a vessel containing *n* moles of gas, when this vessel has a volume *V*, is maintained at an absolute temperature *T*, and *R* is the ideal gas constant, which is 8.3145 J/(mol. K). If more than one gas in the system, the total pressure is the summation of the “partial pressure” exerted by each gas as given below

$$P_{Total} = P_1 + P_2 + P_3 + \ldots, \tag{1.37}$$

where P_1, P_2 and P_3 are the partial pressure of gas species 1, 2 and 3, respectively.

Vacuum quality may be divided into ranges according to the technology required to achieve it or measure it. There is no general universally agreed where is the exact boundary adjacent range, however the typical a typical distribution of the ranges is as in Table 1.2 follows:

Table 1.2 The classifications of vacuum quality/level.

Range	Pressure (Torr) (1 Torr = 101 kPa)
Atmospheric pressure	760
Low vacuum	<760 to 25
Medium vacuum	25 to 1×10^{-3}
High vacuum	1×10^{-6} to 1×10^{-9}
Ultra high vacuum	1×10^{-9} to 1×10^{-12}
Extremely high vacuum	$<1\times10^{-12}$
Outer space	1×10^{-6} to $<3\times10^{-17}$
Perfect vacuum	0

Instead of the gaseous pressure, "mean free path" is often used to indicate the amount of gases molecules in the system. The mean free path (*MFP*) is the average distance traversed by molecules between successive intermolecular collisions. The *MFP* increases as the gas density decreases. The *MFP* can be calculated from the formula given below.

$$MFP = \frac{1}{\sqrt{2}\pi n \sigma^2}, \tag{1.41}$$

where σ and n represents the molecular diameters and the number of molecules per cubic centimeter, respectively. For air at room temperature, the mean free path is expressed as a function of pressure as:

$$MFP = \frac{5 \times 10^{-3}}{P}, \tag{1.42}$$

where P is the gaseous pressure in torr, and MFP is in centimeter. The average MFP of air molecules at room temperature at different pressure given in Table 1.3

Table 1.3 The average MFP of air molecules at room temperature at different pressures.

Pressure (torr)	Mean Free Path (cm)
1 atm	6.7×10^{-6}
1 torr	5×10^{-3}
1 millitorr	5
10^{-6} torr	500
10^{-10}	500 km

Many different devices, instruments and even production processes required vacuum. Applications of low vacuum can be seen in devices/equipment used in our daily life, for example incandescent light bulbs, cathode ray tubes, vacuum tube and vacuum cleaners. It is also useful for industrial applications in various processes, for example electron beam welding, chemical vapor deposition, dry etching, optical coating, cold welding, vacuum packing and vacuum flying. Vacuum in the high vacuum and UHV ranges is very useful for thin film deposition. In the UHV region, thin films may be epitaxially grown when the material system is appropriate. The advance of UHV technology is an important factor for surface science and thin films research.

1.5 MBE/MBD

MBE is a method to grow thin crystal films and layered structures. “Epitaxial” is a Greek word, referring to the ordered growth of crysal on another in such a way that the orientation of the grown layer bear a well defined relationship to the substrate (Pashley, 1990). MBE is an epitaxial growth process taking place in a UHV environment. The growth of MBE is essentially slow, typically 1-300 nm/min and thus UHV is essential for MBE as it preserves atomic-scale clean surfaces for a sufficiently long time to avoid minimize impurities. The set-up of MBE systems is thus rather complicated because of the requirement of UHV environment. The base pressure in the growth area must be in the range 10^{-11} mbar. During growth, the pressure is normally kept below 10^{-9} mbar, depending on the growth rate. This stringent vacuum condition provides the mean free path of the atoms or molecules evaporated from the deposit materials to be larger than the distance between the substrate and the source of the deposit materials. The sources are designed and installed in MBE system in such a way that the atoms or molecules generated in the sources will leave the sources as a “beam” and then impinge on the substrate without colliding with the internal wall of the vacuum chamber or instrument/tool in the vacuum. The atomic or molecular beams can be produced by thermal evaporators or by electron-beam evaporators.

The advantage of MBE is its growth process, which is the physical process. This allows the process to be simulated within the framework of physics. The growth can also be *in situ* monitored during growth using RHEED (reflection high-energy electron diffraction). The evaporation rate can be controlling very precisely using feedback signals from gas analyzing tools such as QMS (quadrupole mass spectrometer) or from a quartz crystal film thickness measuring device. With appropriate condition, meta-stable high crystalline quality layers may be obtained.

The most successful material system for MBE is the III-V compound semiconductors. For some material systems, thick expitaxial layers are prohibit by the large lattice mismatch between the overlayer and that of the substrate, and in many cases expitaxial layers are not possible at all to be obtained. Thus, the word "deposition" is used instead of "expitaxy".

Ultra-thin magnetic films grown by MBE technique often exhibit interesting properties. For example, the Curie temperature of the Ni film varies with the thickness of the film (Huang, Kief, Mankey, and Willis,1994). It should be note that Ni has the lowest Curie temperature comparing to other 3*d* magnet. There has been an interesting report that Ni films grown on W(110) substrates showed strange behavior. The Ni films with thickness less than 5 ML (monolayer) show the 2D Ising magnetism. The β-value of magnetization density, $M \propto (1 - T/T_c)^{\beta}$, is about 0.13. For the Ni films with thickness greater than 5 ML, the Ni films exhibit the 3D Heisenberg magnetism (β ~ 0.37) (Li and Baberschke, 1992). However, when Cu(001) and Cu(111) were used as the substrates, the β-value was found to be 0.23

and 0.37 for the thickness of the NI film less and greater than 7ML, respectively (Huang, Kief, Mankey, and Willis, 1994; Moruzzi and Williams, 1978). The available experimental results were obtained by measuring macroscopic properties such as magnetization measurements. Thus, there are still demands for the explanation in a microscopic level to find the relation between the observed magnetic properties and the atomic and electronic structure of the ultra-thin magnetic films.

There have also been theoretical calculations suggesting that Cu atoms of the substrate could diffuse into the Ni film if the substrate temperature was high enough (Raeker and De Pristo, 1992). Experimental results from photoelectron diffraction measurement have confirmed the prediction (Kim, Hohamed, and Kesmodel, 1992) and have suggested that the diffusion occurred during the growth process (Hernnas, Karolewski, Tillborge, and Martensson, 1994). More detailed studies of Ni deposited on a Cu substrate using LEED showed that the surface of Ni films consist of Cu atoms when the thickness of the Ni films was less than 3 ML. Beneath the surface Cu layer, Ni atoms are disordered arranged.

Thin films of Ni deposited on Cu(001) has different behavior from that of Fe and Co films in a way that the direction of the magnetization of the Ni films changes with the thickness of the films, i.e. the direction of magnetization may be in-plane, perpendicular to the films or the combination of the two directions (Schulz and Baberschke, 1994; Schulz, Schwarzwald, and Baberschke, 1994). For Ni films with thickness between ~8 ML to ~55 ML, the easy magnetization axis is perpendicular to film surface, providing the possibility to employ the films with these thicknesses for high capacity data storage media (Pinski, Staunton, Gyortfy, and Stock, 1986). More importantly, it has been a study showing that these Ni films were very stable; the magnetic properties did not change after they have been used for over 10^6 cycles of data writing-reading.

Among 3*d* ferromagnets (Fe, Co, and Ni), Fe is the most interesting elements because of its diversity of the magnetic properties because it ia heavily used in amny different applications. It is interesting that thermally stable fcc Fe could be obtained by the formation of ultra-thin films of Fe on a Cu(001) single-crystal substrate. The bulk Fe has the body-centered cubic (bcc) structure. The crystal structure of the Fe films on Cu(001) were found to be fcc structure when the thickness of the films was between 5 ML and 11 ML (Jonker, Walker, Kisker, Prinz, and Carbone, 1986; Macedo and Keune, 1988; Li, Freitag, Pearson, Qiu, and Bader, 1994; Vollmer and Kirschner, 2000; Qian and Jin, 2001; Biedermann, Schmid, and Varga, 2001). For thinner Fe films, the crystal structure of the films was face-centered tetragonal (fct) (Pappas, D. P., et al., 1991). Thus the Fe films experiences phase transition as the film thickness increases. When the thickness is above 11 ML, the crystal structure and thus the magnetic properties are the same as those of bulk Fe.

Not only Cu single crystals have been chosen to be the substrate for Fe films, but also other materials such as Au(001) (Durr, Taborelli, and Landolt, 1989), Ag(001) (Pinski, Staunton, Gyortfy, and Stock, 1986; Stampanoni, Vaterlaus, Aeschlimann, and Meier, 1987), Co(001) (Escorcia-Aparicio, Kawakami, and Qui, 1996; Klasger, Schmitz, Carbone, Eberhardt, and Kachel, 1998) and Rh(001) (Hayashi, Sawada, and Kakizaki, 2001) have been used for the investigation of the structural and magnetic properties of ultra-thin Fe films. One of the differences for various substrate materials is the lattice constant (a_o), which is the primary factor to determine the crystalline structure or the quality of the grown Fe layers. Fe films with the thickness less than 5ML grown on Au(001) and Ag(001) substrates were reported to be a ferromagnet with bcc structure. When Co(001) or Rh(001) was used as the substrate, the fct structure was obtained.

Theoretical study of ultra-thin Fe films showed that there were the effects of temperature on the instabilities of the structure (Kadau and Entel, 1999). Experimental results have confirmed the prediction. For example, fcc-Fe/Cu(001) exhibited no long-range magnetic order at room temperature, but it showed totally different magnetic properties when it was cooled to 70 K (Contnenza, Massidda, and Freeman, 1990; Kittel, 1996). It was also found that the history of the sample temperature profoundly effected on magnetism of ultra-thin Fe films on Cu(001) (Li, Freitag, Pearson, Qiu, and Bader, 1994).

CHAPTER II

INSTRUMENTATIONS AND METHODS

This chapter provides the information related to instrumentations and methods employed in this thesis work. This work covers quite a large area of instrumentations. Photoionization technique is also described as it has been used as a technique to measure the resolving power of the monochromator of the BL4 beamline. To fulfill the objectives of this thesis work, a metal MBE/MBD system, in addition to a multi-UHV-chamber system, has been designed and built for synthesizing magnetic ultra thin films. Thus, the original associated experimental station of the BL4 beamline is provided in this chapter. More importantly, the basics knowledge of vacuum technique and technology is also provided as it is essential for the development of the instrumentations.

2.1 BL4 Optical Beamline

The BL4 beamline is the first synchrotron light beamline at the Siam Photon Laboratory of the National Synchrotron Research Center. The beamline was designed for VUV photoelectron spectroscopy for the investigation of electronic structure of solids and solid surfaces/interfaces.

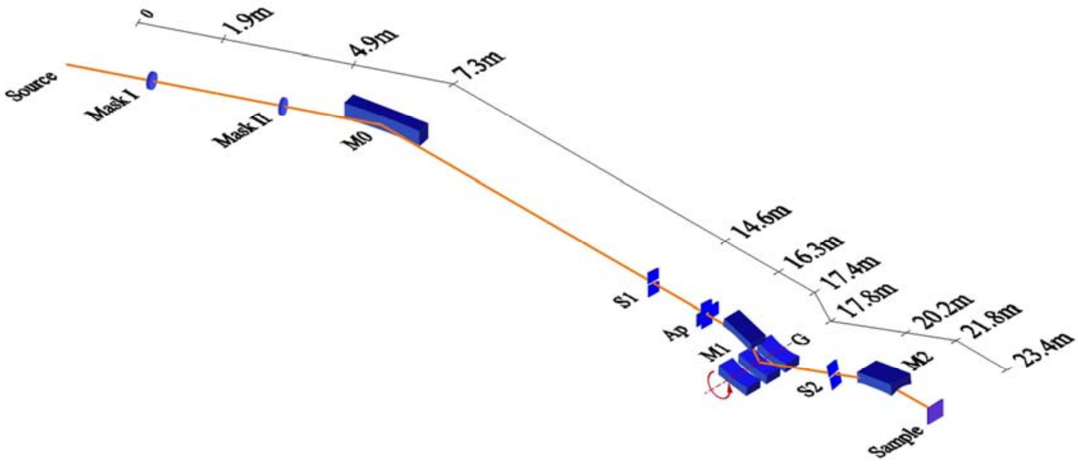

Figure 2.1 The Optical layout of the BL4 beamline at SPL (Songsiriritthigul, 2004; Nakajima, 2007).

The optical layout of the BL4 beamline is illustrated in Figure 2.1. The specifications of the optical beamline are summarized in Table 2.1. The optical beamline consists three main parts, i.e. pre-focusing system, monochromator and post-focusing system.

Table 2.1 Specifications of the BL4 beamline at SPL.

Source	Bending magnet
Energy range	20–240 eV
Expected resolving power	5000 (maximum)
Flux at Sample	$\sim 1 \times 10^{9} - 4 \times 10^{10}$ photons/s
Beam size at Sample (FWHM)	100 (ver.) × 400 (hor.) μm^2

2.1.1 Pre-Focusing Mirror System

The pre-focusing system employs a water-cooled pre-focusing toroid gold-coated mirror, as shown in Fig. 2.1 as *M0*. The advantage of using a toroid mirror is that it has simultaneous focusing power in both horizontal and vertical planes, and thus the number of optical elements is minimized to maximum the throughput of the optical beamline. The toroid mirror deflects the light beam 10° horizontally and focuses the beam onto the entrance slit of the monochromator. M0 is located at 7.3 mm from the source. The designed meridional focal point of M0 is at the position of the entrance slit, S1, which is located at 7.3 mm downstream from M0. It should be noted that the meridional focus is in the dispersive plane of the monochromator, and the deviation of the focal length in this plane will have the influence on the resolving power of the monochromator of the beamline. In addition, the deminification of this mirror in the dispersive plane is kept at 1.0 to minimize coma. The designed value for the big radius of the mirror is 94122 mm. The mirror manufactured by Zeiss has the big radius of curvature of 94300 mm. This 0.189% deviation of the curvature results in a change of the meridional focal position of -0.43%. In order to cope with the deviation of the radius of curvature, the entrance slit is designed to be able to move along the optical axis with in ±100 mm tolerance.

The sagittal focus has no effects on the resolving of the monochromator because it is perpendicular to the dispersive plane of the monochromator. The designed value for the small radius of curvature of the mirror is 636.2 mm. The mirror used at the BL4 beamline has the radius of 637.0 mm., which bigger than the design value of 0.126%. This results in a change of the sagittal focal position of about 0.25%, which is not significant.

2.1.2 Monochromator

The BL4 beamline employ a constant-included angle varied line-spacing plane grating (VLSPG) monochromator. The monochromator consists of an entrance slit, a focusing mirror M1, three VLSP and an exit slit. The monochromator is operated in a constant-included angle of 165°. The monochromator employs the spherical gold-coated mirror as a focusing mirror to converge and vertically deflect the beam onto VLSG. The angle of incidence of M0 is 86°. The proper line-spacing parameters of the grating are chosen to minimize the aberrations as described in Chapter I. Three exchangeable laminar type, holographically ruled and ion etched gratings with the line density at the center of the grating of 300, 600 and 1200 lines/mm are used to cover a photon energy range of 20-240 eV. Photon energy scanning is performed by the rotation of grating. For the whole photon energy range, the monochromatic light is focused virtually at the position of the exit slit, S2. No movement of the exit slit along the optical axis is necessary when photon energy is changed. The total length of the monochromator along the optical axis is 5.6 m.

The designed radius of curvature of M1 is 40140 mm. The entrance slit of the monochromator acts as an object for M1. The distance from the slit to M1 is 2800 mm, thus the image is designed to be at 2400 mm behind the grating. The image again act as a virtual object for the grating. The grating, thus, diffract light on the exit slit. The deviation of the radius of curvature of M1 will definitely have influence on the resolution of the monochromator. M1 made by Zeiss has the radius of curvature of 39880 mm, about 0.648% deviated from the designed radius. Thus, the image position is 0.259 mm behind the grating. In experiments, the position of both the entrance and exit slits must be adjusted to optimize the resolution of the monochromator.

2.1.3 Post-Focusing System

A toroid gold-coated mirror is used to re-focus the monochromatic light on the sample. The mirror is located 1600 mm from the exit slit. It vertically deflects monochromatic light beam to be in the horizontal plane on the sample, which is located 1600 mm downstream the mirror. The designed big and small radii are 26220 mm and 148.8 mm, respectively. The actual mirror has the big and small radii of 26181 mm and 148.7 mm, respectively. The deviation of the radii will have not thing to do with the resolution since the light has already been monochromatized upstream. It only contributes to small distortion of the image on the sample.

2.2 Experimental Station of BL4 Beamline

Figure 2.2 schematically shows the original photoemission system installed in 2002. The primary goal was for the investigations of electronic structures of solids and solid surfaces. The main technique is angle-resolved photoelectron spectroscopy. The system looks complicated as it is the nature of surface science experiments that inevitably require UHV environment that allows the measurement time to be shorter than the time for residual gases to form an overlayer on the sample.

The original experimental station consists of three main chambers, i.e. an analysis chamber, a sample preparation chamber and a load-lock chamber. The analysis chamber is made of mu-metal to shield external magnetic fields preventing the disturbance to electron orbits. Two electron energy analyzers are installed on this chamber. One is a VG Scientific ARUPS10 electron energy analyzer, and the other is a VG Scientific CLAM2 energy analyzer. During the design and installation of this original experimental station, there was no synchrotron light beam in service. Thus different types of laboratory excitation sources were equipped into this chamber such as an electron gun, a twin-anode X-ray tube and a discharged UV lamp. These sources, in a combination with either energy analyzer, allows different type electron spectroscopy could be performed such as Angle-resolved/integrated photoelectron spectroscopy (ARPES/AIPES), X-ray photoelectron spectroscopy (XPS), ultraviolet photoelectron spectroscopy (UPS) and Auger electron spectroscopy (AES).

The load-lock chamber is attached to the side of the analysis chamber (not shown in the figure). The sample is introduced into the system through this chamber without breaking the UHV environment of the analysis chamber. The load-lock chamber is equipped with a long magnetic linear drive that transfers a sample from the load lock chamber to the analysis chamber. A mechanical hand in the analysis chamber is used to move the sample between the sample carousel of the load-lock transfer drive and sample holder of the analysis chamber.

The sample preparation chamber is mounted on top of the analysis chamber. This chamber is vacuum-isoltaed by a UHV gate valve inserted between the preparation chamber and the analysis chamber. The sample manipulator with a 600mm linear translation in the vertical direction is mounted on top of the preparation chamber. The long linear translation of the manipulator allow the sample to be located in the preparation chamber or the analysis chamber.

The surface of the sample sample may be cleaned in the preparation chamber by electron-beam heating or by ion sputtering. The electron-beam heating facility allow the sample to heated up to 1200 K. The energy of ions for ion sputtering can be turned up to 5 keV. After the sample has been treated, the surface impurities can be checked by using AES or XPS measurements in the analysis chamber. The surface crystal structure of the sample can be examined by using LEED in the analysis chamber.

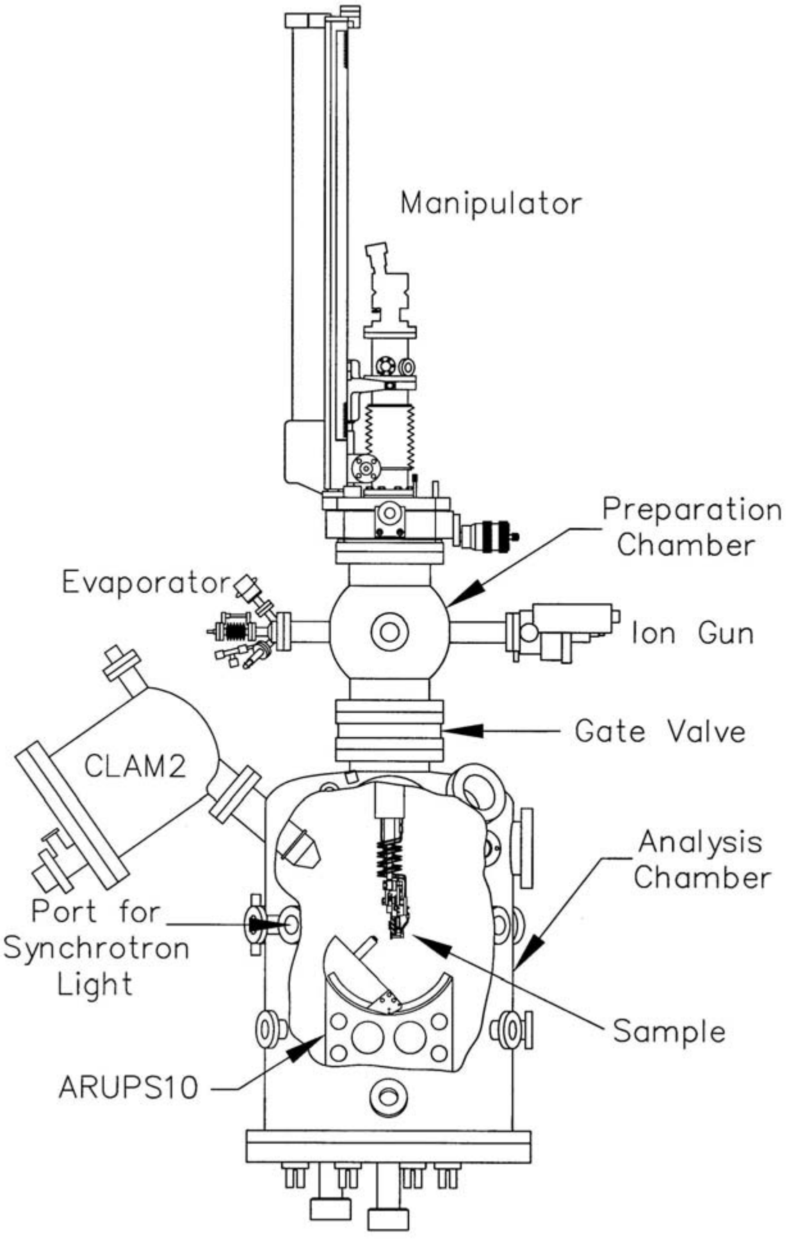

Figure 2.2 Schematic diagram of the original photoemission system at BL4 (Songsiriritthigul, 2001).

2.3 Photoemission

Photoemission Spectroscopy (PES) is a spectroscopic technique for measuring binding energy of electrons excited by photons with sufficient photon energy. The physics of PES is based on the Einstein's photoelectric effect. The matter to be analyzed could be in gas, liquid or solid phase. In gas phase experiment, it is often referred specifically as photoionization. For liquid, however, the measurement cannot be performed as it is limited by the requirement of UHV environment of the experimental set-up and that liquid cannot be brought into vacuum. Thus, PES is generally understood as a technique for solids and gases.

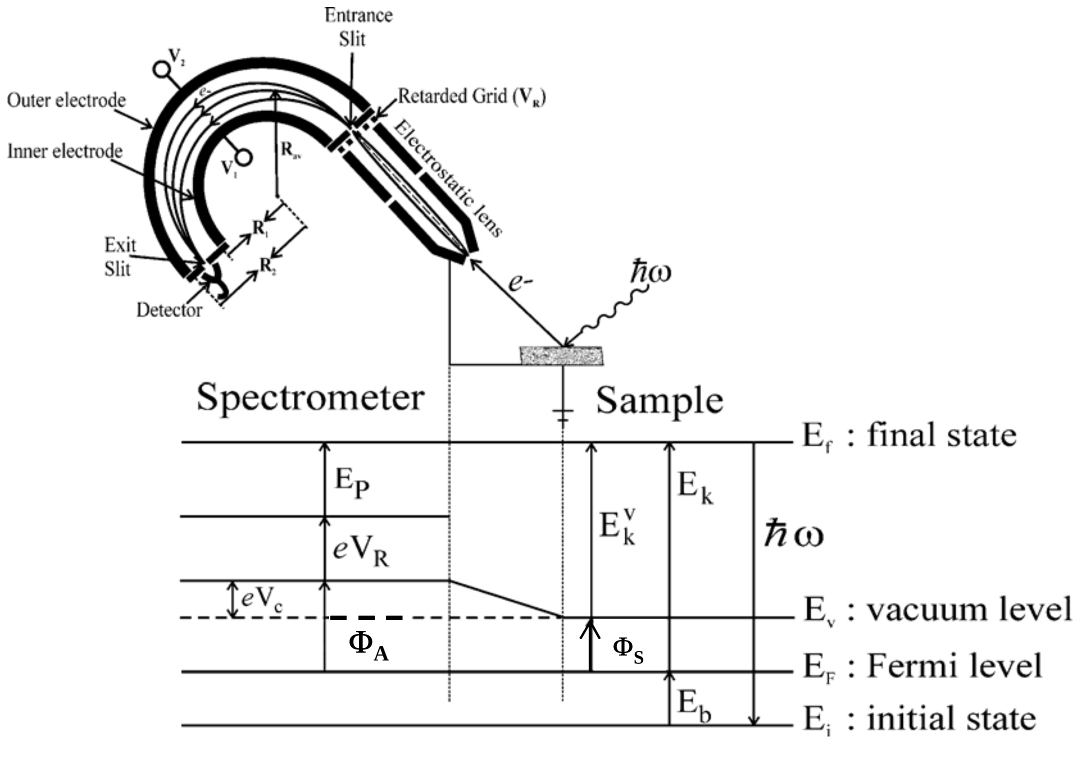

Figure 2.3 experimental set-up for photoemission spectroscopy (Kantee, 2004).

Figure 2.3 show experimental set-up for photoemission spectroscopy. The material to be measured is illuminated with excitation light. Light is absorbed and electrons are emitted from the absorbing atoms when the photon energy is sufficient to overcome the binding energy of the emitted electrons. In order for the electrons to escape from the surface of the material, the electrons must have kinetic energy greater than the work function of the material. The electrons escaping from the surface to vacuum are called photoelectrons. Primarily, PES is a technique to determine the binding energy of photoelectron by measuring the kinetic energy of photoelectron. The binding energy, E_b, and the kinetic energy, E_k, are show in Figure 2.4 and related through the energy conservation law as follow:

$$E_b = h\nu - \Phi - E_k^v \tag{2.1}$$

where hν and Φ are the photon energy of the excitation light and the work function of the analyzed material, respectively.

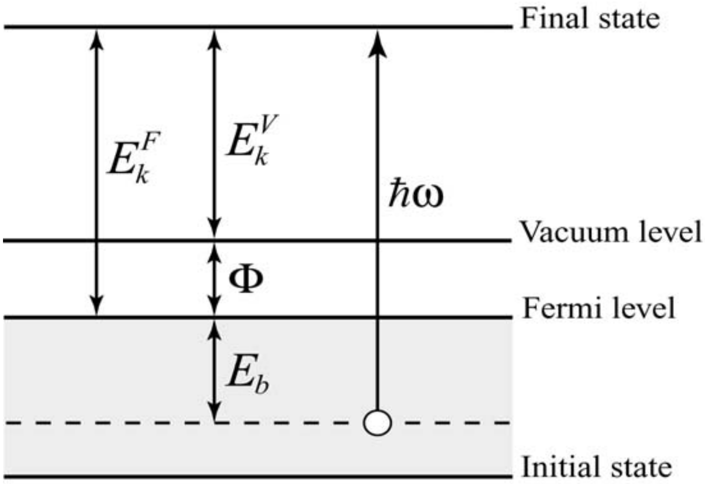

Figure 2.4 Schematic illustration of the energy diagrams of a photoelectron (Kantee, 2004).

In a sudden approximation, the energies of the photoelectrons are assumed to be the characteristic of their original electronic states. Different kinds of the information by PES measurements such as spins, vibrational and rotational information, molecular information, bonding state information, configuration interactions and the polarization effects of the adjacent atoms. However, all these information cannot be obtain in a single measurement set-up. Various experimental configurations have extensively been used to extract the electronic information of solids and solid surfaces.

UPS (ultraviolet photoelectron spectroscopy) and XPS (X-ray photoelectron spectroscopy) or ESCA (electron spectroscopy for chemical analysis) are the most known experimental configurations of photoemission spectroscopy. UPS employs UV (ultraviolet) as the excitation light, and thus the information of the valence band of matter is obtained. The most common excitation source of UPS is a discharged lamp (e.g. He-I: 21.2 eV and He-II: 40.8 eV). UPS is often called valence-electron photoelectron spectroscopy. In UPS measurement on a single crystal, it is called angle-resolved UPS (ARUPS or ARPES) if the measurement has an angular resolving power. For XPS or ESCA, soft X-ray e.g. characteristic X-ray of Mg (1253.60 eV) or of Al (1486.70 eV,1486.27 eV) is used in order to get the information from valence electron, and thus XPS or ESCA is often referred as core-valence photoemission spectroscopy. The distinction between UPS and XPS is rather clear in the former time when only laboratory sources were used. The distinction is no longer clear when a continuous and tunable synchrotron light source is used as the excitation source e.g. some PES beamline provide variable excitation light between 10-1500 eV.

The advances of synchrotron light source and the development of electron energy analyzer have a big impact on the understanding of electronic structure and thus the properties of materials. Synchrotron light has salient and unique properties that PES experiments benefit. The very high photon flux of synchrotron light allows the flux-demanding PES measurements to be performed such as high-resolution PES, spin-resolved PES and trace element PES. The continuous spectrum of synchrotron light allows us to choose proper photon energies suitable for each experiment or to perform PES measurement with energy scan. Time-resolved PES measurements are also possible since synchrotron light has a time structure (pulse light). The development of energy analyzers has pushed the resolution of PES to less than 1meV, which allows us, for example, to measure the superconducting gap.

It is important to note that PES is in general a surface sensitive technique. Although light can penetrate deep into materials, PES cannot probe atoms located at the depth where the excitation light reaches. This is due to the fact that emitting electrons inelastically scatter with other electrons and thereby loss their kinetic energy. The scattering probability of electron traveling with the distance d in matter is give by

$$P = \exp(-d / \lambda) \tag{2.2}$$

where λ is called the "inelastic mean free path (IMFP)" or the escape depth.

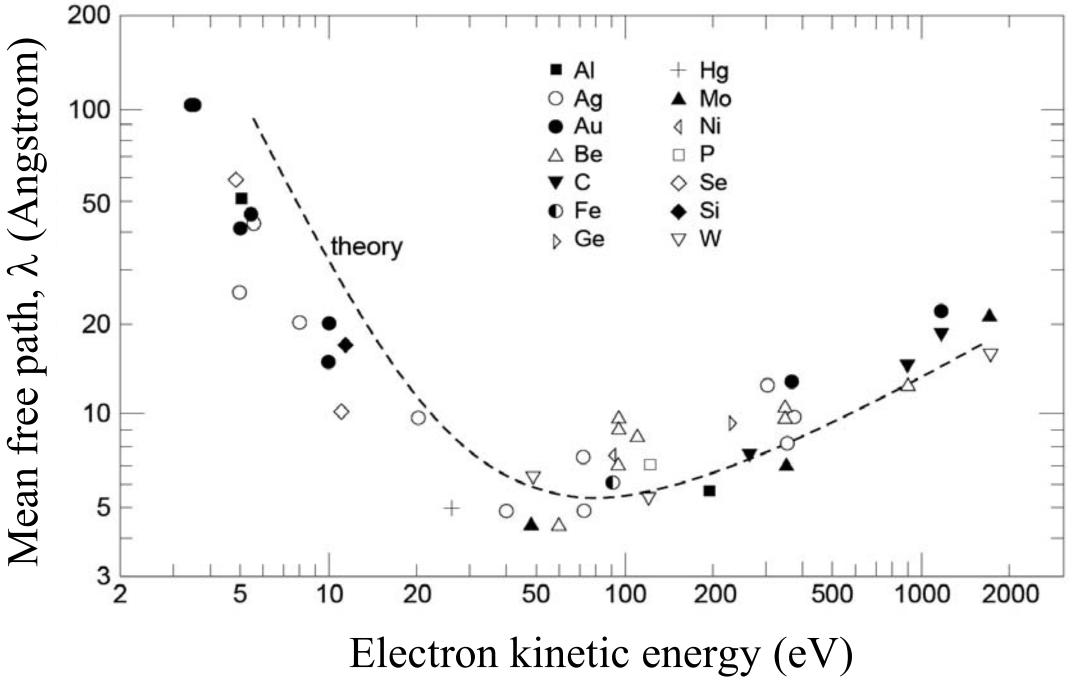

Figure 2.5 Universal curve, escape depth (Hofmann, 2005).

In gas phase experiments, photoemission, or specific named photoionization, are carried out by exposing gases with a beam of photons with photon energy higher that the binding energy of electrons to be excited. The kinetic energy of a photoelectron is the photon energy minus the electron binding energy. In this thesis, photoionization is used for characterization of the performance of the monochromator of the BL4 beamline. The kinetic energy of photoelectrons is the main interest. Secondary electrons, in addition to photoelectrons, are measured in a total electron yield mode. The spectral widths of measured atomic resonance depend on the instrumental resolution of beamline at particular photon energy and the natural widths of the specific resonances.

Gas-phase photoionization measurements were carried out using an existing analysis chamber designed for angle-resolved photoemission measurement. The measurement set-up is illustrated in Figure 2.6. A gate valve with a thin polypropylene window was used to vacuum-isolate the experimental chamber from the optical beamline, allowing the measurements to be carried out at pressures up to 10^{-6} mbar. It should be note that the channeltron must be operated at pressure below 5×10^{-5} mbar to avoid damage to the channeltron. A capillary tube was used to inlet a gas into the focal position of the beam. A secondary electron multiplier was installed within striking distance of gas nozzle to measure electron yield spectra. The size of Y aperture in the measurement is 4 mm, because the small aperture decreased the photon flux without a great improvement of the resolving power.

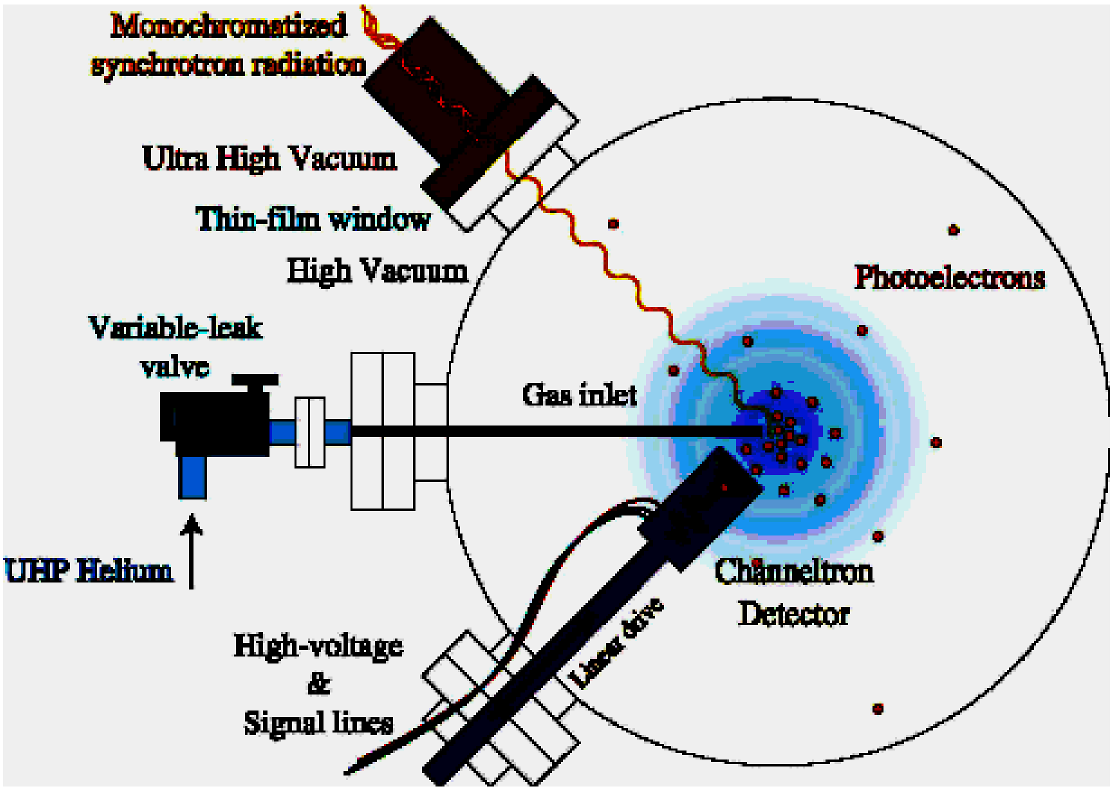

Figure 2.6 Photoionization experimental set-up.

2.4 Production of Vacuum

Surface analysis techniques such as PES require UHV environment to allow the measurement to be complete before an overlayer of residual gases is formed on the surface. This is also true for MBE/MBD. To achieve UHV, special care must be taken from the design to routine operations. Proper choices of materials for manufacturing of chambers and vacuum components are essential to minimize outgassing from the materials. Outgassing is caused by evaporating and sublimating of materials into vacuum. In the vacuum system, outgassing is considered as an “internal” leak. Another internal leak is caused by trapping of air inside a vacuum system, which can be avoided in the design stage. The vacuum system must be clean and free of organic matter to minimize outgassing. The most important outgassing in a clean man-made vacuum system is water absorbed on the internal wall of vacuum chamber or on the surface of vacuum components.

To created vacuum in a man-made vacuum system like the experimental station, the number of gas molecules must be reduced. There are different ways to reduce the number of gas molecules in a man-made vacuum system. The simplest method to remove gas molecules is by suction. Gas molecules in a vacuum system may be chemically combined into solid compound with very low vapour pressure or condensed on a very cold surface inside a vacuum system. Based on the mentioned method to reduce the number of gas molecules in a man-made vacuum system, different types of pumps have been developed such as mechanical pump, sputter-ion pump, getter pump and cryopump. Only the types of pumps relevant to this thesis will be mentioned below.

Mechanical pumps may subdivide into two main types. Those are a positive-displacement pump and a momentum transfer pump. In a positive-displacement pump, gas in a man-made vacuum system is mechanically trapped and subsequently compressed to the exhaust pressure. The simplest pump of this type is an oil-sealed rotary pump with or without gas ballast. A rotary pump may exist in a single or double stage. The gas ballast is normally used in the second stage of a double-stage rotary pump to prevent the formation of oil-water emission reducing the lubricating properties of oil. Water is also transported to the inlet of the pump, and thus the ultimate pressure is limited by the corresponding water vapour pressure. The rotary pump are cheap, however their disadvantage is possible contamination to the vacuum system caused by back-streaming of the lubricating oil. Thus, an oil trapping device installed between the inlet of the pump and the vacuum system may be used to minimize the contamination. Various positive-displacement pumps with more complicated mechanism have been developed to avoid possible oil contamination. Those pumps do not use lubricating oil, and thus are called dry pumps. Pumps in this category are piston pump, diaphragm, scroll, screw, claw and tongue pump. The ultimate pressure and the pumping speed of various positive-displacement pumps are shown in Table 2.2

Table 2.2 Ultimate pressure and pumping speed of various positive-displacement pumps (Hilleret , 1999-2005, pp.26-28).

Type	Ultimate pressure (Pa)	Pumping speed (m^3/h)
Rotary-piston pump	1	30 - > 1500
Rotary-vane pump (single state)	1	1 - > 300
Rotary-vane pump (double state)	2×10^{-2}	1 - > 300
Piston (3-4 state)	atm - > 4	12
Diaphram	atm - > 200	0.8 - > 5
Scroll	atm - > 1	15 - > 600
Roots (4 state)	atm - > 0.1	25 - > 1000
Screw	1	25 - > 2500
Claw (3 state)	atm - > 10	25 - > 500
Tongue/groove (4 state)	atm - > 5	50

Another type of mechanical pump is a momentum transfer pump, known as molecular and turbomolecular pump. The principle of this pump is based on the fact that momentum transfer to gas molecules in a preferential direction introduces a mean drift of the gas molecules towards the higher pressure region. Molecular pump was first proposed by Gaede (Gaede, 1913, quoted in Hilleret, 1999-2005) and latter by Holweck (Holweck, 1923, quoted in Hilleret , 1999-2005) and Siegbahn (Siegbahn, 1994, quoted in Hilleret , 1999-2005). The early versions of molecular pumps not in real uses as they were limited by its poor reliability and low pumping speed.

Advances in high-precision mechanical engineering, a molecular pump has further been developed and integrated as the first stage of turbomolecular pumps to improve the compression ratio. Thus we no longer see a stand-alone molecular pump. The implementation of rapidly rotating blades adds a prefix “turbo”. Turbomolecular pump was first proposed by Becker (Becker, 1958, quoted in Hilleret , 1999-2005). Turbomolecular pump become effective at pressure ~10^{-2} torr, as shown in Figure 2.7. To achieve high or ultra high vacuum, a turbomolecular pump must be used in a combination with a roughing pump, for example a rotary or diaphragm pump as illustrated in Figure 2.8.

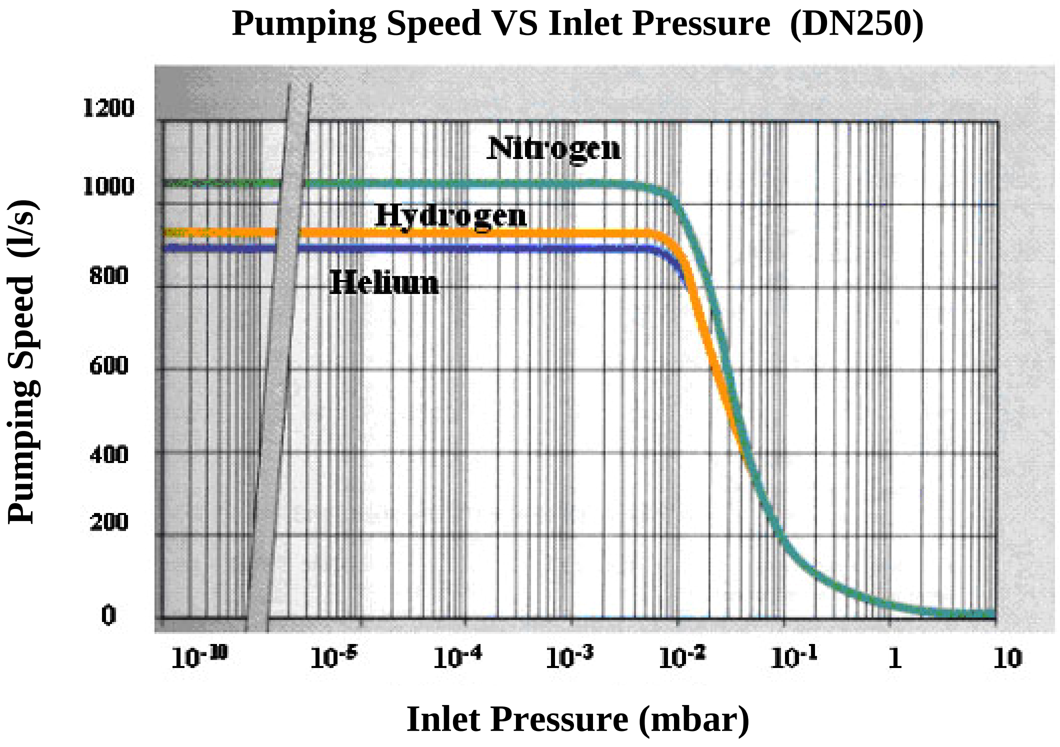

Figure 2.7 Pumping speed of a turbomolecular pump as a function of Pressure (Varian, 2006).

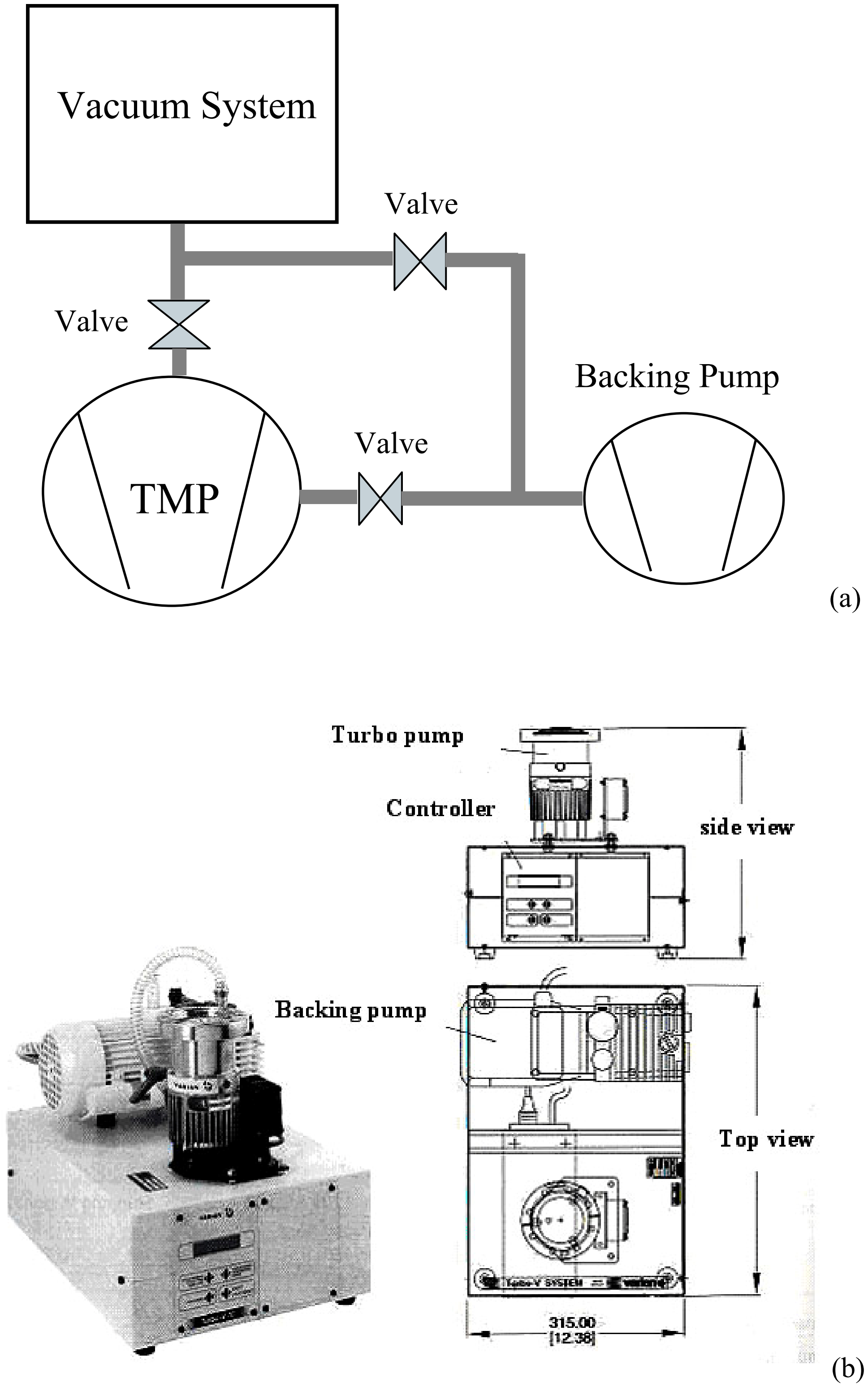

Figure 2.8 (a) and (b) Schematic diagram showing a set-up of a vacuum system using a turbomolecular pump with a roughing pump (Varian, 2006).

Sputter-ion pumps are often used in various UHV systems. The ion-sputter pumps are not mechanical pump, and thus have no mechanical movement. More importantly, ion sputter pumps consume very small electrical power when operating in the UHV region. However, they are no suitable for operating at high gas load. The principle of sputter-ion pumps is based on sorption process of ionized residual gases. A sputter-ion pump consists of many individual Penning cell connecting in parallel. The number of the cell primarily determines the speed of the pump. Figure 2.9 shows a diagram of a Penning cell, consisting anode, cathode and a magnet. Normally, the anode is made of stainless steel cylindrical tube. The titanium cathode plates are placed on both side of the anode tube. Field emission electrons from the cathode are accelerated by the electric and magnetic fields. The energy of the electrons are in the range of up to ~7 kV. Residual gases can be ionized when collided by the energetic electrons. The ionized gas molecules are accelerated by the anode voltage and moved directly to the cathode. The ions sputter titanium from the surface. The sputtered titanium deposited on neighboring surfaces, mainly on the anode making this region become reactive to getter molecules of residual gases. There are two main types of sputter-ion pump. Those are diode and triode sputter-ion pumps. The above described pump is the diode type. The diod and triode type is illustrated in Figure 2.10. The triode configuration prevents the problem with instability when pumping noble gases such as argon. It should be noted also that the operating range for sputter-ion pumps is from ~10^{-4} torr to ~10^{-10} torr. Thus, it is necessary to pre-evacuate the system with a turbomolecular pump before turning on sputter-ion pumps.

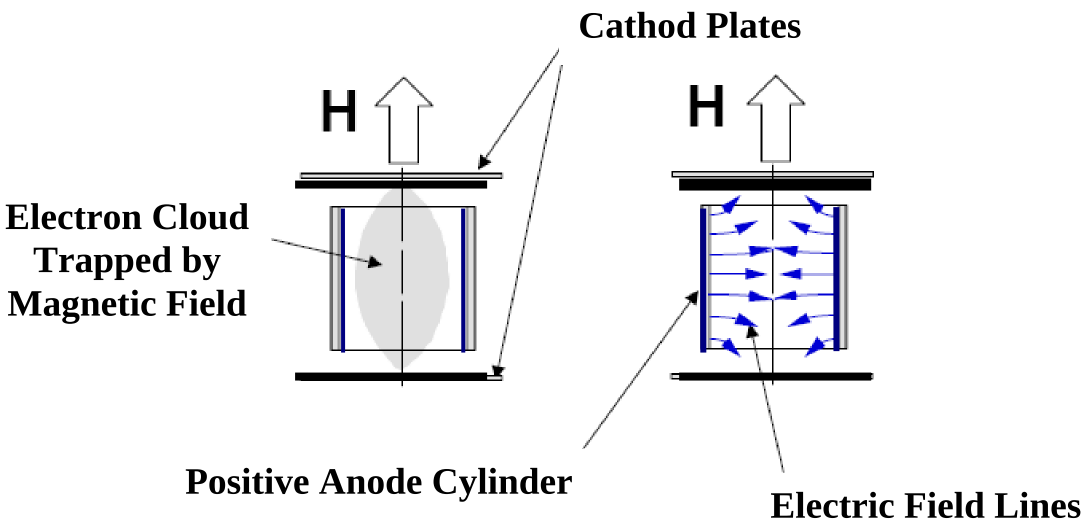

Figure 2.9 A Penning cell in sputter-ion pumps.

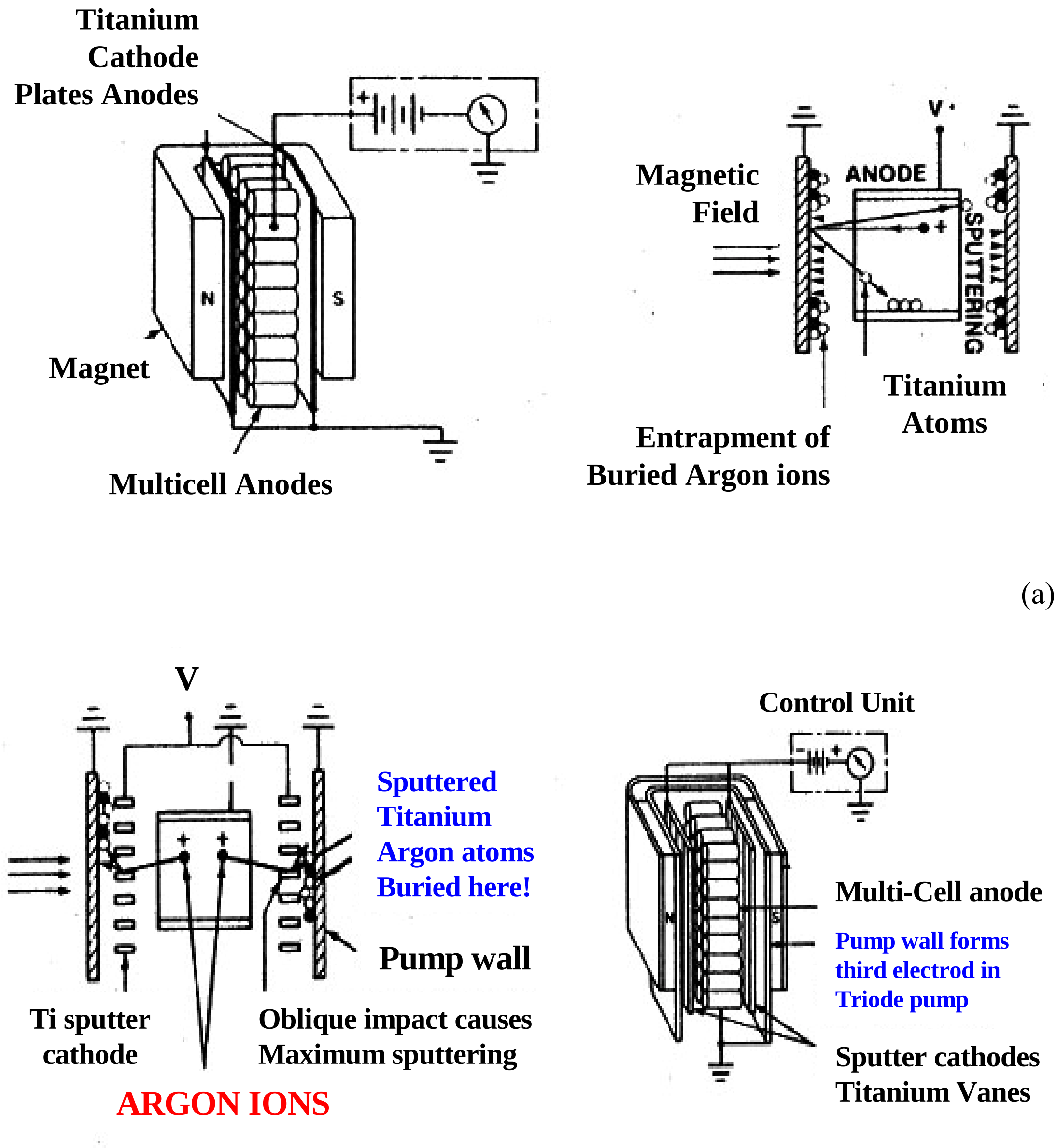

(a)

(b)

Figure 2.10 Diode cell (a) and Triode cell (b) of sputter-ion pump (Bertolini, 2004; Reproduce, 2007).

2.5 Measurements of Vacuum Pressure

Vacuum is measured in the units of pressure, an amount of force perpendicularly acting on a unit area. Pascal or N/m^2 is the SI unit of pressure. Often vacuum is measured in Torrs or mbar. Torr unit is named after an Italian physicist Torricelli. A Torr is equivalent to the displacement of a millimeter of mercury. Table 2.3 shows conversion factors for units of pressure.

Table 2.3 Conversion factors for units of pressure (Berman, 1992).

	Pa (N/m^2)	mbar	Torr (mm Hg at 0 °C)	Technical Atmospheres (at)	Physical Atmospheres (atm)
Pa (N/m^2)	1	1.0×10^{-2}	7.5×10^{-3}	1.02×10^{-5}	9.87×10^{-6}
mbar	1.0×10^{2}	1	7.5×10^{-1}	1.02×10^{-3}	9.87×10^{-4}
Torr (mm Hg at 0°C)	1.33×10^{2}	1.33	1	1.36×10^{-3}	1.32×10^{-3}
Technical Atmospheres (at)	9.80×10^{4}	9.80×10^{2}	7.36×10^{2}	1	9.68×10^{-1}
Physical Atmospheres (atm)	1.01×10^{5}	1.01×10^{2}	7.60×10^{2}	1.03	1

There are many different devices for measuring the pressure in a vacuum system, depending on the range of vacuum. The operation principles of the devices used in this thesis only will be mentioned briefly.

For low vacuum, vacuum gauges based on thermal conductivity are used. It is note that the ability of a gas to conduct heat decreases with pressure. In this type of gauge, a wire filament is resistively heated by running current through. The temperature of the filament is measured by a thermocouple (TC) or resistance temperature detector (RTD). The heated filament can also be RTD such as in the Pirani gauge, in which a platinum filament is used.

Ion gauges are used in high and ultra high vacuum regions. The principle of ion gauges is based on the measurement of density of gas, n, at known temperature, T. The pressure is given in the following relation

$$P = nkT \tag{2.3}$$

where k is Boltmann's constant (1.38×10^{-23} J/K). The density of gas molecule is measured through the ion current ionized by emitted electron from the cathode. There two different types subdivided according to the way electrons are produced from the cathode: hot cathode and cold cathode. The accurate operating ranges for cold cathode and hot cathode gauges are $10^{-2} - 10^{-9}$ torr and $10^{-3} - 10^{-10}$ torr, respectively. In hot cathode gauges, the cathode filament is heated by running current though and emits thermal emission electrons. The electrons travel and ionize gas molecules in the gauge. The ionized gases are collected by a negative collector. The ion current collected by the collector is converted to be the gas density. The principle of cold cathode gauges is the same as that of hot cathode gauges, except that, electrons are produce by discharging from a high-voltage biased cathode. In UHV systems, the composition of gas species is usually unpredictable, so a residual gas analyzer must be used in a combination with vacuum gauges for accurate measurements.

2.6 Auger Electron Spectroscopy

Auger Electron Spectroscopy or AES is one of important surface analysis techniques. It is the most commonly used for determining the elemental composition of the surface layers of solids. The technique was developed in the late 1960’s, is based on the phenomenon first observed by a French Physicist Pierre Auger in the mid-1920’s. The Auger is one of a decay channel where energetic electron is emitted after an atom is excited. The Auger process is illustrated by the energy diagrams in Figure 2.11. First, an atom in a sample is excited by a photon or an energetic electron to create a core hole. In Figure 2.11, the core hole is created in the K-shell. The ionized state is not stable, and thus the exited state will retune to ground state either by X-ray fluorescence channel or Auger electron emission channel. In the Auger emission decay channel, an electron transitions from a higher energy level (i.e. L_1) to fill the initial core hole in the K-shell. The energy releases in this transition is simultaneously transferred to a second electron (i.e. $L_{2,3}$). A fraction of this energy is required to overcome the binding energy of this second electron, the remaining fraction is retained by this emitted *Auger electron* as kinetic energy. As shown in the figure, the final state of the Auger process is a doubly-ionized atom with core holes in the L_1 and $L_{2,3}$ shells.

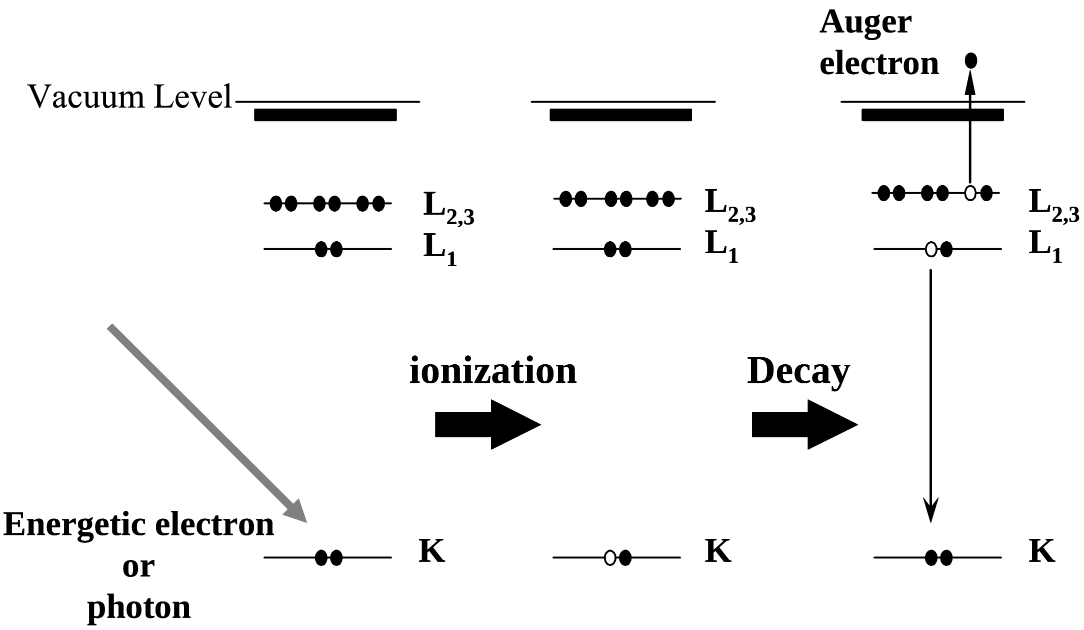

Figure 2.11 The energy diagrams showing the Auger emission process.

It is obvious that an Auger process is characterized primarily by the energy level of the initial hole and the energy level of the final two holes. AES is thus the technique based on the measurement of the kinetic energies of the emitted electrons. The kinetic energy of the Auger electron illustrated in Figure 2.11 may be estimated from the binding energies of the level K, L_1 and $L_{2,3}$ as follow:

$$KE = (E_K - E_{L_1}) - E_{L_{23}} \tag{2.4}$$

It is noted that the transition illustrated is a $KL_1L_{2,3}$ transition. There are also other Auger possible transition such as K L_1 L_1, K L_1 $L_{2,3}$ and K $L_{2,3}$ $L_{2,3}$ transitions. Thus, each element in a sample being measured will give rise to a characteristic spectrum of peaks at various kinetic energies. . For more accurate estimation of the binding energy $E_{L2,3}$ must be the binding energy of an ionized atom since one electron (in L_1 level) has already left the atom. To a good approximation for most purpose, the kinetic energy of Auger electron with a ABC transition may be estimated from the Chung and Jenkins'expression (Chung and Jenkins, 1970), for an atom of atomic number Z,

$$KE = E_A(Z) - \frac{1}{2}\{E_B(Z) + E_B(Z+1)\} - \frac{1}{2}\{E_C(Z) + E_C(Z+1) \qquad (2.5)$$

In most AES systems, an electron gun with energy about 1-10 keV is used as an excitation source and the kinetic energies of the resultant Auger electrons are typically 0.03-1 keV. As already mentioned in the previous section, electrons with such kinetic energies have the escape depth or the mean free path of less than 1 nm, see Figure 2.5. Thus AES is a surface sensitive technique. In this thesis work, AES is used for detecting impurities on surfaces to verify the cleanliness of the surface and used for determining the amount of the growth/deposited materials of an overlayer.

2.7 Low-Energy Electron Diffraction

Low-energy electron diffraction or LEED has long been known as a technique to determine surface crystal structures. The technique is surface sensitive. This is due to the fact that the mean free path for low energy electron is very short, as mentioned in the previous section. The energy of electrons used in the measurement is about 10 – 300 eV. Electrons with in energy in this range have the electron de Broglie wave length, $\lambda = \hbar/p$, about the same as the typical distances in surface crystals and thus diffraction phenomena are occurred.

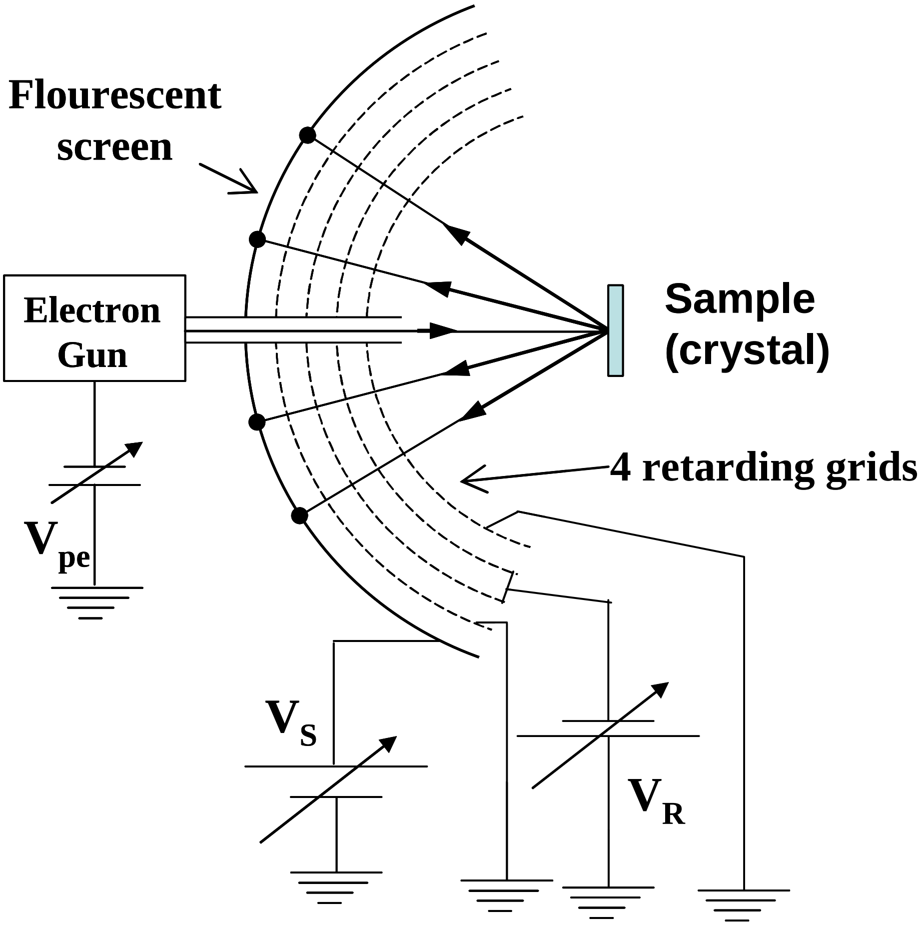

Figure 2.12 The schematic diagram of typical LEED apparatus.

Figure 2.12 shows the schematic diagram of typical LEED apparatus. The LEED set-up is simple consisting of two main components, i.e. an electron gun for producing monochromatic electrons and a detector. The detector consists of a fluorescence screen and three or four metal grids biased at different voltage. For a four grid detector, the first grid from the sample is on ground potential to make sure that there is no electrical field around the sample. The middle two grids are biased with voltage slightly lower than the kinetic energy of the elastically backscattered electron, the kinetic energy of the electron produced by the gun. Proper biased voltage of the middle two grids expels or removes nearly all secondary or in-elastically scattered electrons. The forth grid is on ground potential to extract the elastic electrons on further accelerated by the high electric field between the forth grid and the screen, which is bias with a high positive potential. The LEED pattern on the screen can be view from the front or the rear of the screen, and normally recorded with a video camera.

A quantitative explanation of LEED pattern can be discussed through the conditions for diffraction of low-energy electron with a two dimensional lattice, which are given by the following Laue conditions:

$$(\vec{k}_i - \vec{k}_f)\vec{a}_1 = 2\pi h, \qquad (\vec{k}_i - \vec{k}_f)\vec{a}_2 = 2\pi k \tag{2.6}$$

or

$$\Delta\vec{k}_{//} = h\vec{g}_1 + k\vec{g}_2 \tag{2.7}$$

and

$$\left|\vec{k}_f\right| = \left|\vec{k}_i\right| \tag{2.8}$$

where *h* and *k* are arbitrary integers, a1 and a2 are the unit vector of the surface crystal and $k_{//}$ is the momentum transfer parallel to the surface. The Laue conditions can be illustrated by the Ewald sphere, shown in Figure 2.13. A reciprocal lattice rod pass through every point of the surface reciprocal lattice. The energy of the electron or the magnitude of the electron wave defines the radius of the Ewald sphere. The diffraction id satisfied for every beam that emerges in the direction along which the sphere intersects a reciprocal rod.

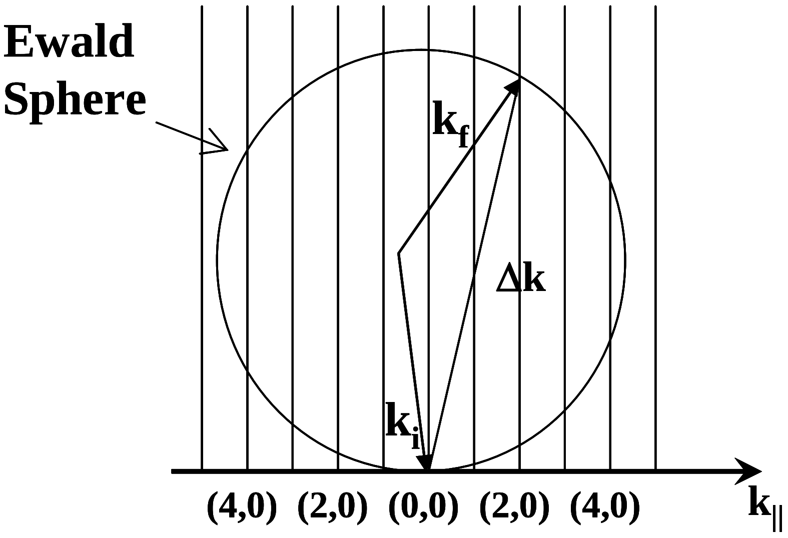

Figure 2.13 The Ewald construction for diffraction of surface lattice.

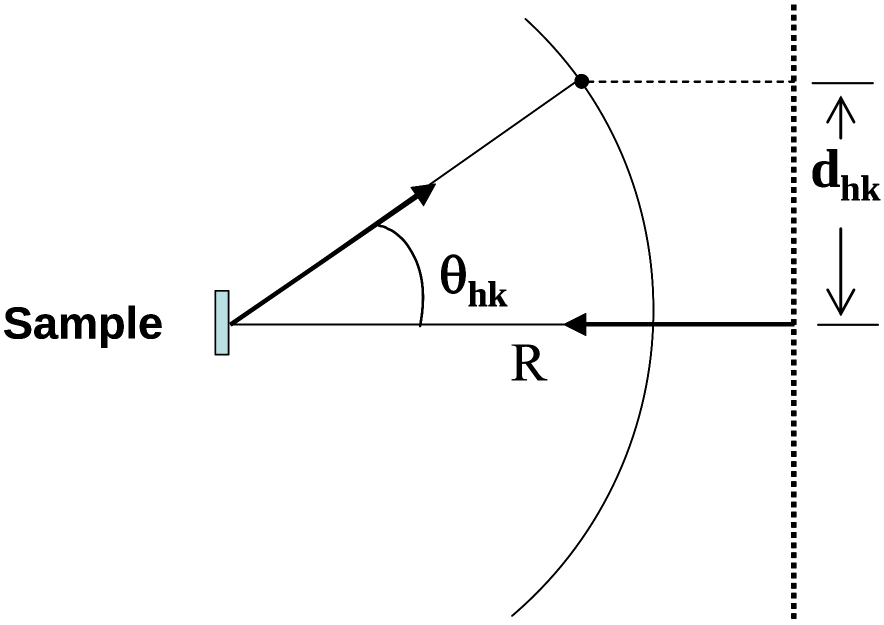

Figure 2.14 Schematic showing the linear LEED image of the reciprocal lattice.

Normally, LEED patterns are taken with normal incident electron beam, i.e. $\vec{k}_{//}$ is zero. The emission of the outgoing electrons is given by the following relation

$$\sin\Theta_{hk} = |\vec{k}_{\|}| / |\vec{k}| \tag{2.9}$$

The high intensity of outgoing electrons must satisfied eq. (2.9). If one views LEED patter from the rear of the fluorescence screen, one will find the position of the intensity maxima on the window with the distance from the center of the screen/window of d_{hk}, which is given by

$$d_{hk} = R\sin\Theta_{hk} = \frac{R}{|\vec{k}|}(h\vec{g}_1 + k\vec{g}_2) = R\sqrt{\frac{h^2}{2m}}\frac{1}{E^{1/2}}(h\vec{g}_1 + k\vec{g}_2) \tag{2.10}$$

2.8 Reflection High-Energy Electron Diffraction

The physics behind reflection high-energy electron diffraction or RHEED is the same as that of LEED. The only differences are the energy of the electrons; RHEED employs about 15-30 keV electrons while LEED uses electrons with energy lower than 300 eV. The high energy of electron in RHEED system allows RHEED measurements be carried out with a grazing incidence angle configuration. Figure 2.15 shows schematic diagram of a set up for RHEED measurements. The electron beam from the gun hit the sample at a grazing angle of about 1-3 degrees. The electrons are diffracted by surface crystal structure and impinge on a phosphor screen. The resulting RHEED pattern is a series of streak.

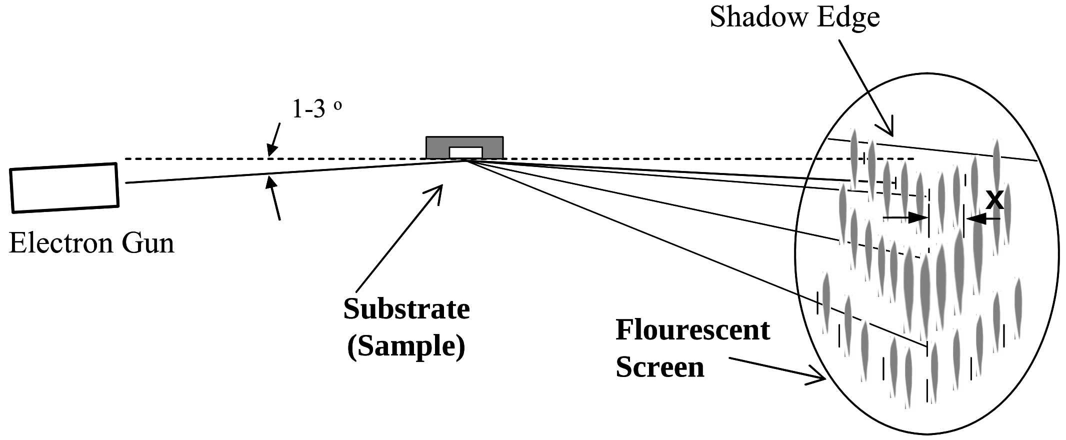

Figure 2.15 Schematic diagram of RHEED experimental set up.

The grazing incidence angle ensures surface specificity though the incident electrons have high energy. Sharp LEED patterns are observed when a surface is atomically flat. The sharpness reduces when the surface becomes rougher. RHEED has long been used in MBE systems as a tool for calibrating the growth rate on a daily basis. The growth rate can be measured in a real time mode. The thickness determined by RHEED oscillation is very accurate, this is one of the advantages of the MBE growth technique.

Figure 2.16 schematically shows the mechanism of RHEED intensity oscillation during MBE growth of a monolayer. The figure shows the case of the growth of a perfect crystal with a two-dimensional growth fashion. One period of the RHEED intensity oscillation is equivalent to coverage of an overlayer of one monolayer. However, there are some precautions when using RHEED for calibrating of MBE growth. First, there might be some growth transients when shutters are open because of the shielding effects of the shutter of the sorces. Second, part of the growth rate is not sensed by the RHEED oscillations i.e. those atoms that can migrate and get incorporated at step edges resulting in no change of the surface roughness.

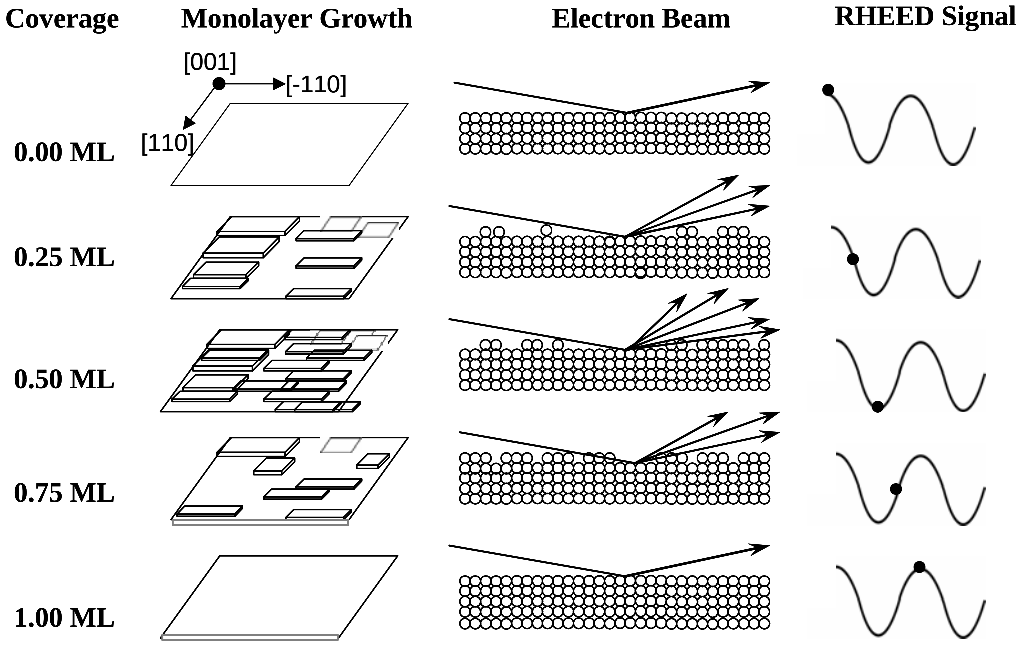

Figure 2.16 Mechanism of RHEED intensity oscillation during MBE growth of a monolayer (Ploog, 1988).

CHAPTER III

DEVELOPMENT OF EXPERIMENTAL STATION

This chapter provides the description for the design considerations, the design and commissioning results of the new experimental station of the BL4 beamline of SPL developed along the course of this thesis work. The new experimental station is an upgraded station of the original angle-resolved photoemission system. The original experimental station is used mainly for ARPES and AIPES experiments using synchrotron light with photon energy between 20 – 240 eV. Detailed descriptions of the original experimental station are given in Chapter 2. In short, the original system has three vacuum-isolated chambers, i.e. the analysis chamber, the sample preparation chamber and the load-lock chamber. The sample preparation chamber is mounted on top of the analysis chamber with a gate valve in between. The relocation of the sample between the preparation and analysis chambers is performed by a vertical linear movement of the manipulator. Surface cleaning of a crystalline sample may be performed by ion sputtering or/and heating in the preparation chamber. Although photoemission spectroscopy is a very powerful tool for studies of occupied electronic states of solids, it is very surface-sensitive. Clean surfaces are required to obtain useful information from photoemission measurements. For ARPES, well-defined surfaces are also necessary. For some materials, it takes a few months to obtain clean and well-defined surfaces for photoemission measurements. The disadvantage of the original experimental station is that sample preparation and photoemission measurement cannot be performed at the same time since the sample preparation chamber and the analysis chamber share the common sample manipulator. This limits the number of samples to be investigated at the BL4 beamline. To make the most use of synchrotron light for photoemission experiments in limited allocated beamtimes, samples must be prepared and characterized before they are transferred into the photoemission system. Thus, in this thesis, the original experimental station has been upgraded with a multi-UHV-chamber system to allow photoemission measurements to be performed while preparing or/and characterizing other samples. This will remove the disadvantage and will expand the capabilities of the experimental station of the BL4 beamline. More importantly, the metal MBE/MBD system has also been developed and connected to the the multi-UHV-chamber system.

3.1 Design Considerations

The main goal for the upgrade of the experimental station of the BL4 beamline is to serve the increasing demands and the number of users. The demand for more efficient use of allocated synchrotron light beamtimes can be satisfied with the use of a multi-UHV-chamber system to allow photoemission measurements using synchrotron light to be performed in parallel with the preparation and/or with *in situ* surface analysis of other samples. The major aim in the design of the new experimental station is also to ensure variability, i.e., provide a multiple propose experimental station for surface and interface research, where a number of surface analysis techniques are available. More importantly, the techniques are *in situ* techniques. The standard surface-sensitive techniques available in addition to ARPES and AIPES using synchrotron light are ultraviolet photoelectron spectroscopy (UPS), X-ray photoelectron spectroscopy (XPS), Auger electron spectroscopy (AES), and low-energy electron diffraction (LEED). Future planned upgrades will include STM and surface magneto-optical Kerr effect (SMOKE) measurement techniques. The availability of STM will provide atomic scale experimental results to be compared with those obtained by surface-averaged techniques such as photoemission and LEED.

Sample preparation systems of users will also be possible to be connected to the new experimental station to utilize the *in situ* analysis techniques. The connection or disconnection of the extra sample preparation systems will not interfere with the rest of the system, i.e. no breaking the UHV condition. In parallel with this upgrade, a metal molecular beam epitaxy (MBE) system has been constructed and attached to the multi-UHV-chamber system. The MBE will be used for depositing or growing ultra-thin metal films on various substrates for the studies of ultra-thin magnetic films and metal-semiconductor interfaces. In combinations with the analysis techniques mentioned above, the MBE system will open the possibility for the investigations to find the relationship between the arrangement of atoms, electronic structure, atomic scale surface morphology and macroscopic properties (magnetic or electrical properties) of the ultra-thin metal films.

3.2 Design of a New Experimental Station

The new experimental station includes the existing photoemission system and a multi-UHV-chamber system, as schematically shown in Figure 3.1. The photo of the upgraded experimental station installed at the BL4 beamline is also shown in Figure 3.2. The essential part of the multi-UHV-chamber system is the sample transfer system, which consists of grips, mechanical hands, transfer rods and linear and radial sample transporters. With the transfer system, samples can be transferred among different UHV chambers providing the possibility for *in situ* studies.

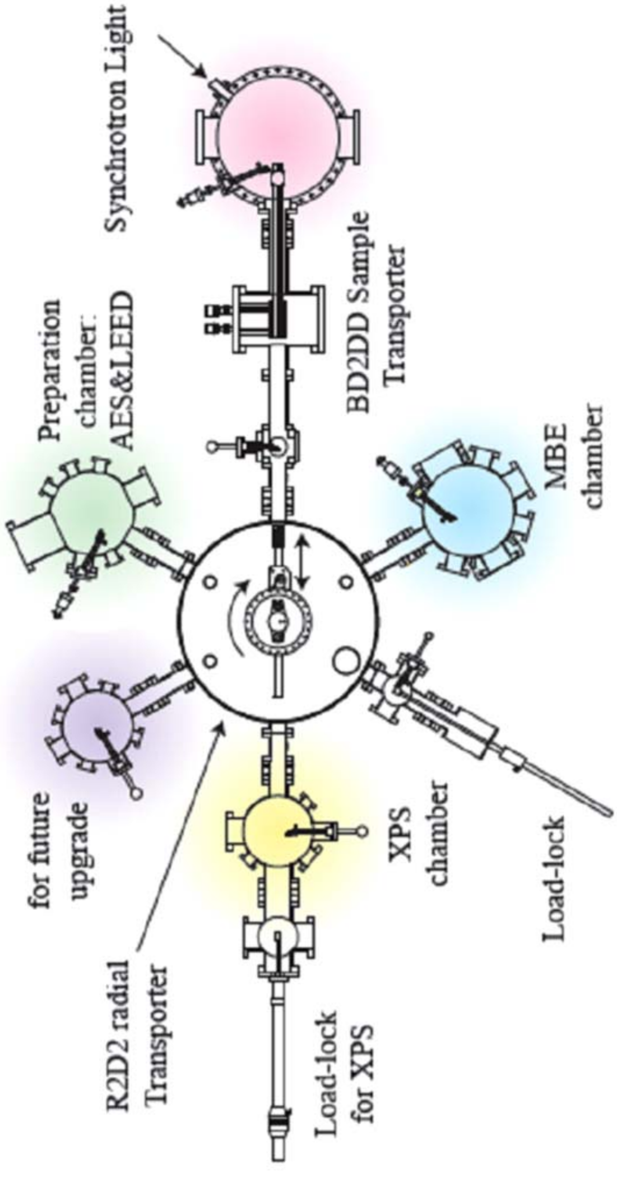

Figure 3.1 The schematic diagram of the upgraded experimental station of the BL4 beamline.

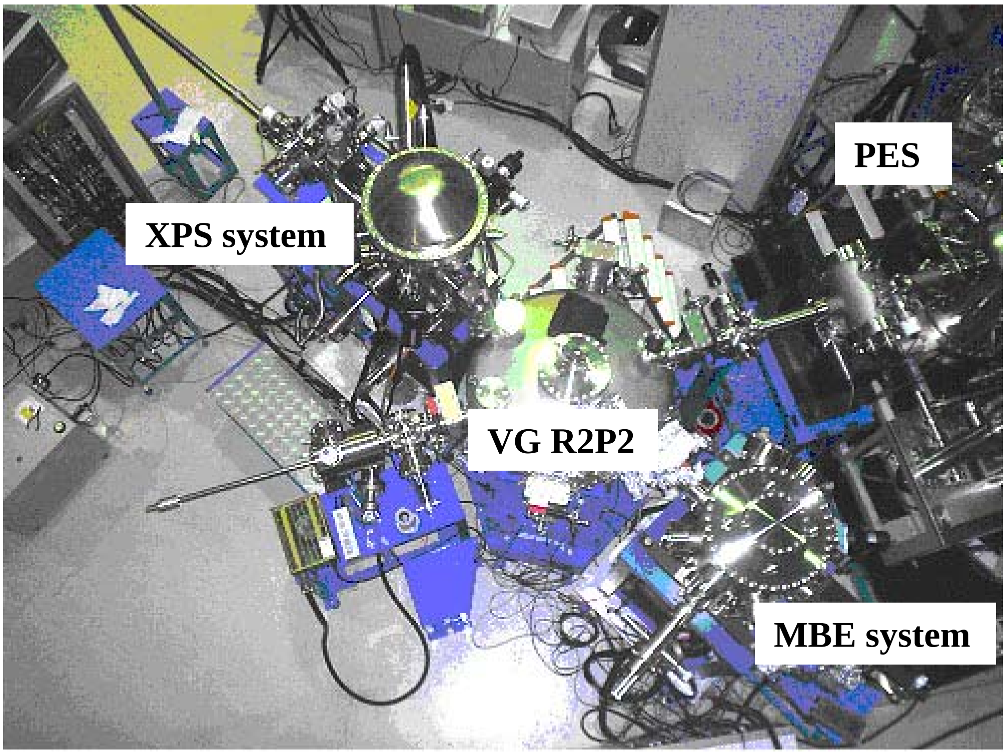

Figure 3.2 The photo of the upgraded experimental station of the BL4 beamline.

The operating principle of the VG R2P2 radial sample transporter is based on the mechanism of the VG linear rack and pinion transporter. As illustrated in the drawing in Figure 3.3, a single ended rack and pinion is mounted on a rotary drive, which is installed on the middle top port of a circular vacuum vessel. The single ended rack and pinion can be rotated until it is aligned in a preset position, the position where the rack is aligned with the radial port. At the present position, the rack can be locked in position by a rack positioning plunger. Once it is locked, the rack can be linearly moved out and in through the radial port by the same rotary drive. At one end of the rack, a storage carousel is attached to allow sample storage up to 11 samples and to allow transfer from chamber to the others. The design of the home-made carousel is shown in small figure of Figure 3.4. Figure 3.5 is the side-viewed photo of the R2P2 transfer system.

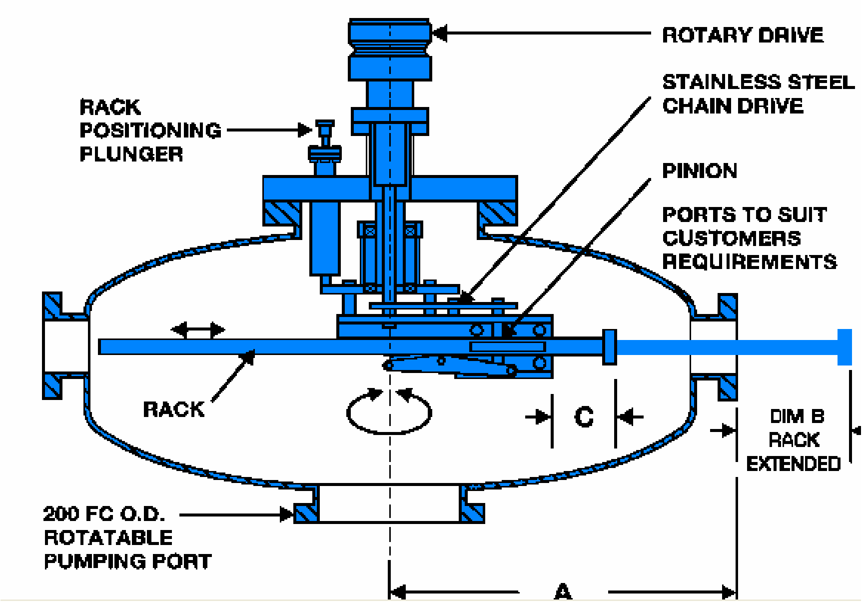

Figure 3.3 A drawing of the VG R2P2 radial sample transporter showing the movement mechanism in the vessel (Thermo VG Scientific).

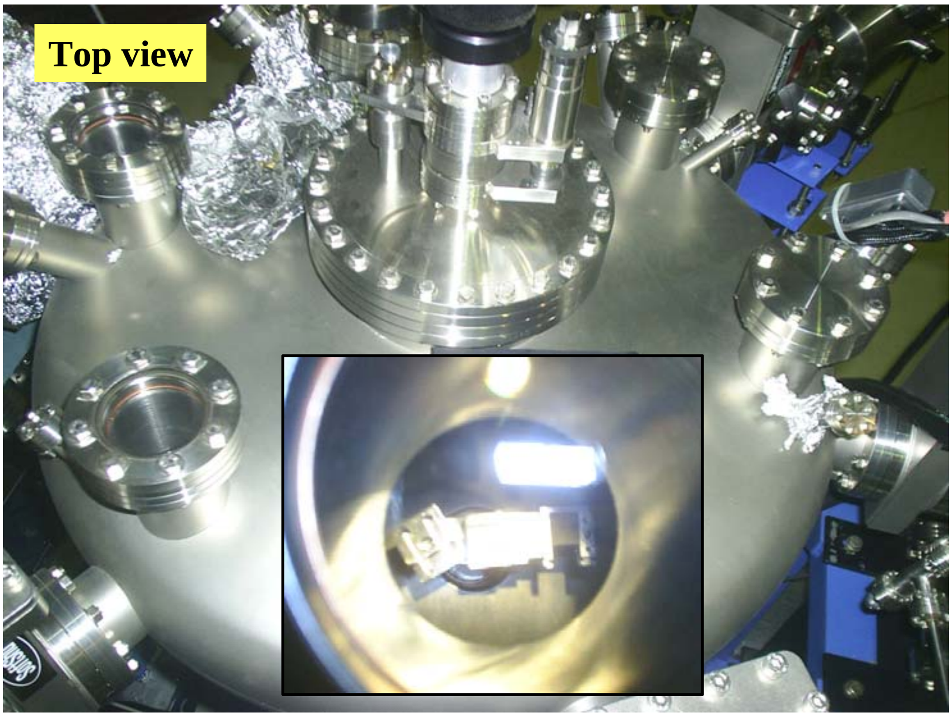

Figure 3.4 The photo of the VG R2P2 radial sample transporter (top view), the home-made carousel in the VG R2P2 chamber was shown in small figure.

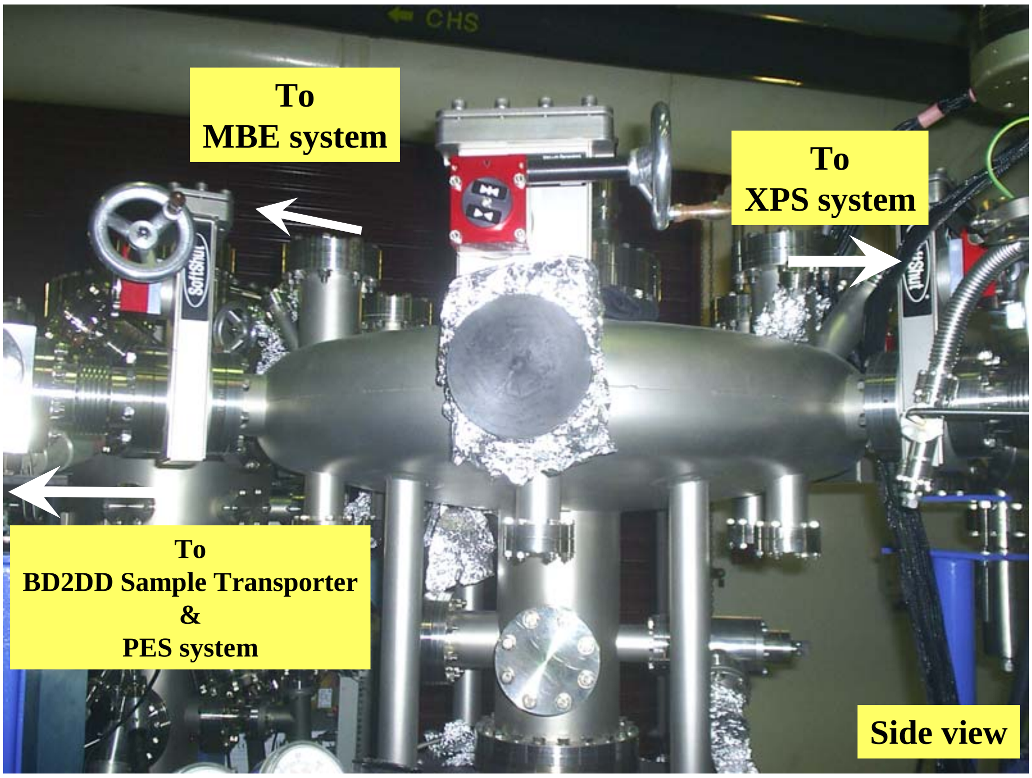

Figure 3.5 The photo of the VG R2P2 radial sample transporter (side view).

The VG R2P2 transporter used in the upgraded experimental station of the BL4 beamline has six connecting radial ports, and thus there are six preset position of the rack. Up to six UHV chambers can be connected to the VG R2P2 sample transporter in such a way that the sample transporter is placed at the center of chambers and form a central hub for which the sample transfer takes place. At the present status, only four ports of the sample transported are used to connect with the existing photoemission system, an additional XPS system, a metal MBE system and a load-lock chamber. The remaining two ports are designed for an additional sample preparation and a SMOKE (surface magneto-optic Kerr effect) system. The preparation system has also developed along this thesis work. However, the system is not connected to the VG R2P2 sample transporter due to the space limit. The vacuum environment of each system can be isolated by closing the gate valves, which are installed between each system and the radial transporter. Between the photoemission system and the radial transporter, the VG DB2DD linear sample transporter is used to provide sufficient working space. Mechanical hands and grips are used for moving the sample between the sample manipulators and the sample carriers of the transporters or of the transfer rods.

Samples can be introduced into the multi-UHV-chamber system without breaking UHV conditions via two different directions, i.e. via the load-lock chamber connected to the radial transporter or via the load-lock chamber of the XPS system.

3.2.1 The XPS system

The original photoemission system has a twin-anode X-ray tube and thus XPS measurement can be carried out in the analysis chamber using either the CLAM2 or ARUPS10 energy analyzer. However, XPS measurements in the analysis chamber prevent synchrotron light photoemission experiments. More importantly, the majority of users of the BL4 experimental station is the XPS users. Thus a dedicated XPS system has been developed to support XPS activities and allow synchrotron light photoemission experiments can be conducted without interruption by XPS users.

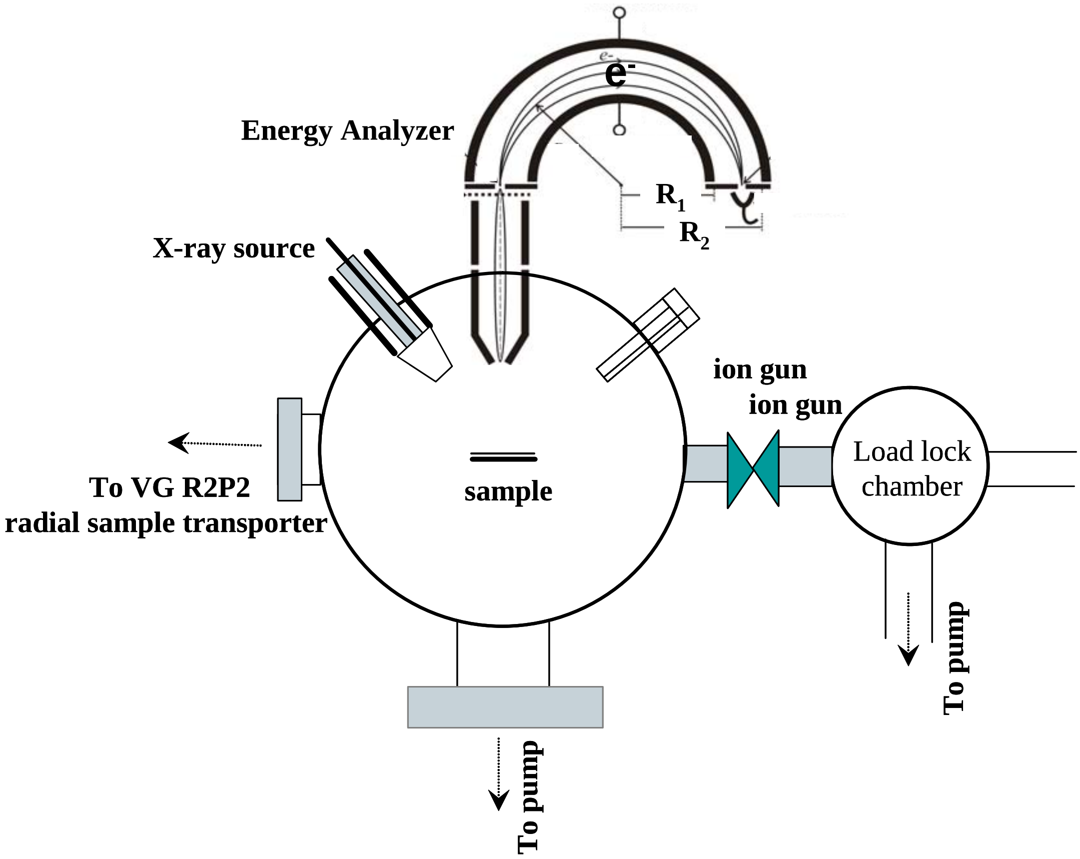

Figure 3.6 Schematic diagram of the new XPS system.

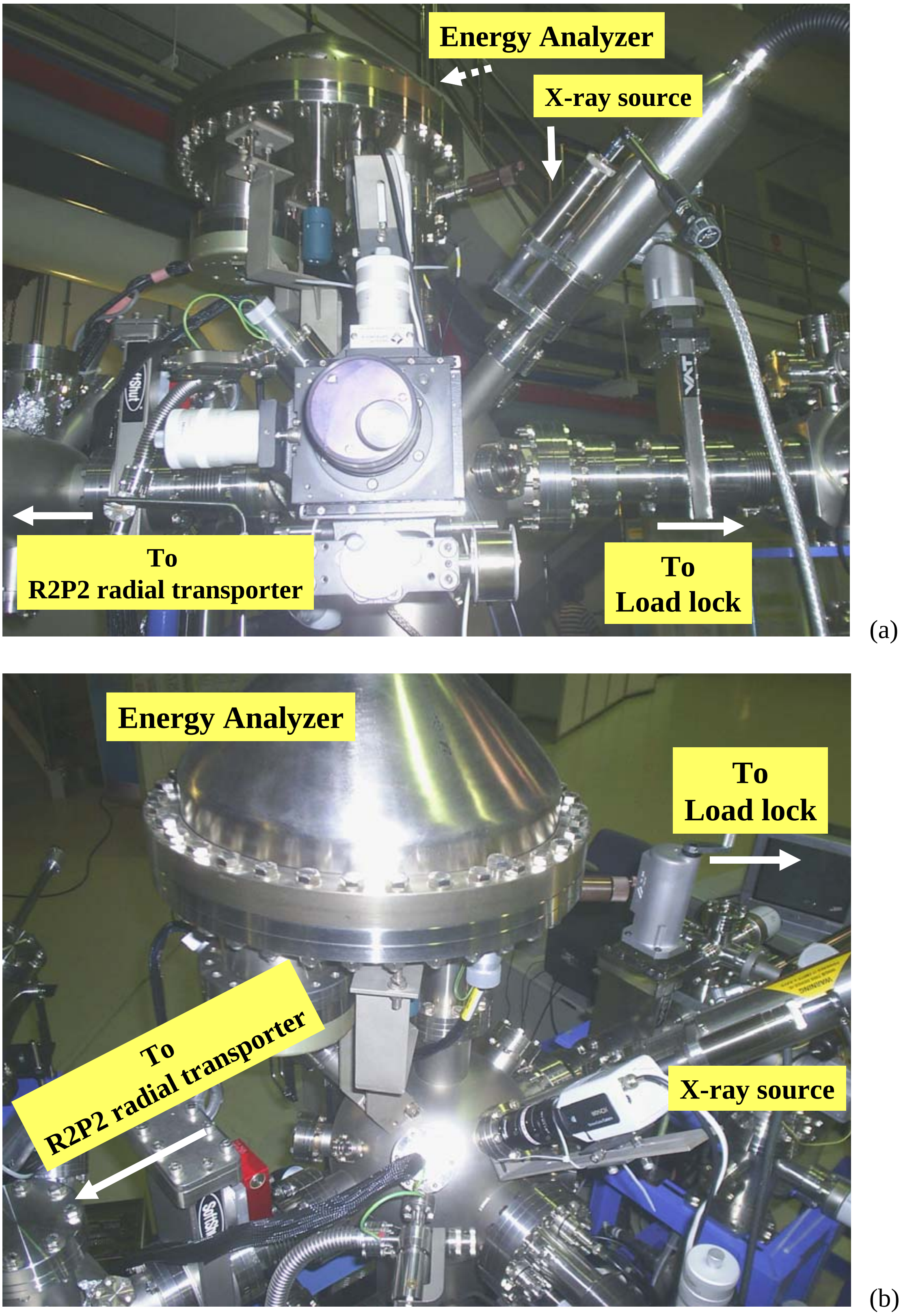

Figure 3.7 Photoes of the new XPS system at the BL4 beamline, (a) and (b).

Figures 3.6 and 3.7 show the schematic diagram and photoes of the new XPS system. The spherical chamber of the XPS system is made of mu-metal to prevent external magnetic field to disturb the orbit of photoelectrons. The XPS system was designed to have its own load-lock system to allow samples to be introduced directly into the XPS system since the XPS system is mainly used for routine chemical analysis. The main XPS analysis chamber is evacuated by a Varian 500 l/s star-cell sputter-ion pump with a titanium sublimation pump. The load-lock chamber can be pump down by a turbomoleculare pump backed by a rotary pump.

The new XPS system employs a Thermo VG Scientific alpha 110 electron energy analyzer. The mean radius of the analyzer is 110 mm. The detector of the analyzer comprises of seven channeltrons. The analyzer is installed downward in order to measure the sample horizontally placed on the sample holder. An electron flood gun is also installed for charge compensation. Surface cleaning of the sample is also possible with Ar^+ ion sputtering in the XPS. The X-ray source of the new system was relocated from the original photoemission system.

3.2.2 Metal MBE/MBD system

A metal MBE/MBD system has been developed during the course of this thesis work in order to prepare ultra-thin metal films. The schematic of the MBE/MBD system is shown in Figure 3.8. The photos of the MBE/MBD system are also shown in Figure 3.9. The growth/deposition is evacuated by a Varian star-cell 500 l/s sputter-ion pump in a combination with a titanium sublimation pump. The chamber has four CF114 ports and four CF70 ports for possible sources for MBE/MBD processes. Only one CF114 port is used for a high temperature effusion with an integrated shutter. A mini electron-beam co-evaporator is installed at one of the CF70 ports. The evaporator can accommodate four different solid sources simultaneously.

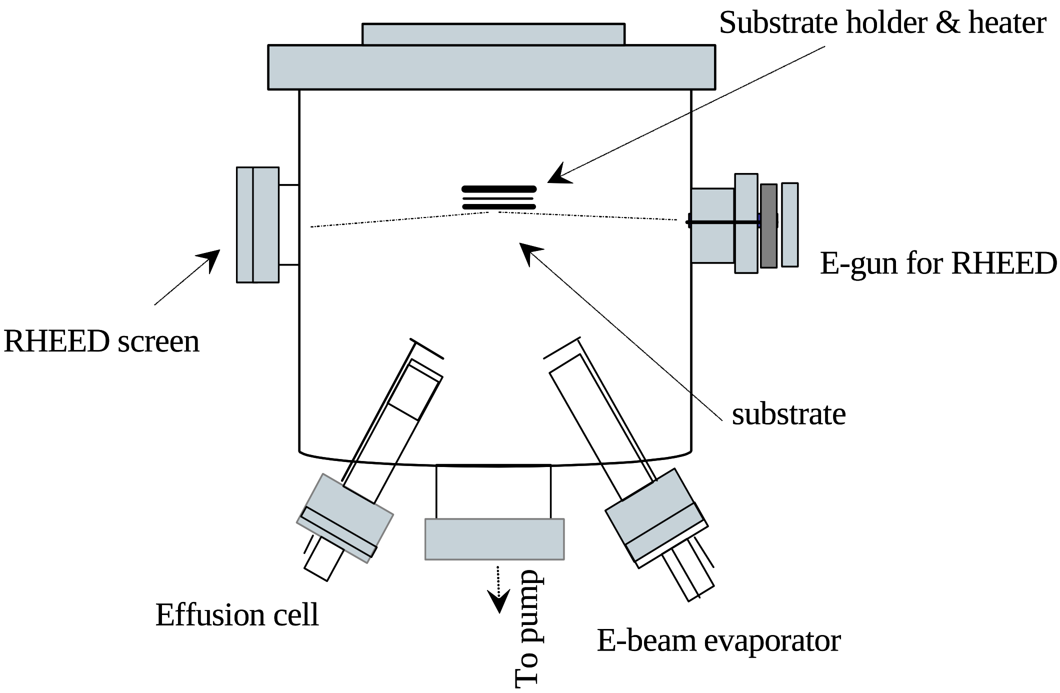

Figure 3.8 The schematic of the MBE/MBD system at the BL4 beamline.

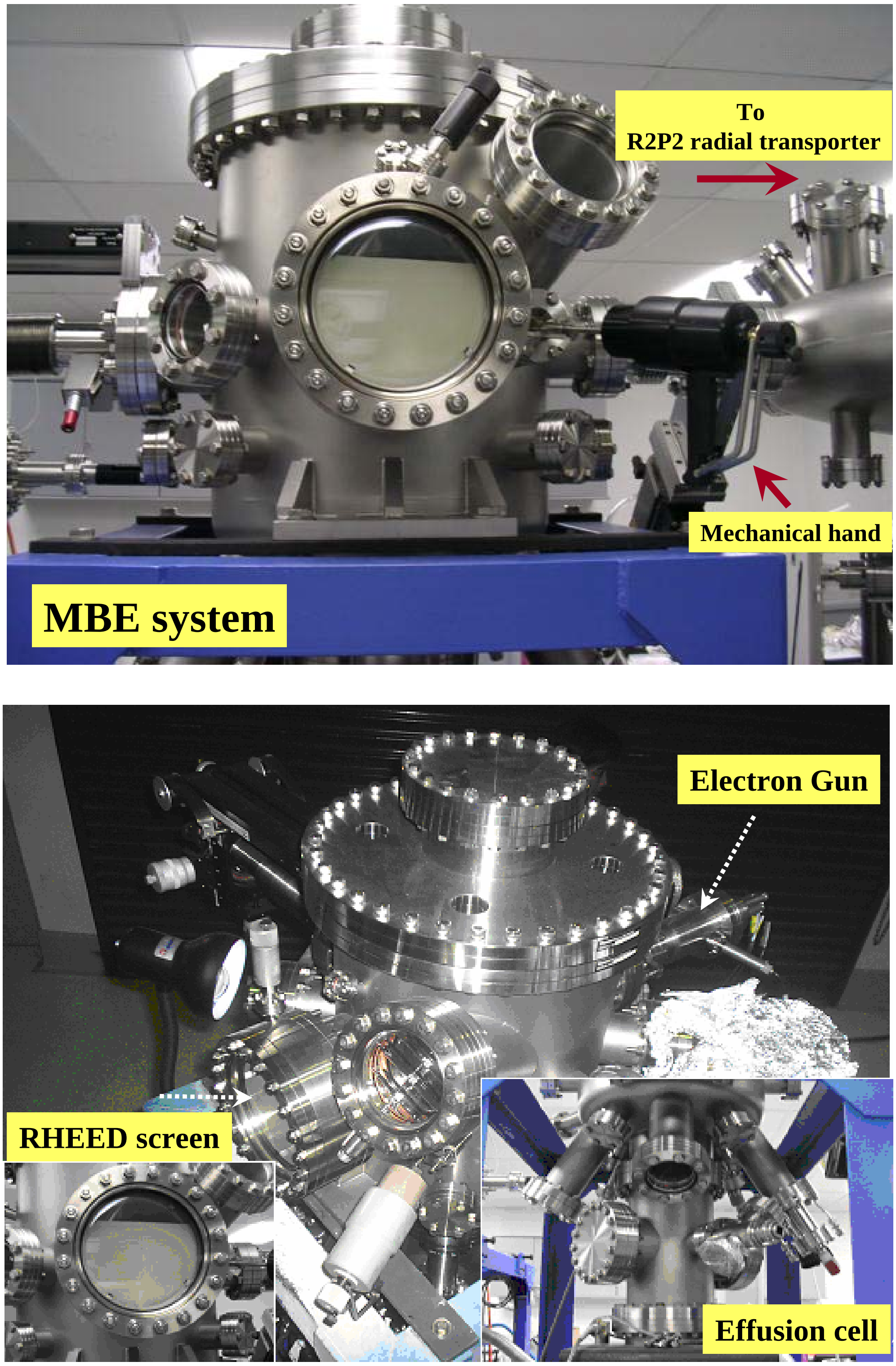

(a)

(b)

Figure 3.9 Photoes (a) and (b) of the MBE/MBD system at the BL4 beamline.

The sample holder mechanism of the MBE system has to be the same as the one used in the original experimental system since the same sample holder has to be moved between the MBE/MBD system and the original photoemission system. The sample/substrate is thus heat by electron beam heating. The maximum temperature for such a heating facility is about 1200°C. The dimension of the sample is limited to 8 × 10 mm^2.

Currently, RHEED (reflection high-energy electron diffraction) is used for real-time monitoring during MBE growth. For MBD, a crystal quartz film measurement device is planned for film thickness measurement.

3.2.3 Additional Sample Preparation System

The additional sample preparation system is used for preparing cleaned and well-defined solid surfaces. The system is pumped by a 500 l/s ion pump and a titanium sublimation pump to produce UHV. Surface cleaning may be performed by ion sputtering and/or electron-beam bombardment heating. The system is also equipped with AES and LEED systems. The AES system employing a cylindrical mirror analyzer is used for checking surface impurities. LEED is used to verify a well-define surface. After cleaning procedures, the clean and well-defined samples may be transferred to the photoemission system for the investigation of the electronic structure or to the MBE system for growing an ultra-thin metal film. The grown layer may then be characterized by XPS or be studied by photoemission spectroscopy. The photos of the additional preparation system are shown in Figure 3.10.

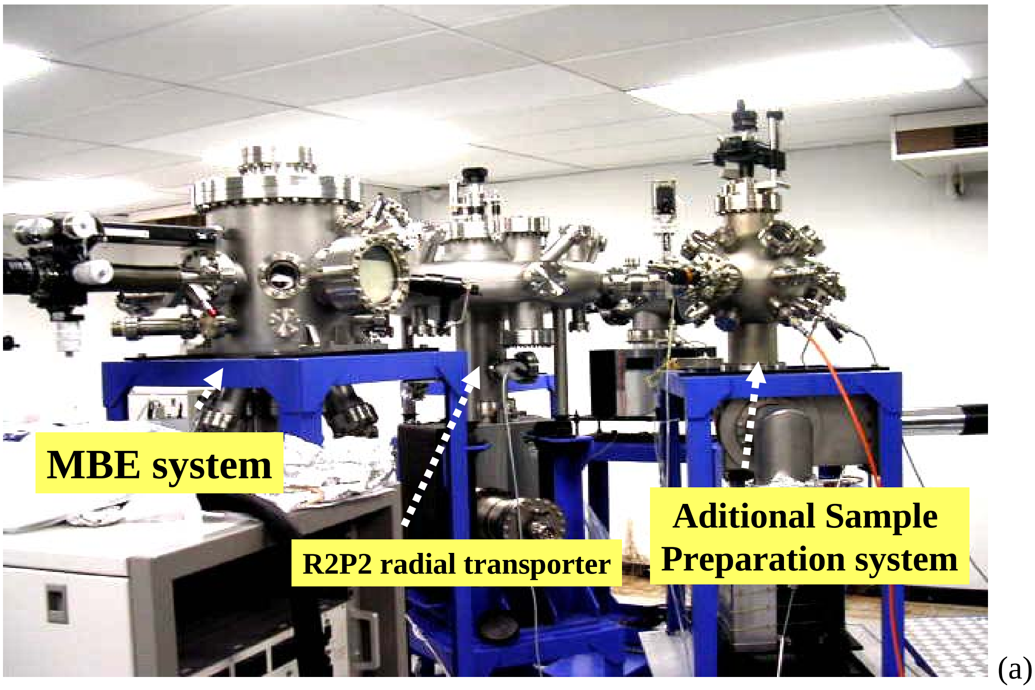

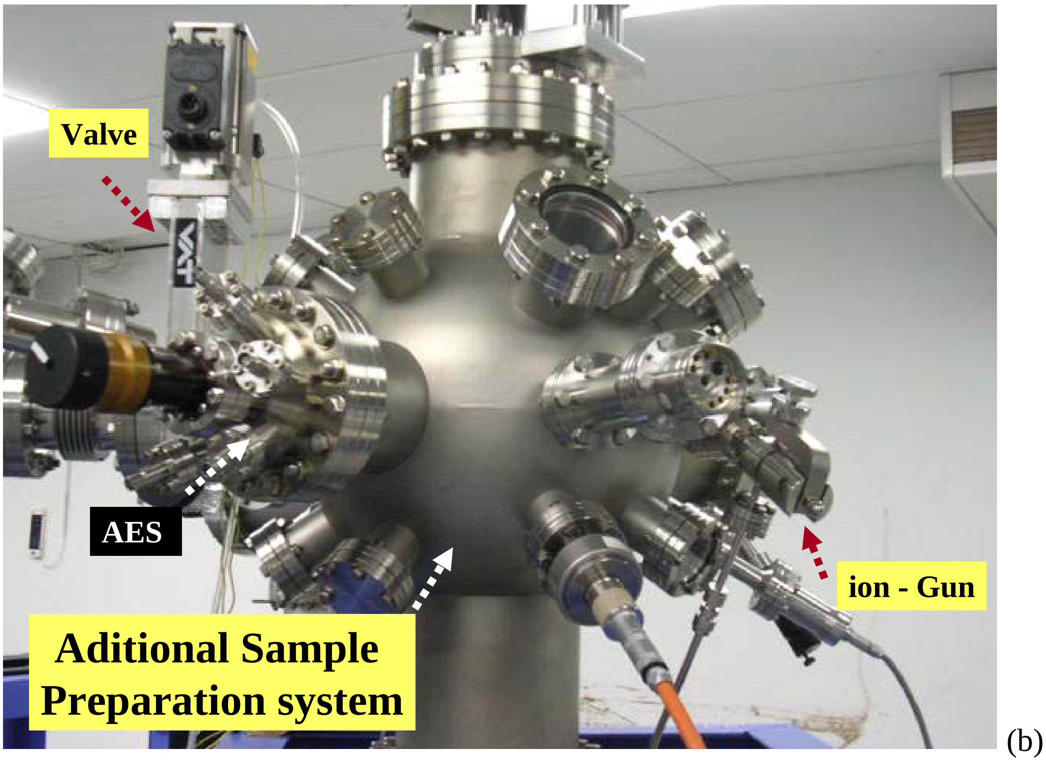

Figure 3.10 The photo of extended systems for the BL4 experimental station (a) and the additional preparation system for solid surface treatment (b).

CHAPTER IV

RESULTS AND DISCUSSIONS

In this thesis work, the BL4 beamline has been optimized. The performance of the BL4 beamline, which are characterized by the resolving power and rejection of high-order light, are reported and discussed. The commissioning results of the upgraded experimental station of the BL4 beamline are also reported and discussed in this chapter.

4.1 Performance of the BL4 Beamline

4.1.1 Resolving Power of Monochromator

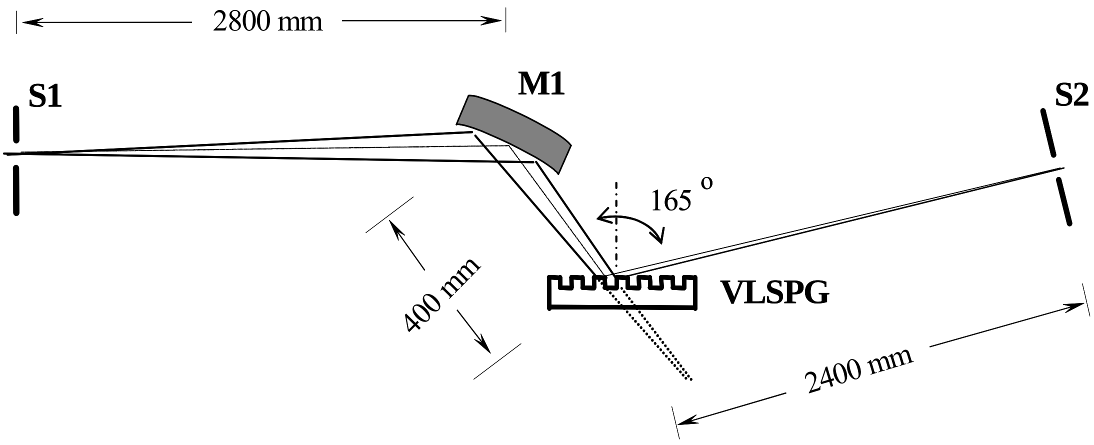

Figure 4.1 The optical layout of the VLSPG monochromator of the BL4 beamline at SPL.

The ability for a synchrotron beamline to deliver light with a very narrow bandpass is determined by the performance of the monochromator used in the beamline. The BL4 beamline at the Siam Photon Laboratory employs a VLSPG monochromator, which is illustrated in Figure 4.1. It should be noted that the grating is placed in such a way that the high-groove density end is at the downstream of the beamline.

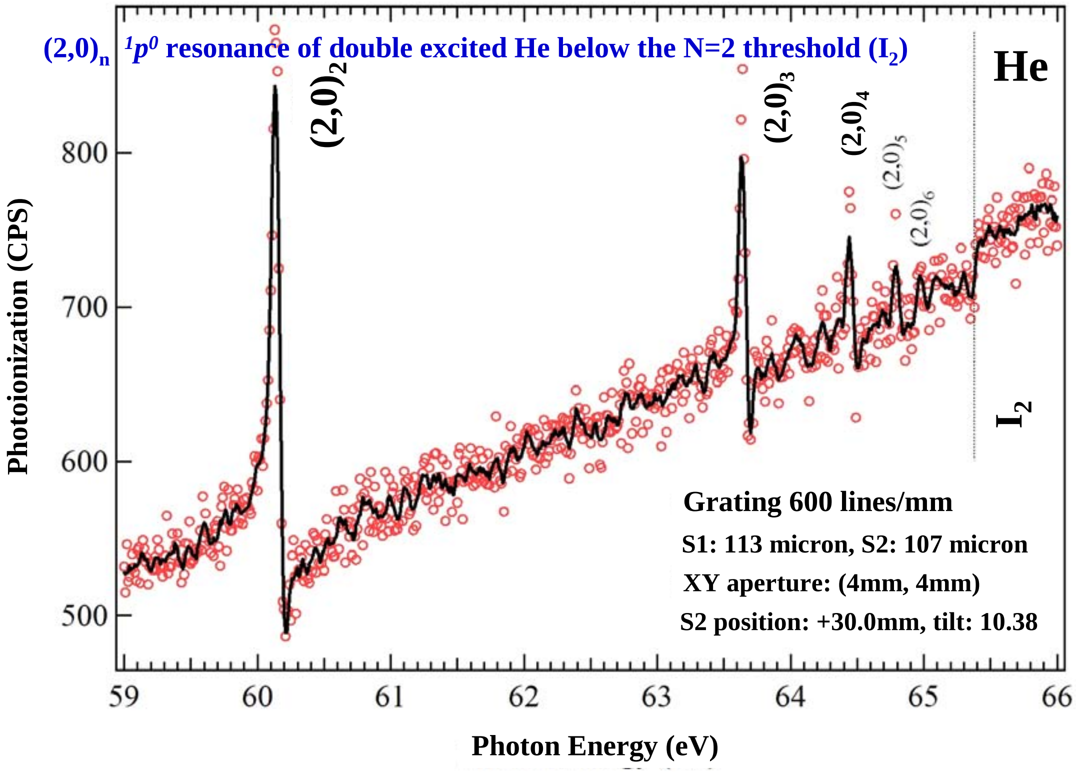

Figure 4.2 Photoionization spectrum measured on ${}^{1}p^{0}$ resonance excited He below the N=2 threshold (I_2).

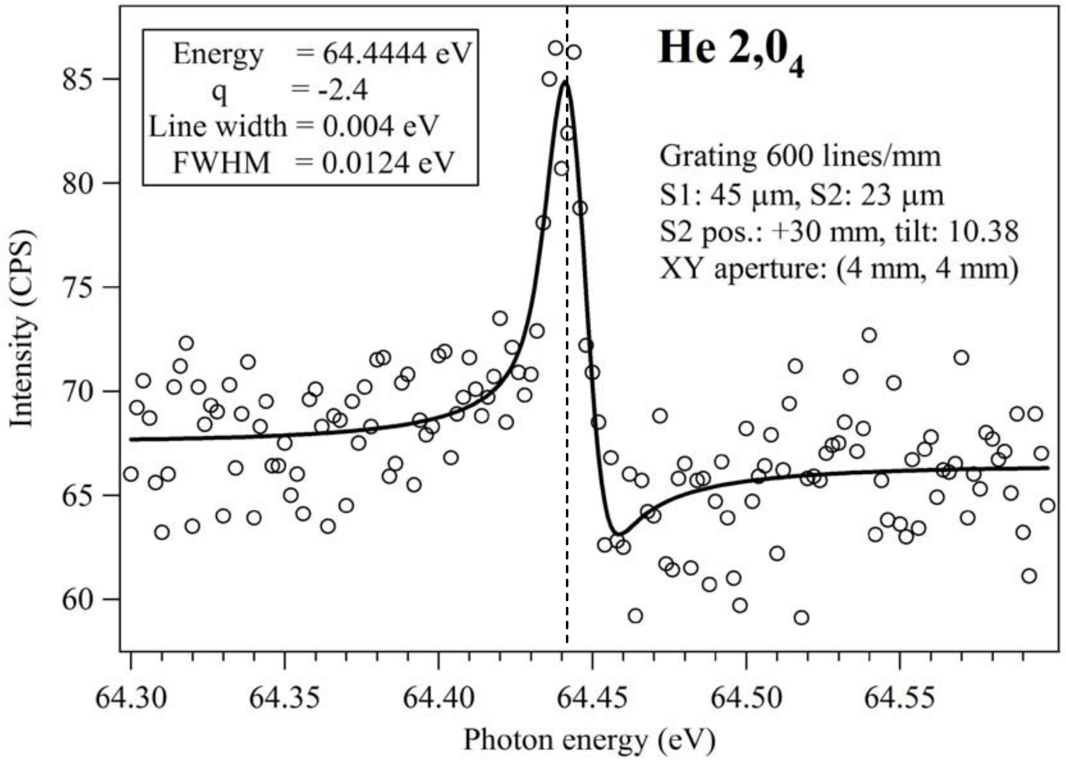

Figure 4.3 Photoionization spectrum measured on $2,0_4$ resonance of doubly excited helium.

Figure 4.3 shows the photoionization spectrum taken from the $2,0_4$ resonance of doubly excited helium. The spectrum is total electron yield as function of exciting photon energy. The spectrum was obtained with the experimental set-up described in Chapter II. Monochromatized light excites He atoms in the ionization chamber, which is in fact the analysis chamber of the ARPES system. The electrons emitted from the gas atoms are counts by a channeltron. In the Figure, open circles represent the experimental results, solid line the fitting result using Fano profile convoluted with a Gaussian. Resonance energy, Fano parameter (q), line width and Gaussian width (FWHM) used in fitting are described in the box. FWHM determines the resolution (or resolving power) of the monochromator. It is noted that the resolution is expressed as ΔE/E, and the resolving power is expressed as E/ΔE. ΔE is FWHM obtained from the measurement. The smaller FWHM, the better resolution (or higher resolving power) of the monochromator. Ideally, the resolution depends primarily on the quality of optical surfaces, the slit width and the optical layout of optical elements used in the beamline. The surface of the optical elements is never perfect because of technological limits in the manufacturing processes. It has both geometrical error (radius of curvatures) and micro error (slope error and roughness). After the beamline has already been built, the alignment of optical elements must be adjusted close to perfect as possible. Thus, the resolution of the beamline is controlled by the slit width.

The spectrum in Figure 4.3 was taken when the exit slit is positioned at the optimized position, which is 30 mm downstream of the designed position. The designed position is 2406.6 mm from the grating. In theory, the best resolution or the high resolving power should be obtained when the exit slit is at the designed position. The deviation of position from the designed position is caused by the imperfections of the manufacturing of the optical surface and the misalignments of the upstream optical elements. The slit width of the entrance slit (S1) and the exit slit (S2) are 45 micron and 23 micron, respectively. For these widths, the slit-limited resolving power calculated from the analytical expressions is 5000 at the $2,0_4$ resonant excitation energy and with groove density of grating (600 lines/mm). The measured spectrum in Figure 4.2 represented by open circles was fitted with Fano profile convoluted with a Gaussian. Fano parameter $q = -2.4$ and line width $\Gamma = 0.004$ eV are used from the previously reported values (Domke, Schulz, Remmers, and Kaindl, 1996). It was found that the FWHM is 0.0124 eV. This corresponds to the resolving of about 5000, which is in good agreement with the calculation. It should be noted that the resolving power of 5000 is the ultimate goal for the design of this beamline. However, the signal-to-noise ratio at the resolving power of 5000 is still poor. This is due to low photon flux limited by the large diameter electron beam in the storage ring and the small slit width. Maximum practical resolving power is obtained when the width of the entrance and exit slit is about 100 micron, corresponding to the resolving power of about 1000.

The spectrum in Figure 4.3 was actually obtained after the optimization procedures of the monochromator have been performed. In fact, the resolving power depend very much on the orientation of exit slit and the exit-arm length of the grating, the distance from the grating to the exit slit. In the optimization procedures, ionization spectra were taken with the exit-arm length and exit slit orientation allowed to vary.

Figure 4.3 shows the dependence of the FWHM of the Fano line shape on the position of the exit-slit relative to the designed position. The data were deduced from a series of photoionization measurements around the $2,0_4$ resonant excitation energy with different positions of the exit slit on the optical axis. The open circles represent FWHM of the Fano line shape obtained from fitting of the measured results of $2,0_4$ resonance of doubly excited helium. From the fitting, the optimum position of the exit slit is 30 mm downstream of the designed position. This indicates that the photon beam is focused 30 mm behind the exit slit. Thus, the exit arm length of the grating is 2436 mm.

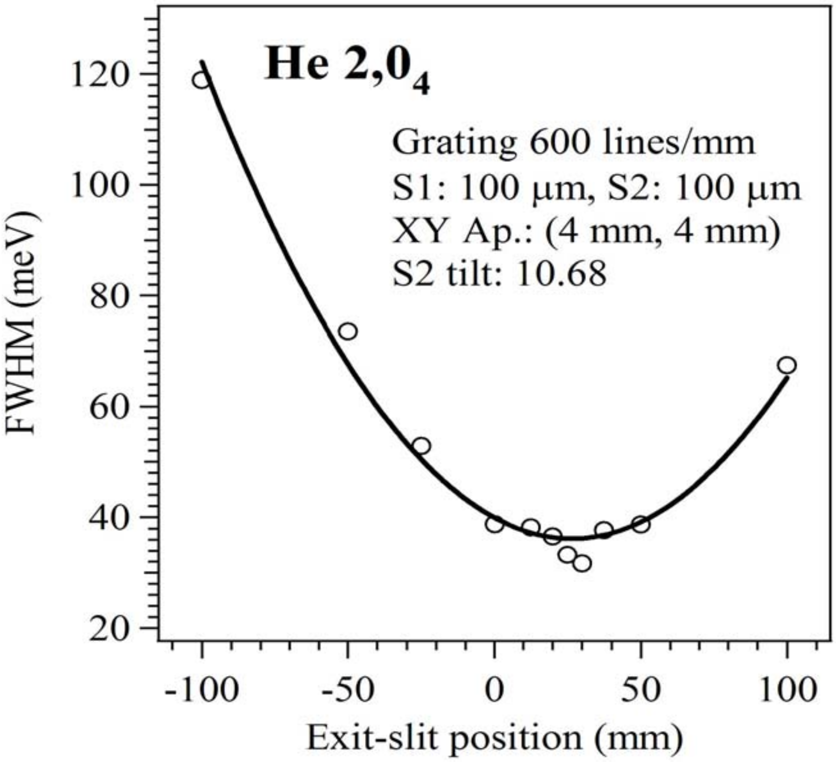

Figure 4.4 FWHM of the Fano line shape obtained from fitting of photoionization spectrum as a function of the position of the exit slit relative to the designed position.

Figure 4.4 shows the dependence of the FWHM of the Fano line shape on the orientation of the exit-slit. The open circles represent FWHM of the Fano line shape obtained from fitting of the measured results of $2,0_4$ resonance of doubly excited helium. Ideally, synchrotron line beam should vertically be focused on the exit slit with a rectangle shape. Optical aberrations and mis-alignment of the upstream optical elements yield distorted shaped of focused photon beam on the exit slit. The exit slit allows rectangular beam passing through. It was also designed to be able to be tilted to get maximum resolving power. It was found from fitting, shown as a solid line in the figure, that the optimized tilt of the exit slit is about 10.68 .

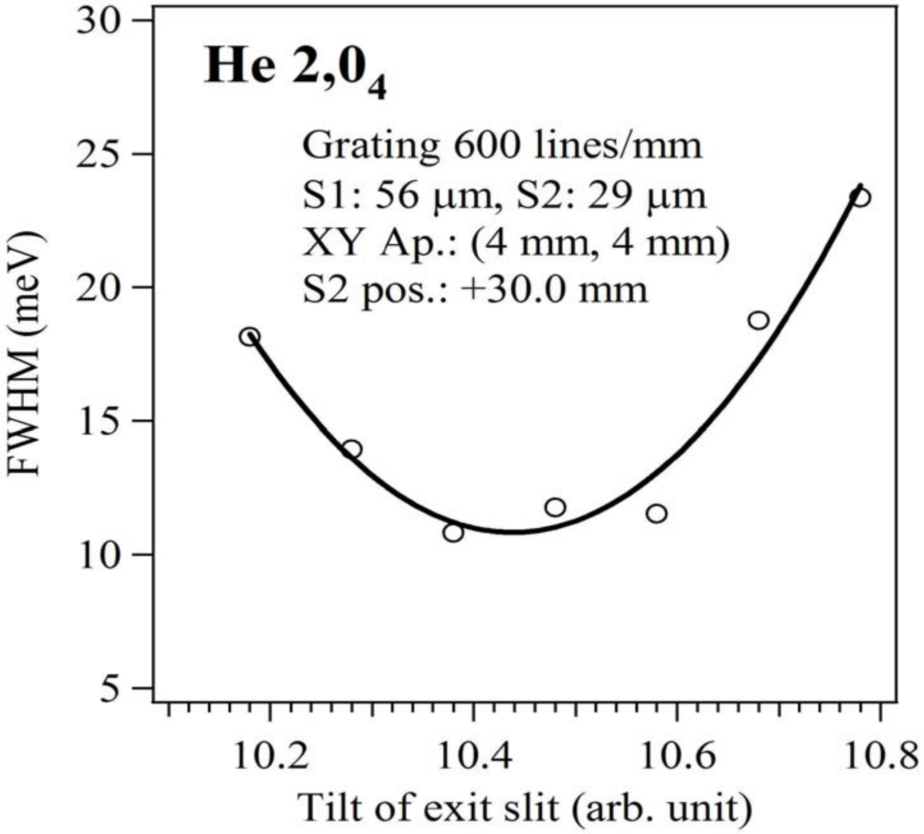

Figure 4.5 FWHM of the Fano line shape obtained from fitting of photoionization spectrum as a function of the orientation of the exit slit.

The measured resolving powers using different slit widths, listed in table 4.1, have also been measured. The measured resolving powers were also in good agreement with those calculated from analytical expression, as shown in Figure 4.6. It is interesting to note that the vertical aperture located in font of M1 was fully open for all the measurement. This indicated that the aberrations from the grating is not significant as the exposed area on the grating is big, which is about 135 × 22 mm^2.

Table 4.1 Resolving Powers when using various slit widths.

Resolving Power (E/ΔE)	S1 (micron)	S2 (micron)
5000	45	23
4000	56	29
3000	75	38
2000	113	107
1000	226	116
500	452	232

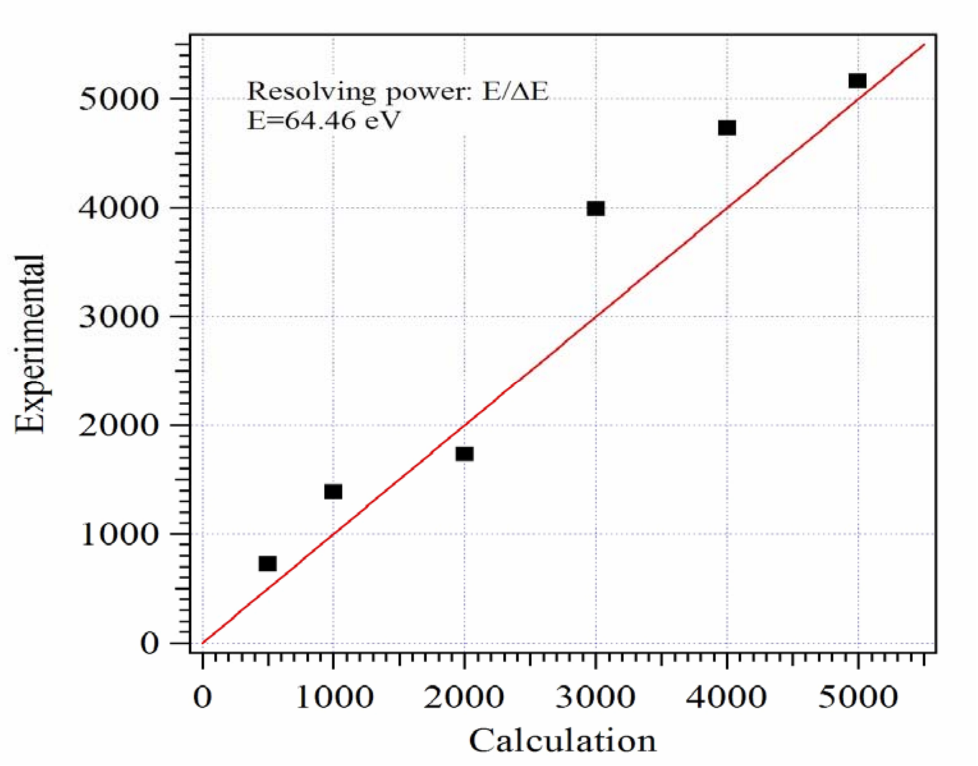

Figure 4.6 Comparision the Resolving Power between Experimental at NSRC and calculation result when using various slit widths, as show in Table 4.1.

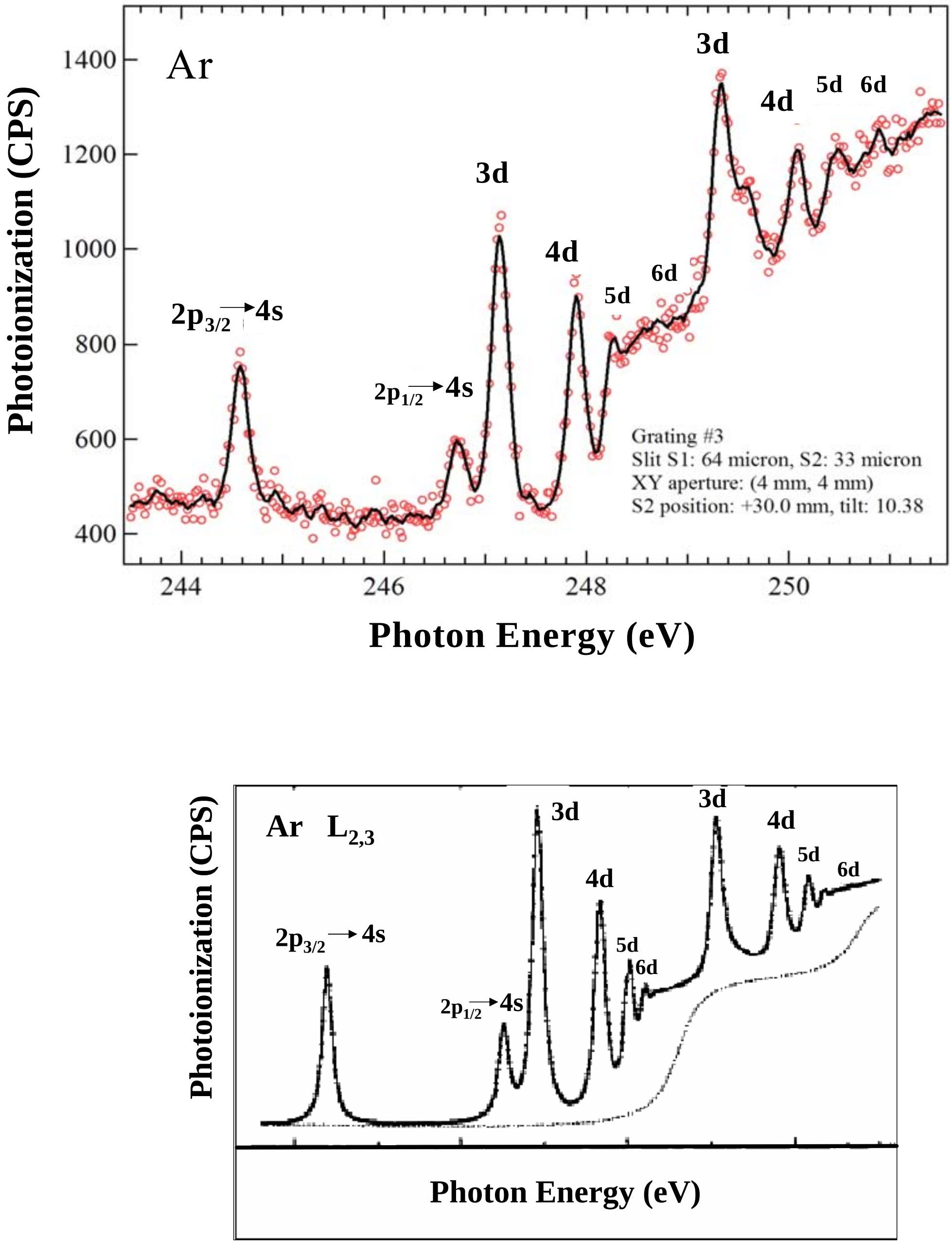

Figure 4.7 Photoionization spectrum of gas-phase Ar taken at BL4 Beamline monochromator at Siam Photon Laboratory (a), comparing to that taken at BESSY beamline using a SX700/II monochromator (b).

4.1.2 High-Order Light

4.1.2.1 Grating with N_0=300 lines/mm

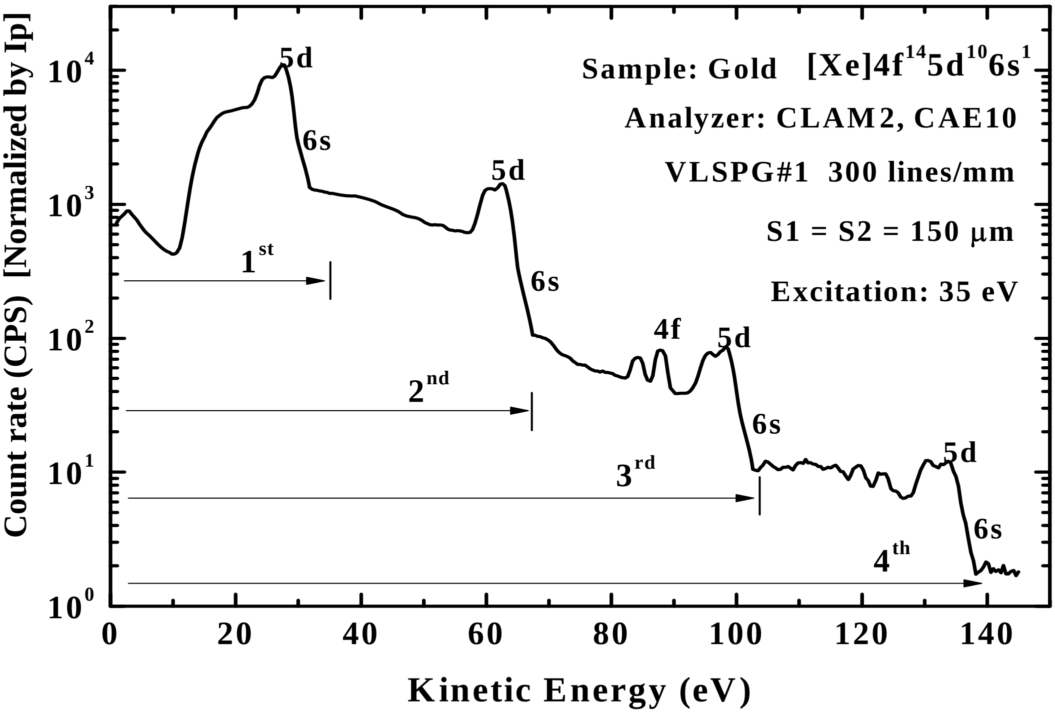

Figure 4.8 Photoelectron spectrum of gold excited by monochromatized light from the monochromator of the BL4 beamline using VLSPG # 1 as the dispersive element. The photon energy of the first order light is 35 eV.

Figure 4.8 shows photoemission spectra of gold taken by the CLAM2 energy analyzer with excitation monochromatized light from the BL4 beamline. The grating VLSPG # 1 with the N_0=300 lines/mm grating was used as a dispersive element in the monochromator. The photon energy of the first order light is 35 eV, and thus the second, third and forth-order lights are 70 eV, 105 eV, and 140 eV, respectively. From the results shown in Figure 4.5, high-order lights from the monochromator is detectable up to the forth order. Ideally, only the first-order light is needed. High-order lights are not wanted. The contamination of the high order lights result in a complicated spectrum as shown in Figure 4.5. Thus, it should be kept in mind that high-order light may excite core electrons which, in turn, results in the features in a spectrum in the region below the photon energy of the first-order excitation light. Photoionization cross section of Au 5d at photon energies of 35 eV, 70 eV, 105 eV, and 140 eV are approximately 4, 1, 0.03, and 0.01 Mb/atom (Yeh and Lindau, 1985). Considering the photoionization cross section, the ratio of the 2nd, 3rd, and 4th order to 1st order light at this diffraction angle are 25, 0.8, and 0.3 percent, respectively.

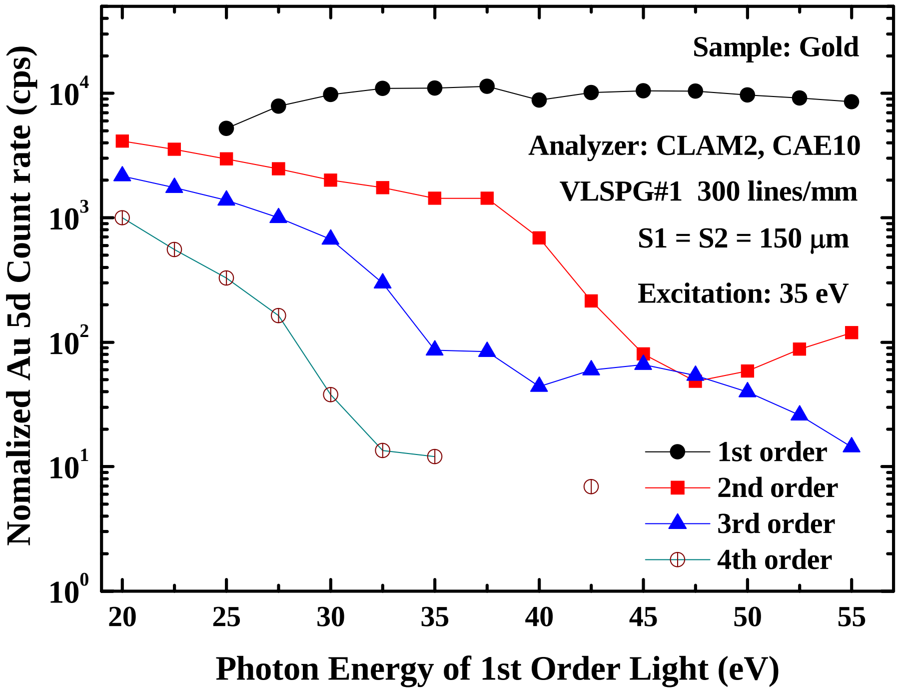

Figure 4.9 Peak height of Au 5d deduced from the energy dispersive curves as a function of the photon energy of the 1st order excitation light for a whole photon energy covering by VLSPG # 1.

Figure 4.9 shows the Peak height of Au 5d deduced from the energy dispersive curves as a function of the photon energy of the 1st order excitation light for a whole photon energy covering by VLSPG # 1. The data were normalized with the intensity of monochromatic excitation light. The amount of high-order light decreases with photon energy. Below 40 eV, the contamination of the 2nd order light is rather high, between ~ 20 and 40 percent. Below 25 eV, the intensity of the 3rd order light is still significant, between ~10 and 20 percent. To obtain monochromatized with the 4th order light less than 1 percent, one has to use 1st order light with photon energy more than 25 eV. As a result, when photoemission measurements are performed with photon energy less than 40 eV, the first few high-order lights influent significantly the measured photoemission spectra. It is nearly impossible to obtain meaningful photoemission spectra with excitation light with photon energy below 30 eV for this monochromator.

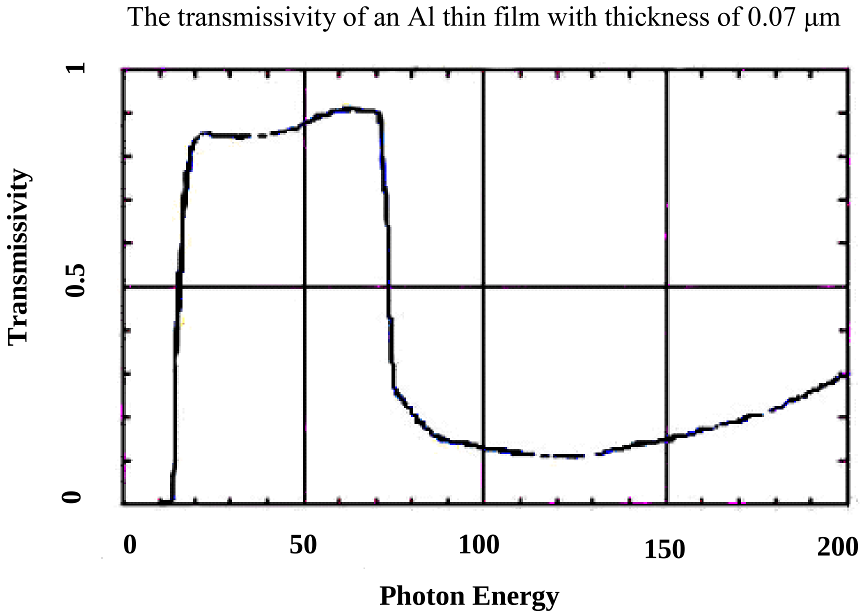

Figure 4.10 The transmissivity of an Al thin film with thickness of 0.07 μm as a function of photon energy.

Suppression of high-order lights may be achieved by using filters, which may be very thin foils or mirror coated with proper materials that absorb photons in the energy range of the unwanted high-order lights. Figure 4.10 shows the transmission of light through a 0.07-μm-thick Al foil as a function of photon energy in eV. The energy bandpass of this foil is from 15 eV to 75 eV. Thus, it has been chosen to be experimented as a filter to suppress high-order light with photon energy greater than about 75 eV. The foil is installed on a linear drive allowing the filter to retractable from he optical axis. The Al foil is located between the post focusing mirror M2 and the sample.

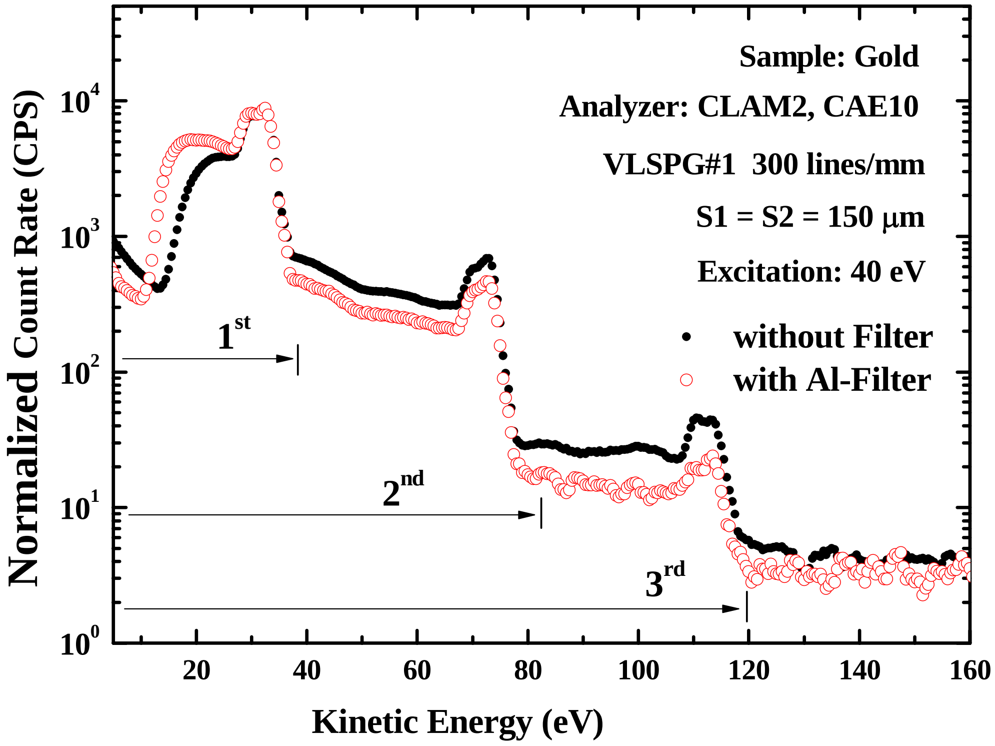

Figure 4.11 EDC of gold taken by the CLAM2 analyzer at the BL4 beamline with and without an Al film as a filter.

Figure 4.11 shows EDC of gold taken by the CLAM2 energy analyzer at the BL4 beamline. The photon energy of the 1st order of the excitation light is 40 eV. The spectra are normalized at Au 5d peak excited by 1st order light. It is clearly seen that the photoelectron signals excited by high-order lights are lower when the Al filter is used in the beamline, indicating that high-order lights are suppressed. It should be noted that in the region below about 25 eV kinetic energy of photoelectron, the signals of the photoelectrons are higher when the Al filter is used. This is due to the limit of the performance of the CLAM2 energy analyzer since this low energy region the performance is greatly influenced by the total number of photoelectrons, which are mostly secondary electrons. Without the filter, the number of secondary electron is much higher than that when the filter is used. In fact, the spectral shape is improved when the Al foil is used since the overlapping of secondary electron is less.

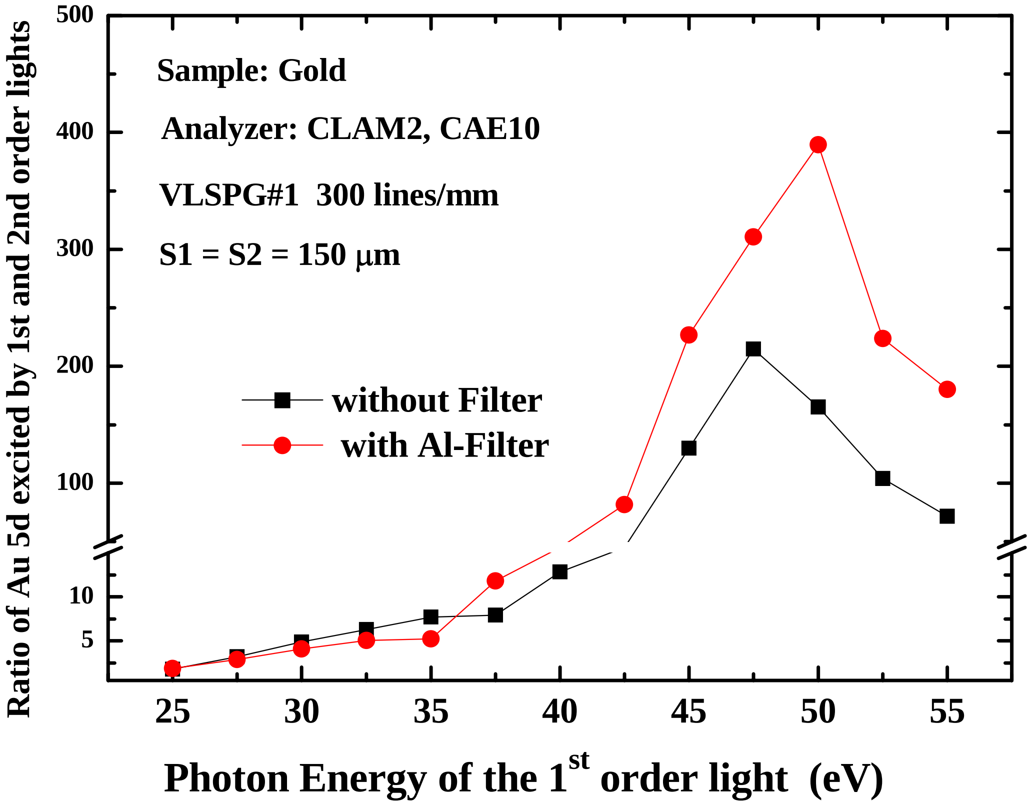

Figure 4.12 Ratio of the Au 5d peak excited the 1st order light to the 2nd order light when using the BL4 beamline with and without an Al foil as a filter.

.

The 2nd order light of the BL4 beamline is suppressed when a 0.07-µm-thick foil is used. This is indicated by the ratio of the Au 5d peak excited by the 1st order light to the 2nd order light, as shown in Figure 4.12. At photon energy below ~35 eV, there is no advantage of using the Al foil since the photon energy of its 2nd-order still within the energy band-pass of the foil, as shown in transmission spectrum in Figure 4.10. The measurement results in Figure 4.12 shows that the ratio of Au 5d peak excited by the 1st order light to the 2nd order light filter when using the Al filter becomes larger than that when the Al is not used at photon energy of ~ 37 eV. This indicates that the Al foil becomes an effective filter for high-order light suppression when photon energy of the wanted 1st order light greater than ~37 eV, and thus the photon energy of the 2nd order light is ~74 eV. This is very well in agreement with the calculated transmission of the Al foil, shown in Figure 4.7 where the high-energy end of the band-pass is ~75 eV. The suppression of 2nd, 3rd, and 4th order light when the Al foil is used as the filter in the beamline can be shown Figure 4.13, 4.14, and 4.15, respectively. It is clearly seen that the filter becomes effective at photon energy greater than ~35 eV, 25 eV, and ~20 eV for the 2nd, 3rd, and 4th order lights, respectively.

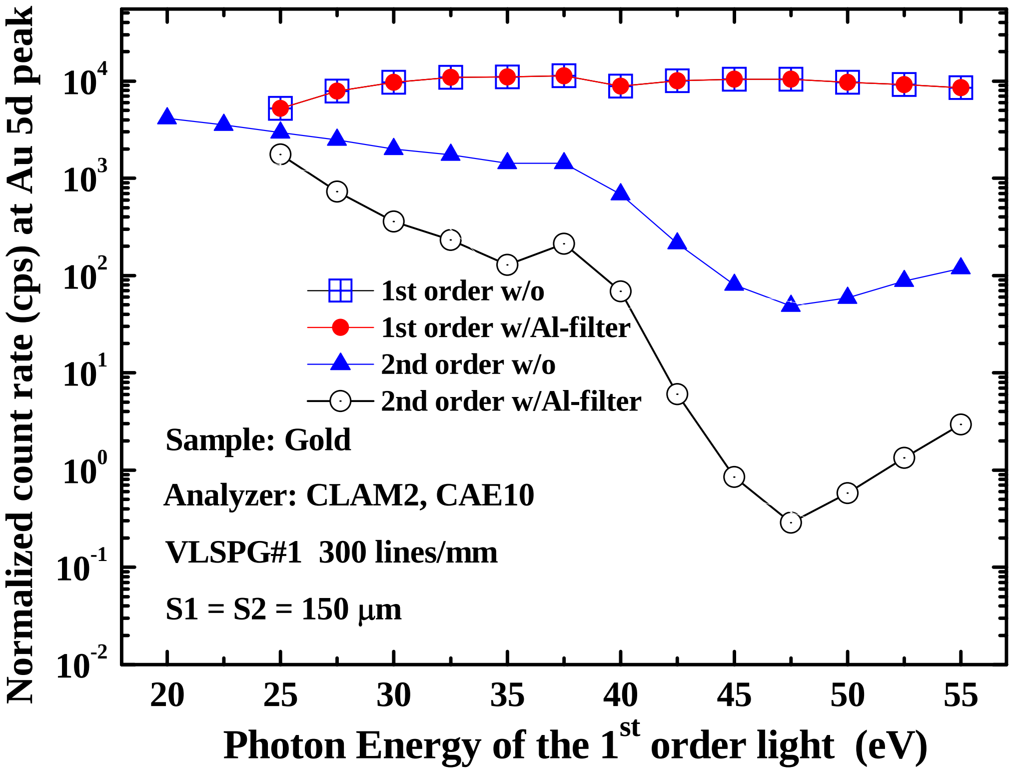

Figure 4.13 Normalized signal of Au 5d peak excited by 1st and 2nd order light with and without an Al filter.

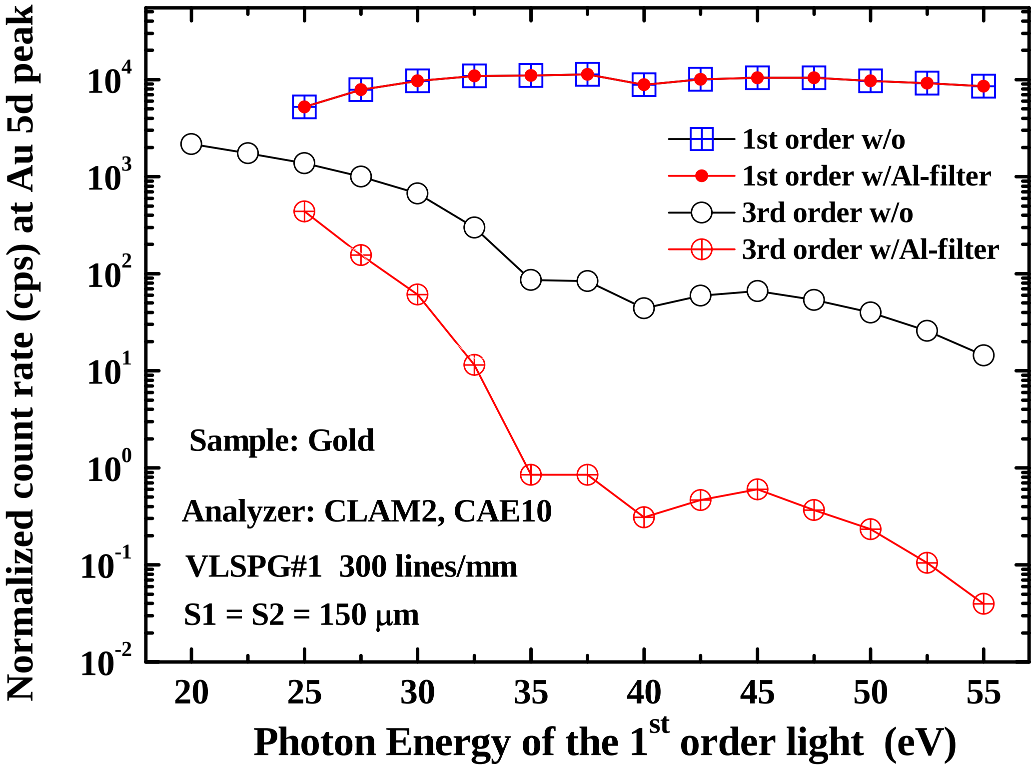

Figure 4.14 Normalized signal of Au 5d peak excited by 1st and 3rd order light with and without an Al filter.

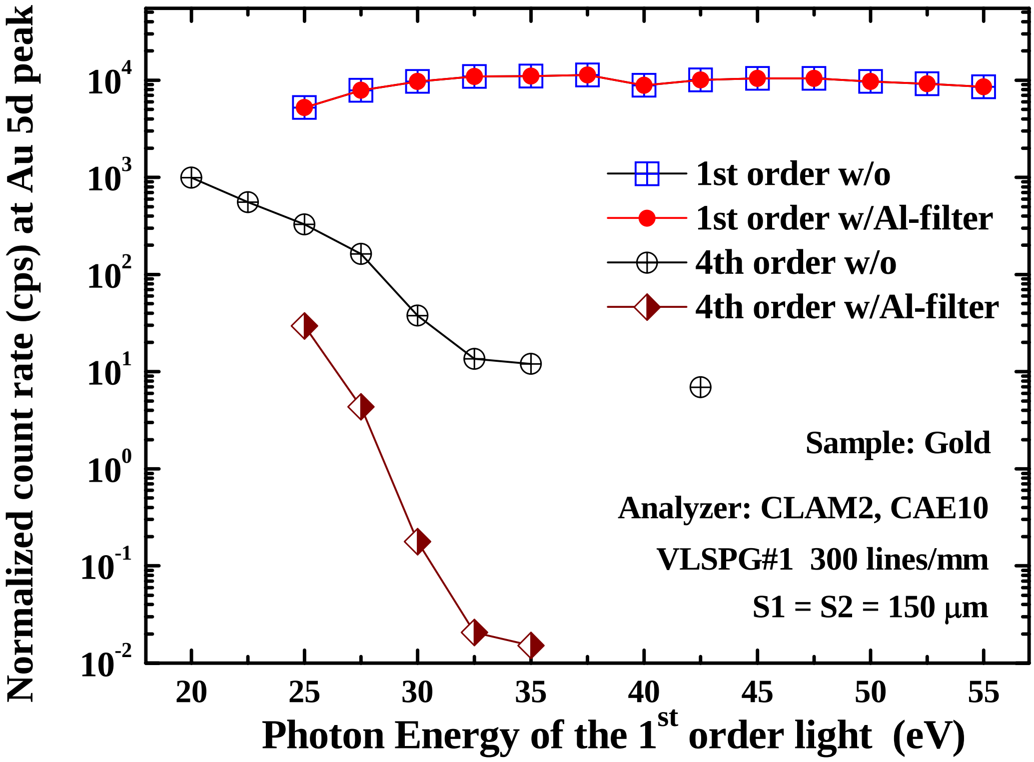

Figure 4.15 Normalized signal of Au 5d peak excited by 1st and 4th order light with and without an Al filter.

4.1.2.2 Grating with N_0=600 lines/mm

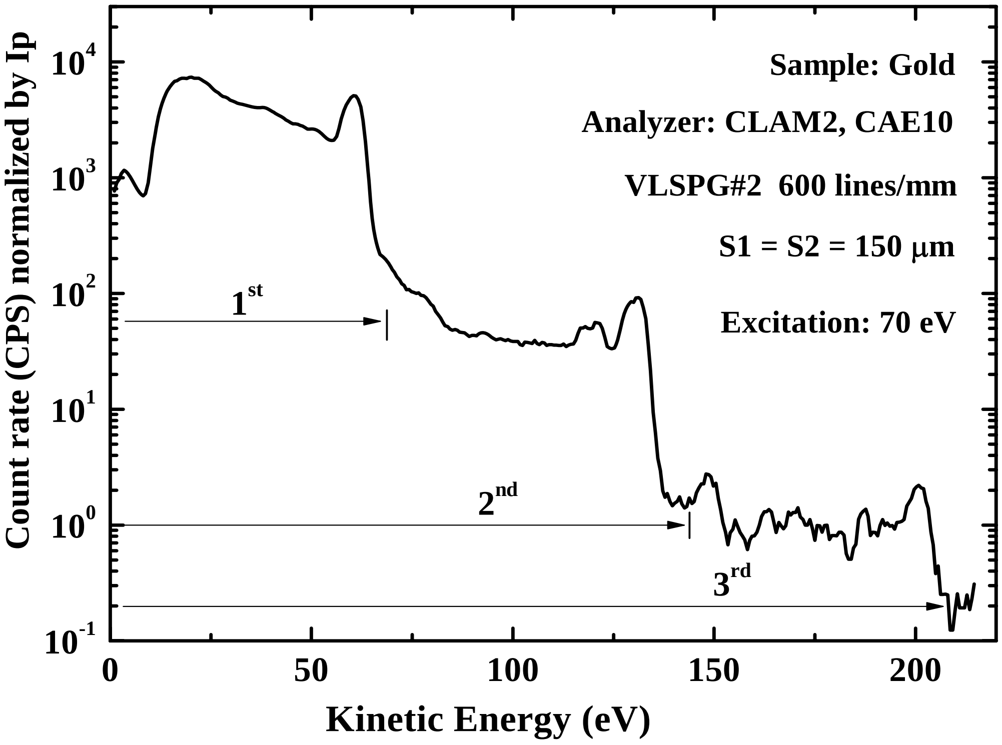

Figure 4.16 Photoelectron spectrum of gold excited by monochromatized light from the monochromator of the BL4 beamline using VLSPG # 2 as the dispersive element. The photon energy of the first order light is 70 eV.

Figure 4.16 shows photoelectron spectrum of gold excited with monochromatized with higher photon energies. The grating with N_0=300 lines/mm, VLSPG # 2, is used to give light with photon energies of 70eV (1st order), 140 eV (2nd order), 210 eV (3rd order) and so forth. The contamination of the second order light is a few percent. This is not significant comparing to the case when low-energy grating VLSPG#1 is used. The 3rd order light contamination is negligible.

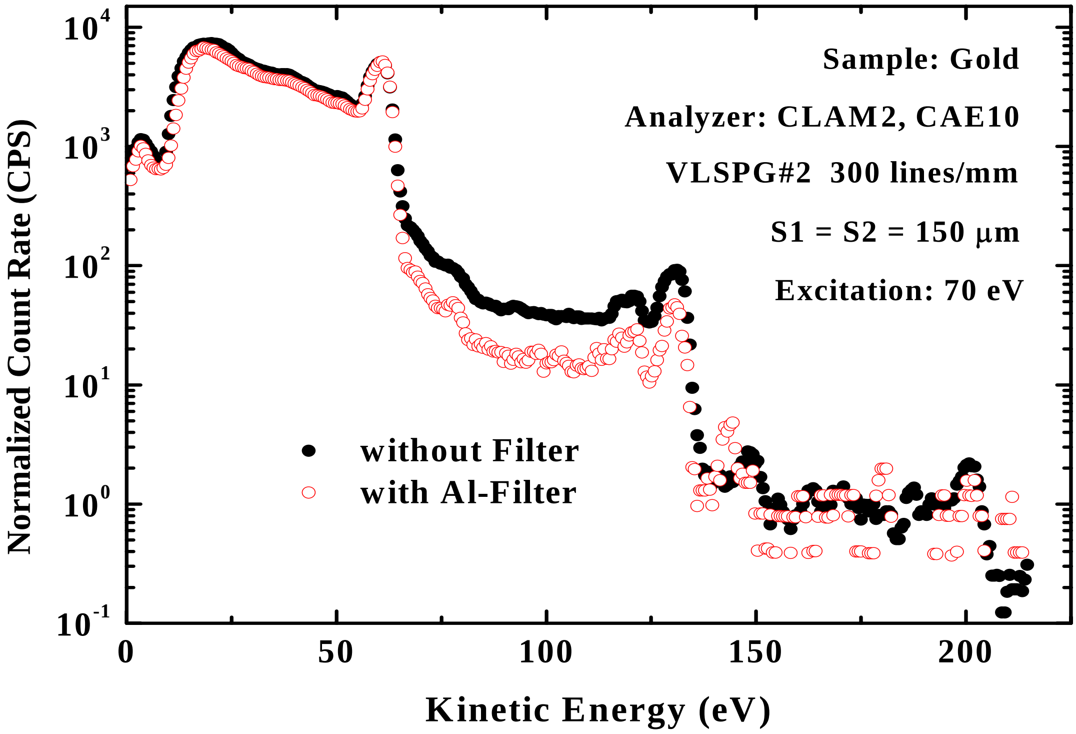

Figure 4.17 EDC of gold taken by the CLAM2 analyzer at the BL4 beamline with and without an Al film as a filter .

Figure 4.17 shows EDC of gold excited by monochromatized light with the photon energy of the 1st order light of 70 eV with and with out using the Al foil as the filter. It is clearly seen that the suppression of high order lights is appreciated even though the contamination of the high-order lights is not significant from the begging. For a whole photon energy range covering by VLSPG # 2, the suppression of hig-order light may be deduced from the ratio of the photoelectron signals excited by 1st order light to the 2nd order light, shown in Figure 4.18

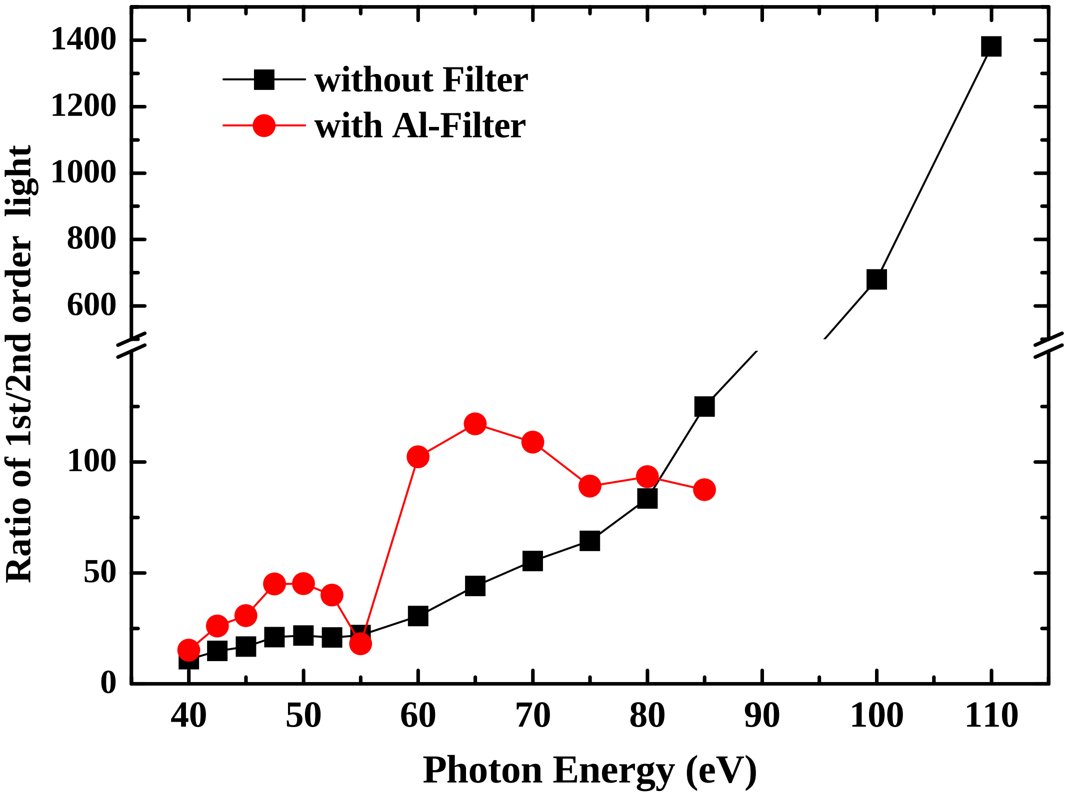

Figure 4.18 Ratio of the Au 5d peak excited the 1st order light to the 2nd order light when using the BL4 beamline with and without an Al foil as a filter.

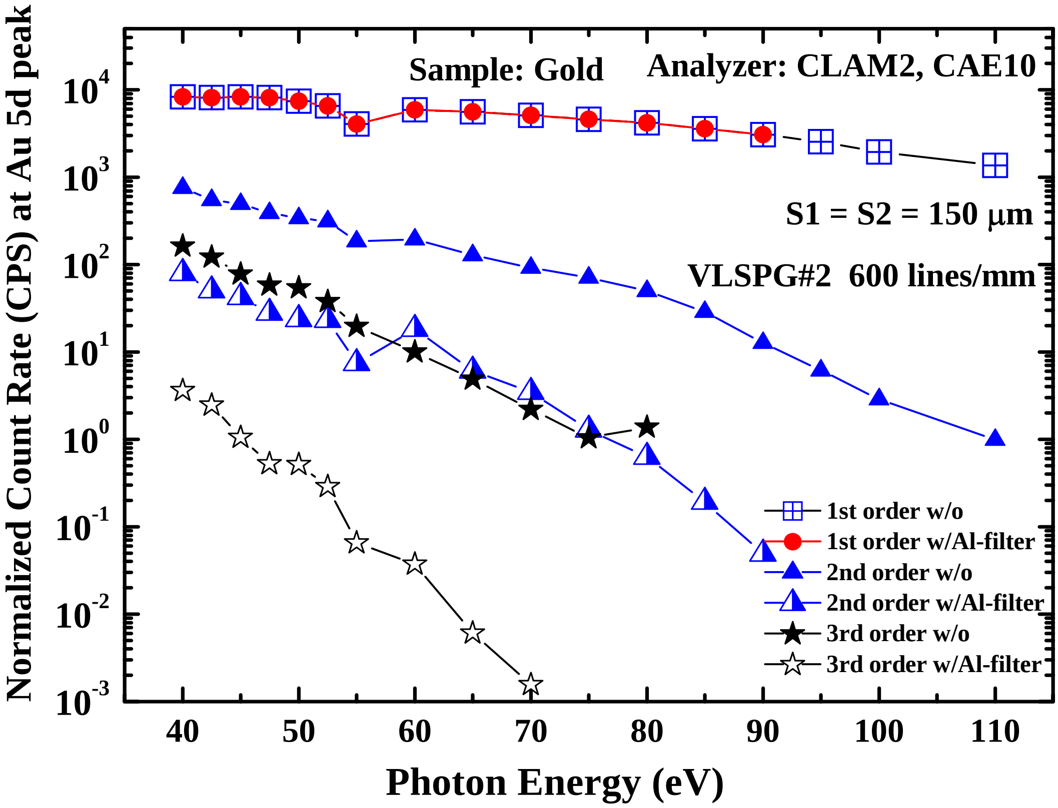

Figure 4.19 Count rate of the Au 5d peak excited by 1st, 2nd, and 3rd order lights when using the BL4 beamline with and without an Al foil as a filter.

4.1.2.3 Grating with N_0=1200 lines/mm

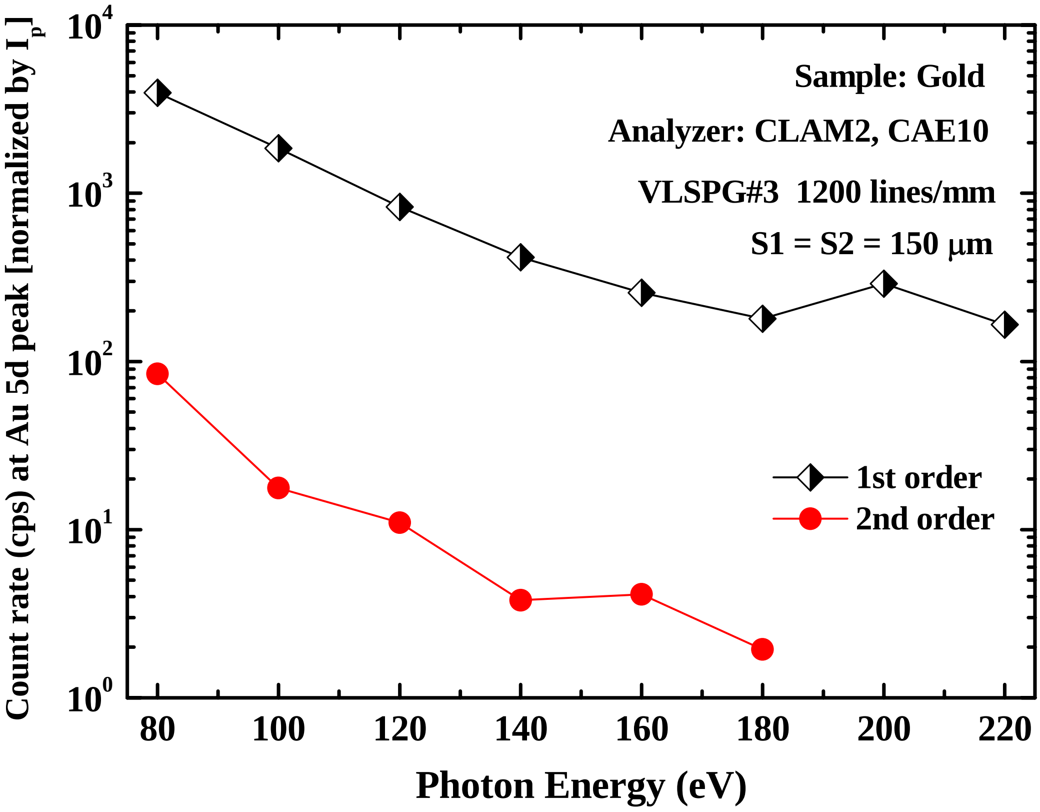

Figure 4.20 Peak height of Au 5d deduced from the energy dispersive curves as a function of the photon energy of the 1st order excitation light for a whole photon energy covering by VLSPG # 3.

High-order light contamination may be negligible when using the high-energy grating VLSPG # 3. This is confirmed from photoemission measurement shown in Figure 4.20. The 2nd order is less than nearly the whole energy range.

4.2 Commissioning Results of New Experimental Station

4.2.1 Sample Transfer

There are two possible ways for loading sample into the new experimental station of the BL4 beamline without breaking UHV condition of the experimental station. One way is to use a FEAL (fast-entry air lock), which is connected to one of the radial port of the R2P2 sample with a gate valve for vacuum isolation. FEAL was originally used for load and unload sample for the original photoemission system of the BL4 beamline. After introducing the sample into the R2P2 transfer system, the sample may be transferred further to the MBD/MBE chamber or to the ARPES system. The other way for introducing sample in to the experimental station is use a load-lock system of the XPS system. However, this must be done when the XPS system is not used. In fact, this load-lock system is designed for routine XPS operation.

The sample transfer system has successfully been tested, and is now in operation. The sample can also transferred between the main UHV chambers. For example, a sample with a deposited layer from the MBE/MBD system can be transferred to the XPS or ARPES system for analysis.

4.2.2 Vacuum

All vacuum vessels of the new experimental station have been leak-tested using a RGA with helium gas. No leak was found at the welding joints. Standard procedures to obtain UHV in XPS, MBE/MBD and sample preparation systems and in the linear and rotary sample transporters were carried out. Each UHV chamber was baked out at a time due to the limit of a turbomolecular pumping unit, except for the

XPS analysis chamber that can be baked out any time as it has its own turbomolecular pumping unit for independent load-lock system. Typical baking temperature is 150°C. The baking time is normally at least 24 hours, depending on the history of the chamber. In some circumstances, baking temperature was raised to 175°C for more effective baking and shorter baking time. In the beginning of this work, baking was done by using heating elements wrapped around the chamber. The chamber was wrapped with aluminum foils to keep ensure temperature homogeneous. Later, baked-out boxes made of aluminum with heat insulator were used for baking the MBE/MBD and XPS system resulting in much better efficiency of the baking. It is noted that all components of the system that cannot withstand baking temperature are always removed before baking-out procedures.

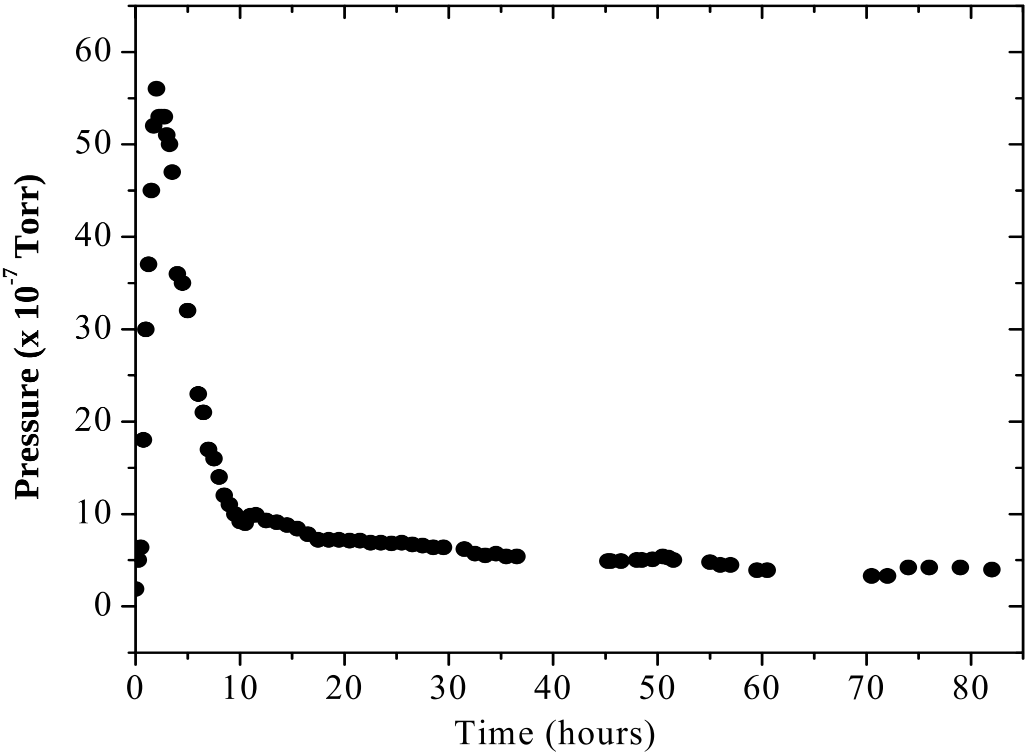

Figure 4.21 Vacuum pressure in the mobile pumping unit during baking the metal MBE/MBD growth.

Figure 4.21 show typical vacuum pressure during baking of the MBE/MBD growth chamber. It should be noted that the pressure shown in Figure 4.21 is from the pressure gauge at the mobile pumping. A 0.8-meter-long flexible tube is used for connecting the mobile pumping unit to the MBE/MBD chamber. The pressure drop along the connecting line is about one order of magnitude. The mobile pumping unit consists of a turbomolecular pump backed by a rotary pump. It is also equipped with an RGA unit for leak test and residual gas analysis. Before baking, the growth chamber must be leak tested if any ports of the chamber have been opened to air. Without leakage, vacuum pressure in the mobile pumping unit usually reaches 10^{-8} torr region in the mobile pumping unit, in the 10^{-7} torr region in the MBE/MBD chamber. In the first three hours of the bakeout, the pressure goes up to the maximum, typically in the 10^{-5} torr region (10^{-7} torr in the MBE/MBD chamber). Then it decreases with time and approaches the minimum pressure of about 5×10^{-8} torr in about 24 hours. In the end of baking-out processes, the filaments of MBE/MBD sources, pressure gauges and analytical tools such as electron gun of RHEED gun were degassed. The base pressure of the MBE/MBD system is about 1×10^{-10} torr.

The vacuum quality of the MBD/MBD system can be assured by using the RGA equipped on the growth chamber. At the based pressure, remaining gases in the chamber are analyzed by the RGA. The typical results from RGA measurements are shown in Figure 4.22.

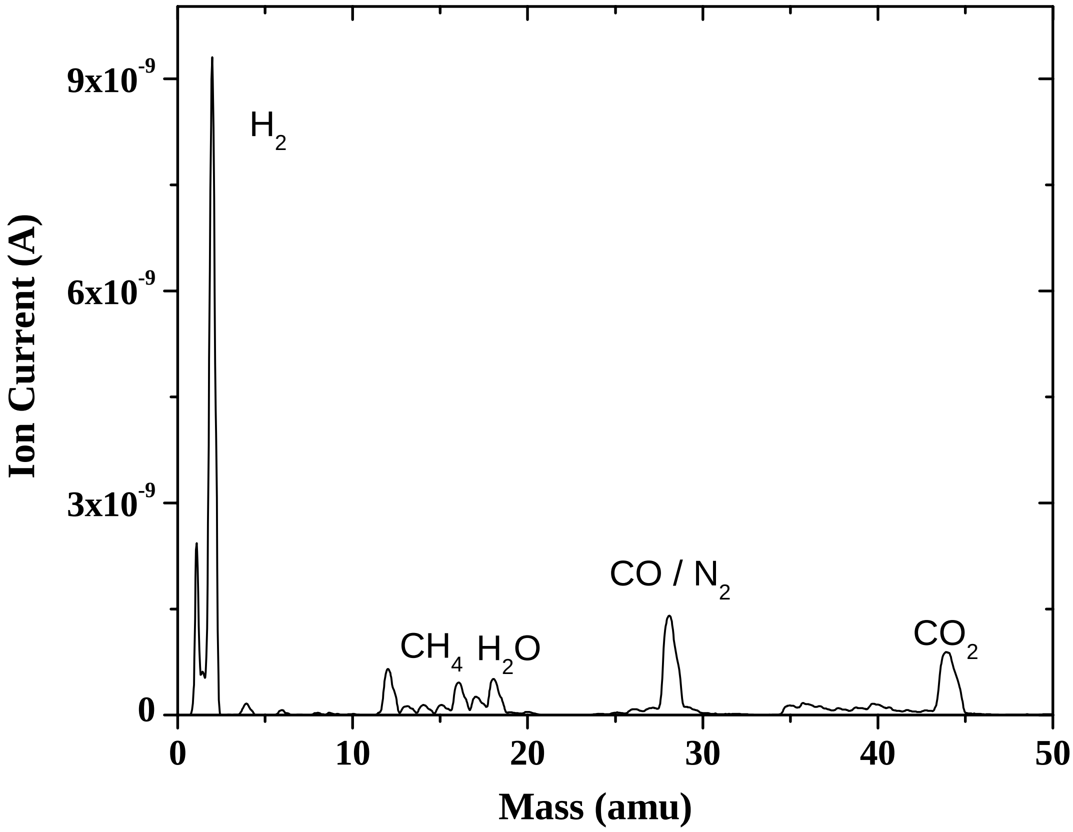

Figure 4.22 Residual gases in the metal MBE/MBD growth chamber after baking (base pressure ~1×10^{-10} torr).

The main residual gases in the system are H_2, CO_2, CO, N_2, H_2O, and CH_4. Baking-out processes remove most of water from the system. H_2 is the dominating gas in the system. Even after baking, water can still be found in the system. It seems to be not possible to totally get rid of water due to the fact that there are always chemical reactions on the surfaces of materials in the vacuum. It should be noted that there are always gases released from the surface of materials in vacuum. CO is one of the main gases released from stainless steel, which is used for vacuum chambers and vacuum components.

The XPS system has its own load-lock system which has a turbomolecular pump backed with a rotary pump. This provides flexibility to bake the XPS system whenever necessary. XPS is baked in a solid baking box. The XPS system is normally baked at 150°C for 24 hours or at 175°C for 12 hours. The base pressure of the system is about 2×10^{-10} torr. However, the operating pressure during XPS analysis is about 1×10^{-9} torr. The rise of vacuum pressure is caused by the increase of outgassing from the operation of X-ray tube. The ultimate vacuum pressure in the R2P2 radial transfer chamber is about 2×10^{-9} torr.

The additional sample is currently not connected to the R2P2 transfer system due to the space limitation. However, the system is used for surface cleaning of a sample prior to introducing into the experimental station of the BL4 beamline to speed up the cleaning procedure in the experimental station.

4.2.3 Sample Preparation

A clean and well ordered surface is necessary for ARPES measurements and for MBE growth. Two different kinds of substrates have been used for the test and commissioning the upgraded experimental station. Those substrates were Si(100) and Cu(110) single crystals. Si(001) substrate was chosen as an example for metal-semiconductor interface research problems. It is relatively simple to clean Si(001) to obtain a clean and well define surface. Cu(110) was chosen as an example for research on magnetic thin film. Copper is noble and non-magnetic materials. It is a suitable substrate to allow some measurement techniques such as SMOKE to get information only from the overlayer.

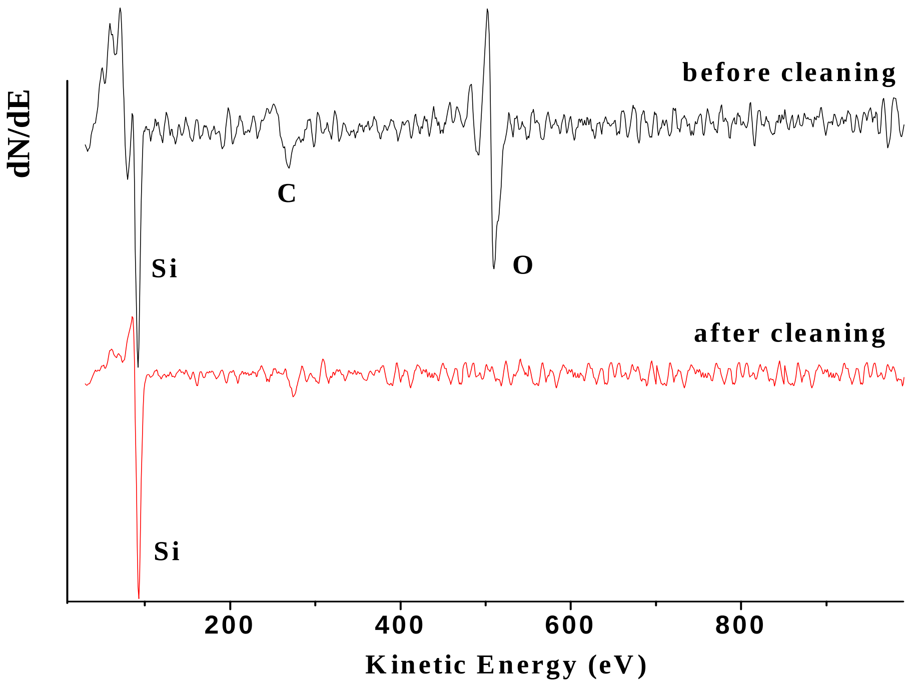

Figure 4.23 AES spectrum taken from the Si(001) before and after cleaning procedures.

Before introducing into the experimental station, a *p-type* Si(001) substrate was first treated chemically with an RCA (Radio Corporation of America) cleaning procedure ($NH_4OH:H_2O_2:DI = 1:1:5$, $HF:DI = 1:50$ and $HCl:H_2O_2:DI = 1:1:6$) to obtain a clean surface with a protective oxide layer (Kern and Puotinen, 1970). After cleaning, the sample was fixed on a molybdenum sample holder. The sample was further cleaned in UHV environment by heating at elevated temperature. Typically, the sample was thermally degassed at about 500°C and then heated at about 850°C for 10 minutes. These procedures results in a clean and well-defined surface with (2×1) two-domain surface reconstruction, as observed from AES and LEED measurements with the results shown in Figures 4.23 and 4.24, respectively.

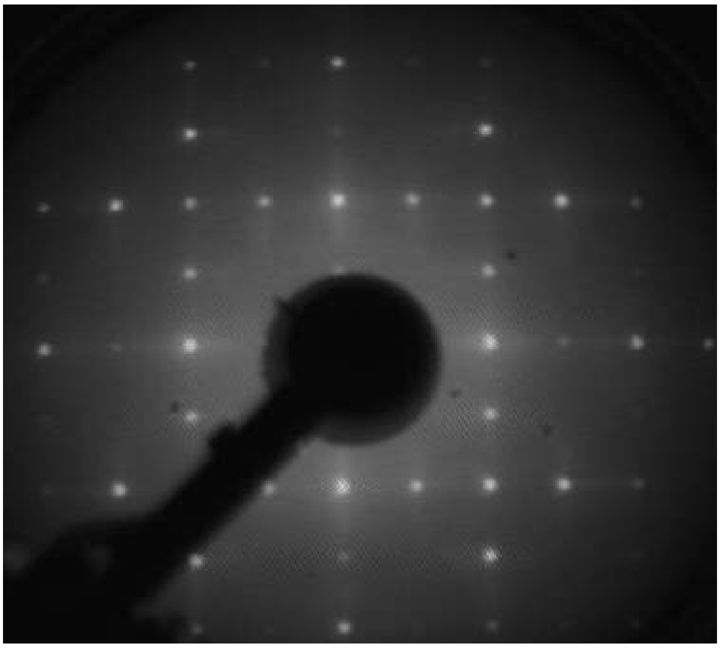

Figure 4.24 LEED pattern taken from a clean Si(001) substrate with electron energy of 120 eV.

For Cu(110) substrate, the sample used is a slice cut out of a single crystal of 99.999%-pure Cu(110) purchased from Good Fellow Cambridge Co.. The slice was grinded and polished by standard procedures until a secular surface was obtained. The sample surface was cleaned with alcohol and pure water in an ultrasonic cleaning machine before introducing into the experimental station. The sample surface was further cleaned in situ in the based vacuum of 10^{-10} Torr. The final cleaning of the sample was made by the repetition of Ar^+ ion bombardment followed by electron bombardment heating at 600^oC. By the AES analyses, the existence of foreign atoms or molecules on the sample surface such as O, S, and CO was examined. Cycles of Ar^+ ion bombardment and baking were repeated for a month before a clean surface was obtained. The well-defined (110) surface was confirmed by measuring the LEED pattern. The AES spectra and LEED pattern confirming the clean and well-defined surface are shown in Figures 4.25 and 4.26, respectively.

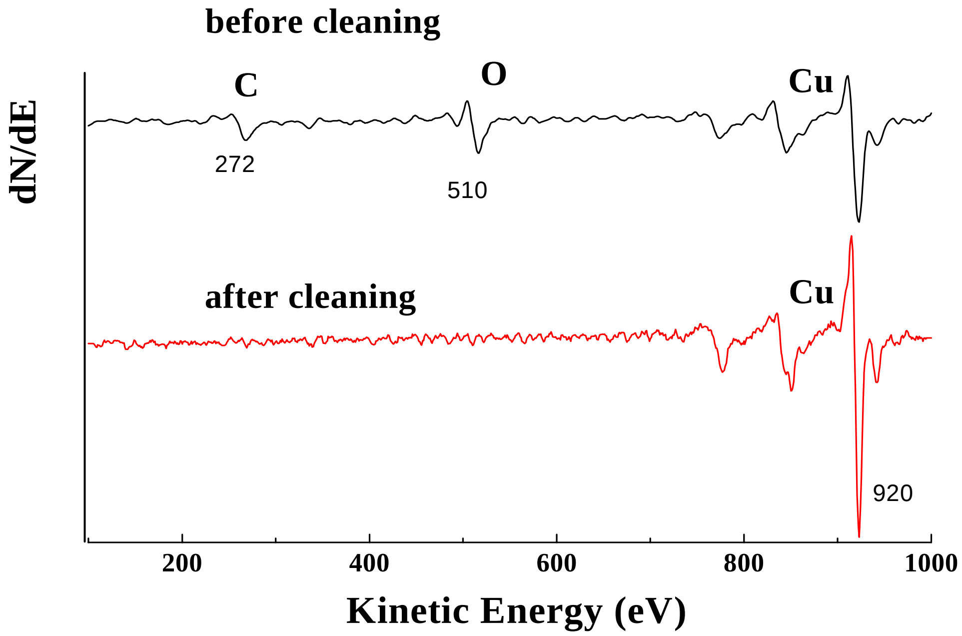

Figure 4.25 AES spectrum taken from the Cu(110) substrate before and after cleaning procedures.

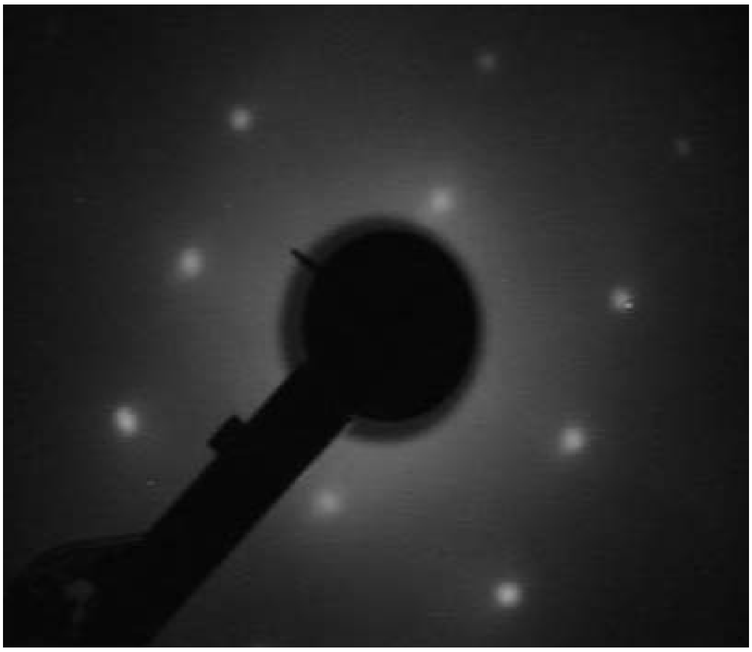

Figure 4.26 LEED pattern taken from a clean and well-defined Cu(110) substrate with electron energy of 200eV.

4.2.4 Growth/Deposition of Thin Film

Two different kinds of sources are available in the MBE/MBD system. Those are a mini electron-beam evaporator and an effusion cell. Figure 4.27 shows the relation between the input power and the temperature of the effusion cell. The crucible dimension used in this work was 10 cm^3. The maximum temperature of the effusion cell is in fact about 1500°C for a 10-cm^3 crucible.

Figure 4.27 shows the relation between the input power and temperature of the effusion cell. The crucible was loaded with Mn flake, the maximum temperature of the cell was controlled to be at 1082°C. The relation between the input power and temperature is also show for the case when there is material loaded in the crucible. The open circles are the measurement data while the solid line is given be the manufacturing.

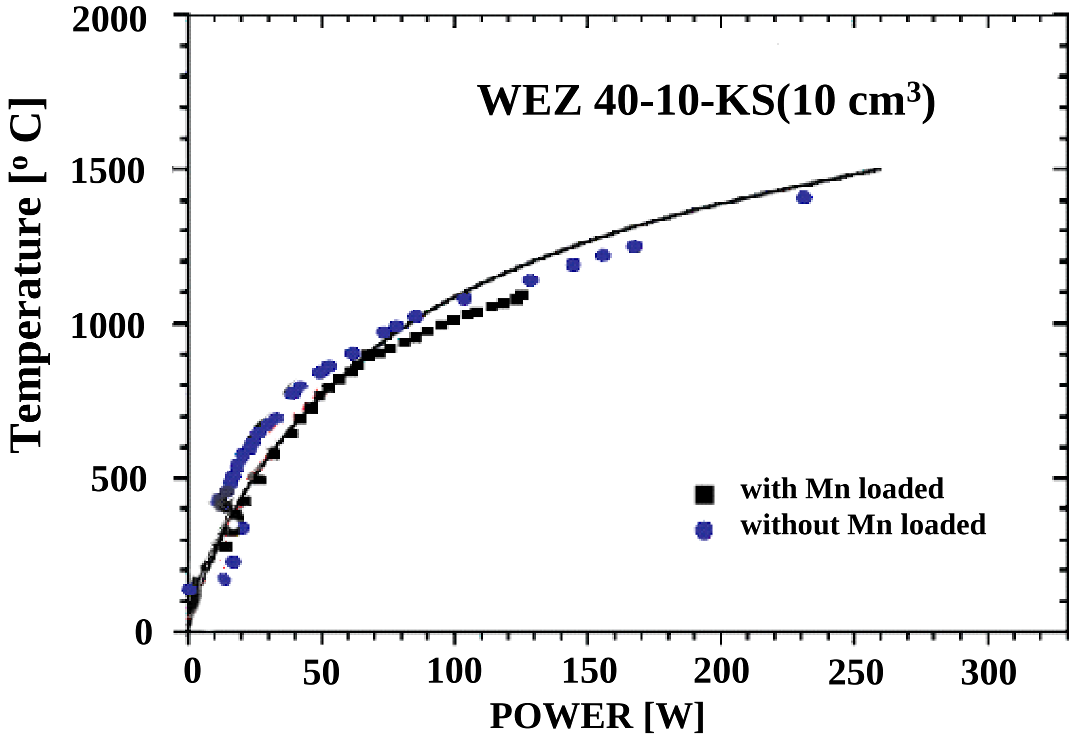

Figure 4.27 Relation between the input power and temperature of the effusion cell.

4.2.4.1 Mn deposition on Si(001)

Figure 4.28 show AES spectra taken from a clean Si(100) substrate before and after deposition of Mn at different temperature of the effusion cell. All depositions were done at room temperature for the same duration of 10 minutes in the MBE/MBD chamber. The vacuum pressure was about ~ 6.5×10^{-9} - 1.0×10^{-8} torr during the deposition. The sample was transferred from the MBE/MBD chamber to the photoemission analysis chamber for AES measurement. When the temperature of the effusion cell is 750°C, a very small amount of Mn was observed on the surface of the substrate. The amount of Mn on the substrate increases with the temperature of the effusion cell. From AES measurements, it was found that the amount of Mn was equivalent to 12.25%, 23.18%, and 95.21% (0.12, 0.23, and 0.95 monolayer), corresponding to the deposition rate of 0.01, 0.02 and 0.1 monolayer/min, when the cell temperature was 800°C, 850°C, and 900°C, respectively.

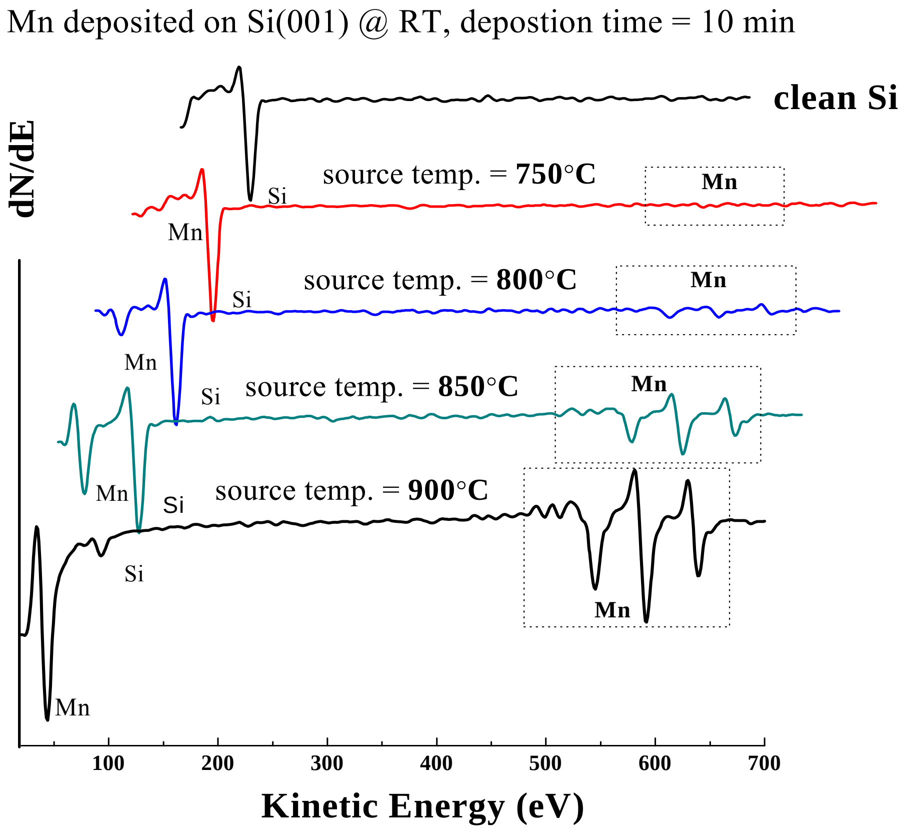

Figure 4.28 AES spectra of a clean Si(001) substrate before and after Mn deposition at different cell temperatures.

In addition to AES measurements, photoemission measurements using synchrotron light were also carried out with the same CLAM2 energy analyzer in the same chamber as AES measurements. Figure 4.29 shows EDCs of a clean Si(100) substrate before and after Mn deposition at different cell temperatures. The EDCs were taken with 60-eV excitation light. The work fucntion of the energy analyzer is 4.2 eV. Thus, the Fermi level corresponds to the kinetic energy of photoelectron of about 55.8 eV. The region between 50 eV and the Fermi level are the contribution from the electrons in the valence band. It can be seen clearly that the surface changes from the semi-conducting state the conducting state when the Mn surface concentrate increases.

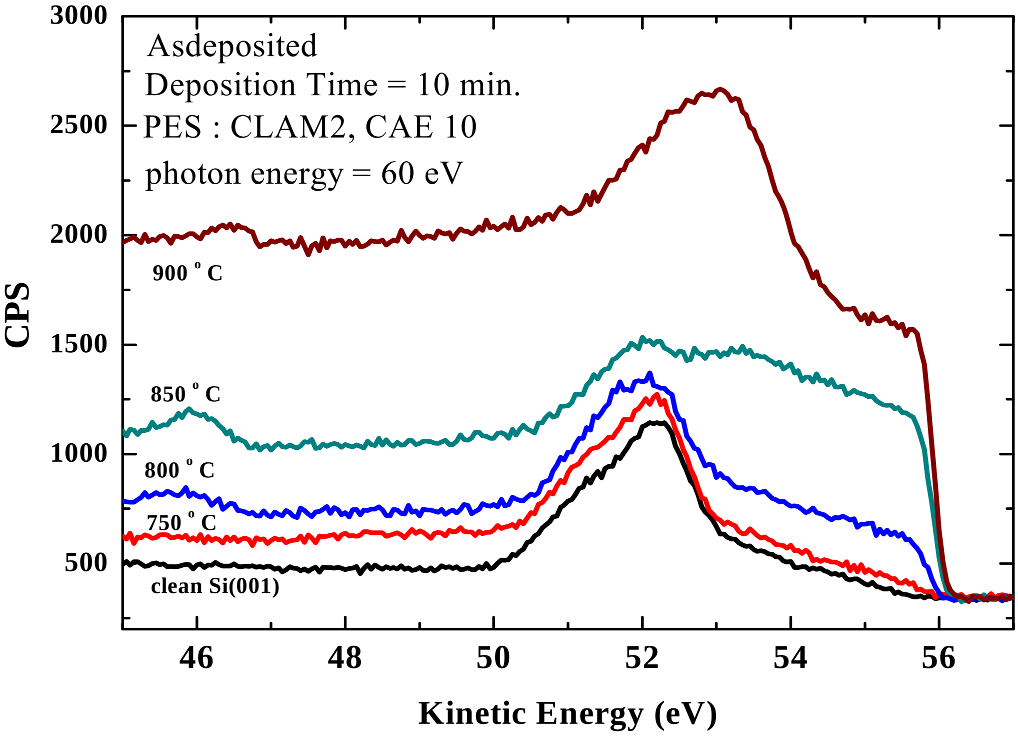

Figure 4.29 EDC of a clean Si(100) substrate before and after Mn deposition at different cell temperatures.

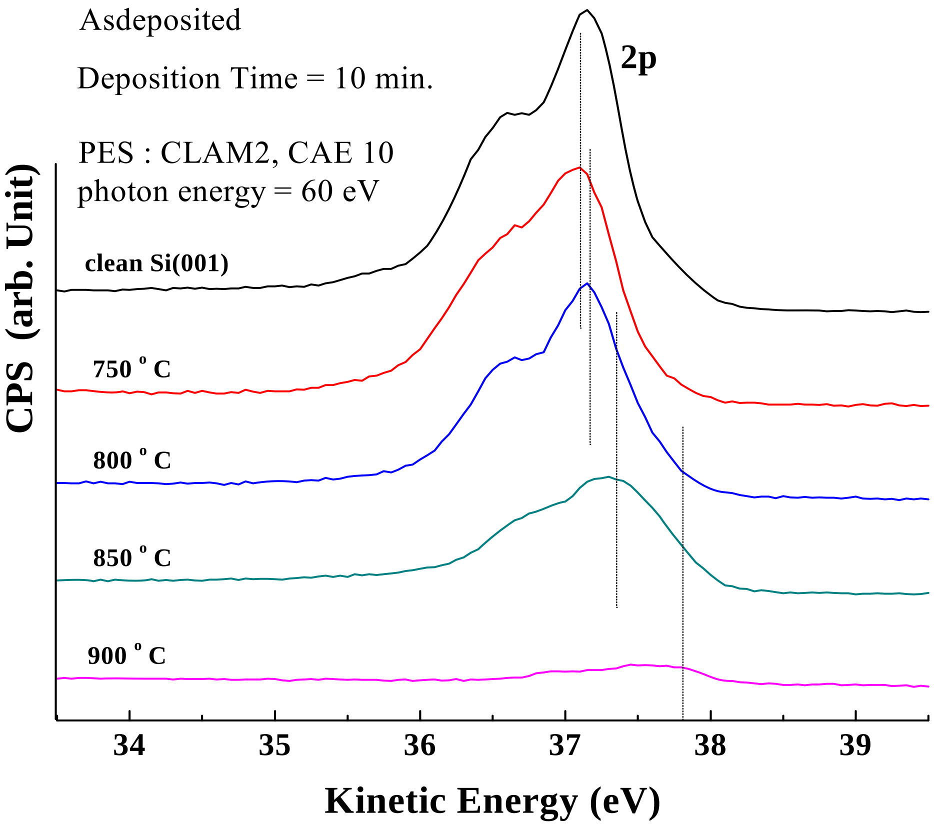

Figure 4.30 EDC showing the chemical shift of Si 2p taken from a clean Si(100) substrate before and after Mn deposition at different cell temperatures.

Figure 4.30 shows EDC taken around Si $2p_{1/2}$ and $2p_{3/2}$ levels from a clean Si(100) substrate before and after Mn deposition at different cell temperatures. The Si $2p_{1/2}$ and $2p_{3/2}$ peaks become smaller when the temperature of the effusion cell increases. This indicates that the thick of the deposited layer increase with temperature of the effusion cell. It is interesting to note that the Si $2p_{1/2}$ and $2p_{3/2}$ peaks shift towards higher kinetic energy, or lower binding energy. The shift of the binding energy indicates the formation of Mn silicide.

4.2.4.2 Mn deposition on Cu(110)

Growth of Mn on Cu(110) has also been experimented. A Cu(110) disc with clean and well-defined surface was use as a substrate. AES spectra in Figure 4.28 indicate a clean Cu(110) substrate with impurities below the detection level. After growth of Mn on the Cu(110) substrate, the amount of Mn deduced from the AES result spectrum in Figure 4.28 is equivalent to 0.37 monolayer. The growth rate is estimated to be about 0.12 monolayer per minute. The sligth difference in the deposition rate, comparing to the growth of Mn on Si, may be due to the difference in the sticking coefficient.

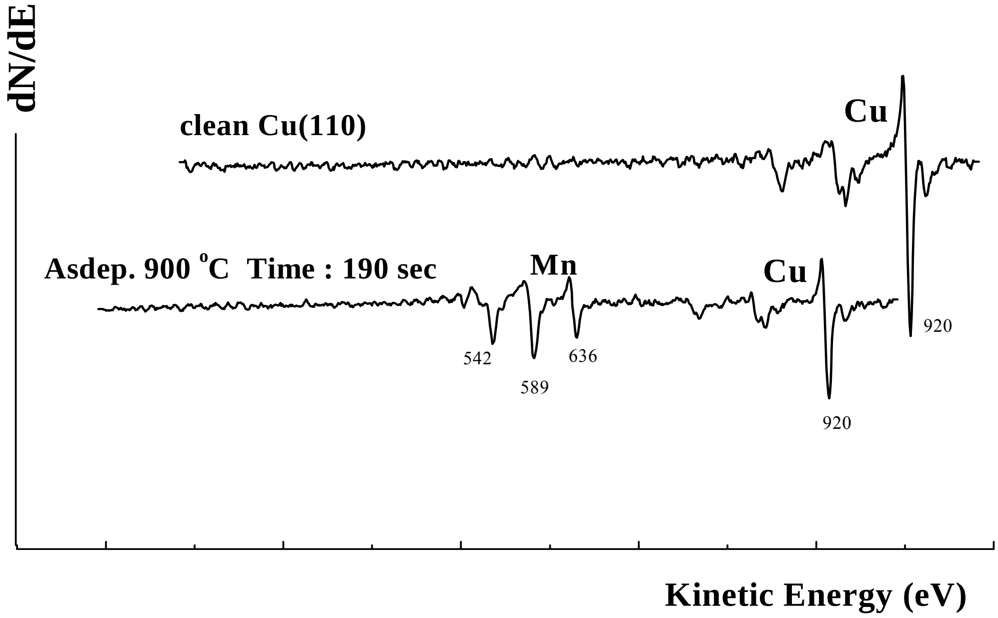

Figure 4.31 AES spectra of a clean Cu(110) substrate before and after Mn deposition at cell temperature of 900°C for 190 seconds.

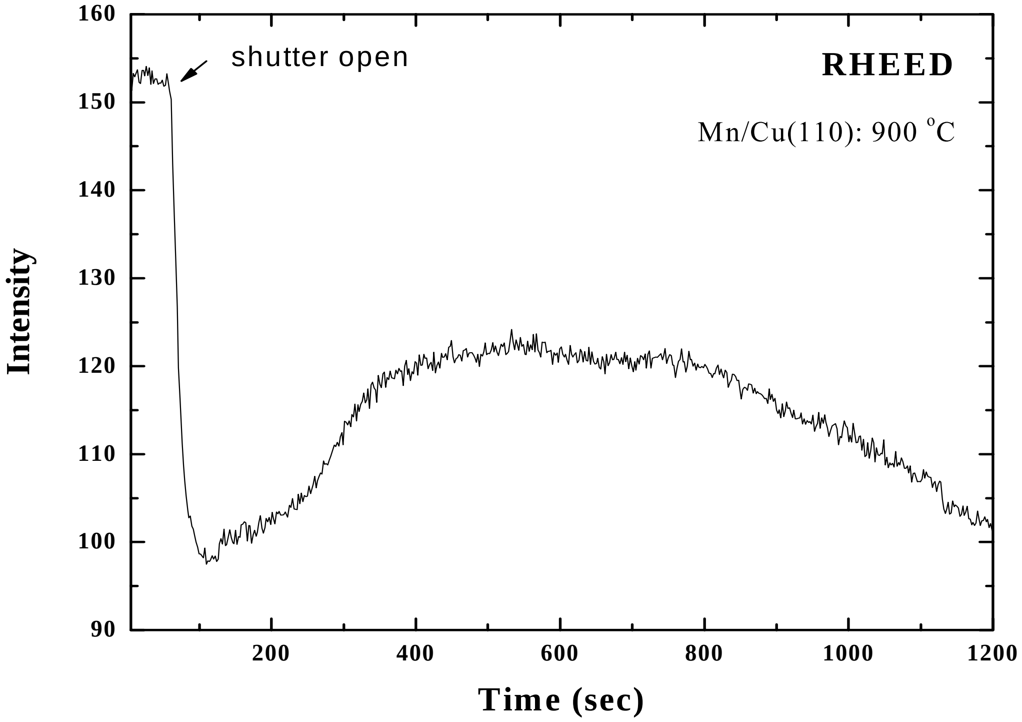

Figure 4.32 RHEED intensity as a function of deposition time.

Figure 4.32 shows RHEED intensity during growth of Mn on Cu(110). The RHEED intensity drops suddenly when the shutter of the effusion cell is opened. The RHEED intensity increases with time and reaches the maximum at about 500 seconds after opening of the shutter. The increase of the RHEED intensity indicates, likely epitaxial, growth of Mn overlayer on the substrate in the initial stage. After that, the RHEED intensity reduces and approaches a certain minimum intensity as the growth proceeds. The absence of the RHEED intensity oscillation may also be caused by the that Cu(110) surface contain steps, which results in no change of the surface roughness as the growth proceed when the incorporation of growth atoms are at the step edges.

CHAPTER V

CONCLUSIONS

In conclusions, the followings have been achieved during the course of this thesis work:

- The BL4 beamline has been optimized to meet the design specifications. The resolving power of the monochromator has reached its designed value of 5000. This will allow this beamline to be able for the investigations of fine structure. Suppression of high-order lights have successfully been demonstrated. Considering excitation energy, an aluminum foil is a suitable filter to be used to suppress the 2nd-order light for the investigation of 3p-3d resonance photoemission for most 3d magnetic materials.
- The experimental station of the BL4 beamline has been upgraded to meet the increasing demands and the number of users. The demand for more efficient use of allocated synchrotron light beamtime can now be satisfied with the use of a multi-UHV-chamber system to allow photoemission measurements using synchrotron light to be performed in parallel with the preparation and/or with *in situ* surface analysis of other samples. The upgraded system ensures variability, providing a multiple propose experimental station for surface and interface research. More importantly, the techniques are *in situ* techniques. The standard surface-sensitive

techniques available, in addition to ARPES and AIPES using synchrotron light, are UPS, XPS, AES and LEED.

- A metal MBE/MBD system has been constructed and connected to the multi-UHV-chamber system of the experimental station of the BL4 beamline. The growth/deposition of magnetic ultra-thin films on Si(100) and Cu(110) substrates and *in-situ* characterizations of the substrates and films have successfully been demonstrated.

Remarks

The new experimental station developed in this thesis work has already been used for the investigations of electronics structure of low-dimensional magnetic materials. The work in whichI have partially participated, in is the investigation of the electronic structure of oxygen-adsorbed Ni(111). The results of this work have already been accepted for publication in Journal of the Physical Society of Japan. The system has also being used for the investigation of Ni films on Cu(100) and metal-GaN contact.

In a long term, I do hope that the system developed in this work will be useful for a Thai surface and interface research community, though it is a very small community.

REFERENCES

REFERENCES

Berman, A. (1992). **Vacuum Engineering Calculations, Formulas, and Solved Excercises**, Academic Press, Inc.

Bertolini, L. R. (2004). **Accelerator Vacuum and Mechanical Engineering**, Lawrence Livermore National Laboratory, United States Particle Accelerator School, The College of William and Mary.

Biedermann, A., Schmid, M., and Varga, P. (2001). Crystallographic structure of ultrathin Fe films on Cu(100). **Physical Review Letters** 87(8) : 86103.

Contnenza, A., Massidda, S., and Freeman, A. J. (1990). Magnetic and electronic properties and Schottkey barrier in $Fe_n/(ZnSe)_m(001)$ superlattics. **Physical Review B** 42(5) : 2904-2913.

Domke, M., Schulz, K., Remmers, G., and Kaindl, G. (1996). **Physical Review A** 53, 1424.

Duke, P. J. (2000). **Synchrotron Radiation Production and Properties.** New York, Oxford university press.

Durr, W., Taborelli, M., and Landolt, M. (1989). Magnetic phase transition in two-dimensional ultrathin Fe film on Au(100). **Physical Review Letters** 62(2) : 206-209.

Escorcia-Aparicio, E. J., Kawakami, R. K., and Qui, Z. Q. (1996). fcc-Fe films grown on a ferromagnetic fcc-Co(100) substrate. **Physical Review B** 54(6) : 4155-4158.

Hayashi, K., Sawada, M., and Kakizaki, A. (2001). Structure and magnetism of Fe thin films grown on Rh(001) studied by photoelectron spectroscopy. **Physical Review B** 64 : 054417.

Hernnas, B., Karolewski, M., Tillborge, H., and Martensson, N. (1994). On the growth of Ni on Cu(100). **Surface Science** 302(1-2) : 64-72.

Hilleret N., (1999-2005). **Mechanical pump**, Switzerland, Geneva, CERN.

Hofmann, P. (2005). **Lecture notes on surface science.** Arhus university.

Horn, K., and Scheffler, M. (2000). **Handbook of surface science (Vol. 2): Electronic structure.** North Holland, Amsterdam.

Huang, F., Kief, M. T., Mankey, G. J., and Willis, R. F. (1994). Magnetism in the few-monolayers limit: A surface magneto-optic Kerr-effect study of the magetic behavior of ultrathin films of Co, Ni and Co-Ni alloys on Cu(100) and Cu(111). **Physical Review B** 49(6) : 3962-3973.

Kadau, K., and Entel, P. (1999). Atomistic study of structural transformation in thin iron films on copper. **Journal of Magnetic Matterials** 198-199 : 531.

Kantee, S. (2004). Development of angle-integrated photoemission spectroscopy system using synchrotron light. **Ph.D. Dissertation**, Suranaree University of Technology, Thailand.

Kern. W., and Puotinen, D. A. (1970). Cleaning solutions based on hydrogen peroxide for use in silicon semiconductor technology. **RCA Review** 31: 187-206.

Jonker, B. T., Walker, K. H., Kisker, E., Prinz, G. A. and Carbone, C. (1986). Spin – polalized photoemission study of epitaxial Fe(001) films on Ag(001). **Physical Review Letters** 57(1) : 142-145.

Kadau, K., and Entel, P. (1999). Atomistic study of structural transformation in thin iron films on copper. **Journal of Magnetic Matterials** 198-199 : 531.

Kim, J. S., Hohamed, M. H., and Kesmodel, L. L. (1992). Vibrational spectroscopy of ordered oxygen adiayers on Ni/Cu(001) and Co/Cu(001) thin film systems. **Surface Science** 260(1-3) : 185-190.

Kittel, C. (1996). **Introduction to Solid State Physics.** (7th ed.). New york : John Wiley & Sons, Inc.

Klasger, R., Schmitz, D., Carbone, C., Eberhardt, W., and Kachel, T. (1998). Surface manetism and electronic structure of ultra thin fcc Fe films. **Solid State Communication** 107(1) : 13-18.

Li, D., Freitag, M., Pearson, J., Qiu, Z. Q., and Bader, S. D. (1994). Magnetic phases of ultrathin Fe Groun on Cu(100) as epitaxial wedges. **Physical Review Letters** 72(19) : 3112-3115.

Li, Y., and Baberschke, K. (1992). Dimensional crossover in ultrathin Ni(111) films on W(110). **Physical Review Letters** 68(8) : 1208 -1212.

Macedo, W. A., and Keune, W. (1988). Magnetism of epitaxial fcc-Fe(100) films on Cu(100) investigated *in situ* by conversion-electron Mossbauer spectroscopy in ultrahigh vacuum. **Physical Review Letters** 61(4) : 475-479.

Moruzzi, V., Janak, J. F., and Williams, A. R. (1978). **Calculated Electronic Properties of Metals.** New York, Pergamon.

Nakajima, H., et al. (2007). **The Eighth International Conference on Synchrotron Radiation Instrumentation.** Vol. 879: 543.

Pappas, D. P., et al. (1991). Magnetism of ultra thin films of Fe on Cu(100). **Journal of Applied Physics** 69(8) : 5209-5211.

Pashley, D. W. (1990). **Growth and Characterisation of Semiconductors**. New York, Bristol, Adam Hilger.

Peatman, W.B. (1997). **Grating, Mirrors and Slits Beamline Design for Soft X-Ray Synchrotron Radiation Sources**. Amsterdam: Gordon and Breach Science Publishers.

Pinski, P. J., Staunton, J., Gyortfy, B. L., and Stock, G. M. (1986). Ferromagnetism versus antiferromagnetism in face-centered ion. **Physical Review Letters** 56(19) : 2096-2099.

Ploog, K. (1988). **Microscopical structuring of solids by molecular beam epitaxy**. Angewandte Chemie - Int. English ed, 27(5):593-621

Qian, D., Jin, X. F. (2001). Spin-density wave in ultrathin Fe films on Cu(100). **Physical Review Letters** 87(22) : 227204.

Raeker, T. J., and De Pristo, A. E. (1992). Alloy formation energetics and dynamics in the Ni/Cu(100) and Ni/Cu(111) systems. **Vacuum Science and Technology A** 10(4) : 2396-2399.

Schulz, B., and Baberschke, K. (1994). Crossover from in-plane to perpendicular magnetization in ultrathin Ni/Cu(001) films. **Physical Review B** 50(18) : 13467-13472.

Schulz, B., Schwarzwald, R., and Baberschke, K. (1994). Magnetic properties of ultrathin Ni/Cu(100) films determined by a UHV-FMR study. **Surface Science** 307-309(2) : 1102-1108.

Songsiriritthigul, P. (1997). **Silicon-Germanium alloy layers formed by solid phase epitaxial growth of Germanium ion silicon**. Chalmers university of technology, Sweden, Goteborg.

Songsiriritthigul, P., Pairsuwan, W., Ishii, T., and Kakizaki, A. (2001). Photoemission at the Siam Photon Labolatory. **Surface Review and Letters** 8(5) : 497-500.

Stampanoni, M., Vaterlaus, A., Aeschlimann, M., and Meier, F. (1987). Magnetism of epitaxial bcc iron on Ag(001) observed by spin-polarized photoamission. **Physical Review Letters** 59(21) : 2483-2485.

Varian, Inc. (2006). **Vacuum Technologies**, Product Catalog 2006 (April 06).

Vollmer, R., and Kirschner, J. (2000). Influence of H_2 adsorption on magnetic properties of Fe films on Cu(001). **Physical Review B** 61(6) : 4146-4154.

Yeh, J.-J., and Lindau, I., (1985). Atomic subshell photoionization cross sections and asymmetry parameters: $1< z <103$. **Atomic Data and Nuclear Data Tables** 32, 1.

APPENDICES

APPENDIX A

PERFORMANCE OF THE BL4 BEAMLINE FOR SURFACE AND INTERFACE RESEARCH AT THE SIAM PHOTON LABORATORY

Performance of the BL4 Beamline for Surface and Interface Research at the Siam Photon Laboratory

Hideki Nakajima[1], Moragote Buddhakala[2], Somchai Chumpolkulwong[2], Ratchadaporn Supruangnet[2], Akito Kakizaki[3], Prayoon Songsiriritthigul[1, 2]

[1]*National Synchrotron Research Center, 111 University Avenue, Muang District, Nakhon Ratchasima 30000, Thailand* [2]*School of Physics, Suranaree University of Technology, 111 University Avenue, Muang District, NakhonRatchasima 30000, Thailand* [3]*Institute for Solid State Physics, The University of Tokyo, Kashiwa, Chiba 227-8581, Japan*

Abstract. The evaluations of the monochromator of the BL4 beamline at the Siam Photon Laboratory were carried out by gas-phase photoionization measurements. The beamline employs a varied-line-spacing plane grating monochromator, which delivers photons with energies between 20-240 eV. The resolving power of the monochromator depends strongly with the alignment of the exit slit. The designed resolving power of 5000 has been achieved. The experimental station of the beamline has been upgraded for surface and interface research. The new experimental station removes the disadvantage and expands the capabilities of the old one in such a way that photoemission experiments using synchrotron light can be performed in parallel with other in situ surface analysis techniques, as well as with preparation of other samples. The new system includes the old photoemission system and a multi-UHV-chamber system. The standard surface-sensitive techniques available in addition to photoemission spectroscopy using synchrotron light are UPS, XPS, AES and LEED. The new experimental station also includes a metal MBE system for preparing samples for the studies of ultra-thin magnetic films and metal-semiconductor interfaces.

Keywords: Varied line spacing plane grating monochromator, UPS, XPS, AES, LEED, RHEED, MBE.**PACS:** 07.85.Qe, 33.60.Cv

PERFORMANCE OF THE BEAMLINE

The BL4 beamline at the Siam Photon Laboratory was constructed for solid state spectroscopic research and related phenomena. The beamline delivers photons with energy between 20 eV and 240 eV. The detailed descriptions of the beamline were reported elsewhere [1]. Our recent commissioning results, presented at SRI2003 [2], were obtained during the initial operation of the Siam Photon Source with unstable electron beam. With the improvement of the light source, fine tuning of the monochromator could be carried out. It was found that the intermediate aperture in the dispersion direction (Y aperture), located between the entrance slit and the focusing mirror of the monochromator, greatly influenced on the resolution. This is because the gratings were installed in the reversed direction resulting in poor resolving power. After the correction of the gratings, the performance optimization of the monochromator was done by means of gas-phase photoionization measurement. The spectral widths of measured atomic resonance depend on the instrumental resolution of beamline at particular photon energy and the natural widths of the specific resonances.

Gas-phase photoionization measurements were carried out using an existing chamber designed for angle-resolved photoemission measurement. A gate valve with a thin polypropylene window was used to vacuum-isolate the experimental chamber from the optical beamline, allowing the measurements to be carried out at pressures up to 10^{-6} mbar. A capillary tube was used to inlet a gas into the focal position of the beam. A secondary electron multiplier was installed within striking distance of gas nozzle to measure electron yield spectra. The size of Y aperture in the measurement is 4 mm, because the small aperture decreased the photon flux without a great improvement of the resolving power.

Photoionization spectrum taken from the $2,0_4$ resonance of doubly excited helium is shown in Fig. 1. In Fig. 1, the measured spectrum represented by open circles was fitted with Fano profile convoluted with a Gaussian. Fano parameter q=-2.4 and line width Γ=0.004 eV are used from the previously reported values [3].

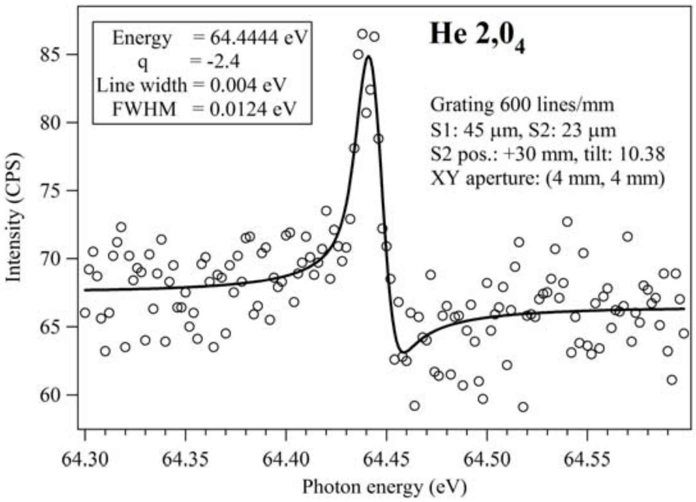

FIGURE 1. Photoionization spectrum measured on $2,0_4$ resonance of doubly excited helium. Open circles represent the experimental results, solid line the fitting result using Fano profile convoluted with a Gaussian. Resonance energy, Fano parameter (q), line width and Gaussian width (FWHM) used in fitting are described in the box. The corresponding resolving power here is about 5000.

This result reveals a resolving power of 5000 which is a designed goal of our monochromator. The optimized exit-arm length was 30 mm shorter than the designed one. Figure 2 shows the dependence of the resolution on the exit-slit position. An entrance-slit width (S1) is 45 micron and an exit-slit width (S2) 23 micron, which are calculated from the analytical expressions at 5000 resolving power using parameters of $2,0_4$ resonant excitation energy and groove density of grating (600 lines/mm). The measured resolving powers using various slit widths were also in good agreement with those calculated from analytical expression.

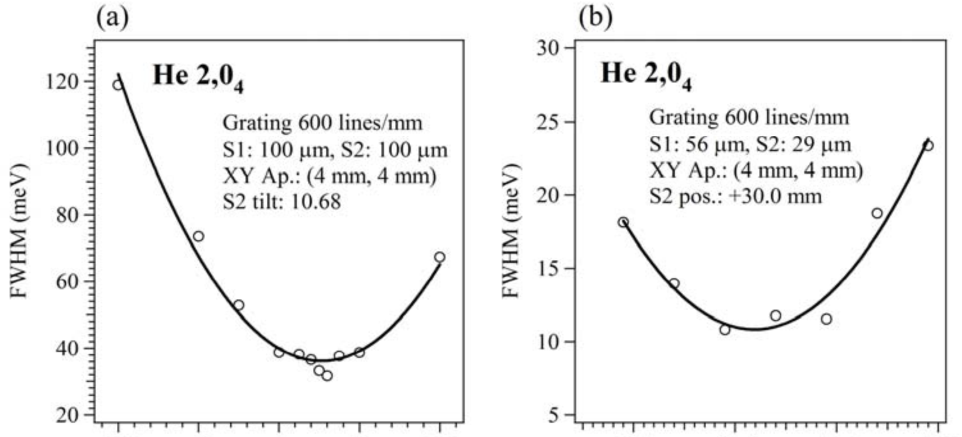

FIGURE 2. The dependence of the resolution on the exit-slit position measured on $2,0_4$ resonance of doubly excited helium. The optimized resolution was obtained in terms of (a) the alignment of exit-slit position in the optical-path direction and (b) the adjustment of tilt of exit slit. Solid lines represent the curves fitted with a quadratic polynomial function.

DEVELOPMENT OF THE EXPERIMENTAL STATION

The old experimental station of the beamline is for angle-resolved photoemission spectroscopy (ARPES) experiments using synchrotron light. The system has three vacuum-isolated chambers, i.e. the analysis chamber, the sample preparation chamber and the load-lock chamber. The sample preparation chamber is mounted on top of the analysis chamber with a gate valve in between. The relocation of the sample between the preparation and analysis chambers is performed by a vertical linear movement of the manipulator. Surface cleaning of a crystalline sample may be performed by ion sputtering or/and heating in the preparation chamber.

Although photoemission spectroscopy is a very powerful tool for studies of occupied electronic states of solids, it is very surface-sensitive. Clean and well-defined surfaces are required to obtain useful information from ARPES measurements. It takes weeks, or in some case a few months, to prepare some materials to obtain clean and well-defined surfaces. The disadvantage of the old experimental station is that sample preparation and photoemission measurement cannot be performed at the same time since the sample preparation chamber and the analysis chamber share the sample manipulator. This limits the number of samples to be investigated at the BL4 beamline. To make the most use of the limited beamtimes, samples must be prepared and characterized before they are transferred into the photoemission system. Thus the old experimental station has been upgraded with a multi-UHV-chambers system to allow photoemission measurements to be performed while preparing or/and characterizing other samples.

Design Considerations

The main goal for the upgrade of the experimental station of the BL4 beamline is to serve the increasing demands of the users. The demand for more efficient use of allocated beamtimes can be satisfied with the use of a multi-UHV-chamber system to allow photoemission measurements using synchrotron light to be performed in parallel with the preparation and/or with in situ surface analysis of other samples. The major aim in the design of the new experimental station is also to ensure variability, i.e., provide a multiple purpose experimental station for surface and interface research, where a number of *in situ* surface analysis techniques are available. The standard surface-sensitive techniques available in addition to ARPES using synchrotron light are ultraviolet photoelectron spectroscopy (UPS), X-ray photoelectron spectroscopy (XPS), Auger electron spectroscopy (AES), and low-energy electron diffraction (LEED).

Sample preparation systems of users may also be connected to the new experimental station to utilize the *in situ* analysis techniques. Connection or disconnection of the extra sample preparation systems does not interfere with the rest of the system, i.e. no breaking the UHV condition. In parallel with this upgrade, a metal molecular beam epitaxy (MBE) system has been constructed and attached to the multi-UHV-chamber system. The MBE has been being used for depositing or growing ultra-thin metal films on various substrates for the studies of ultra-thin magnetic films and metal-semiconductor interfaces.

The New Experimental Station

The new experimental station includes the old photoemission system and a multi-UHV-chamber system, as shown in Fig. 3. The essential part of the multi-UHV-chamber system is the sample transfer system, which consists of grips, mechanical hands, transfer rods and linear and radial sample transporters. With the transfer system, samples can be transferred among different UHV chambers providing the possibility for *in situ* studies. The VG R2D2 radial sample transporter has six connecting ports, allowing up to six UHV chambers to be connected. Currently, five ports are used to connect with the old photoemission system, an additional XPS system, an additional sample preparation system, a metal MBE system and a load-lock system. Between the photoemission system and the radial transporter, the VG DB2DD linear sample transporter is used to provide sufficient working space. The vacuum environment of each system can be isolated by closing the gate valves, which are installed between each system and the radial transporter.

Samples may be introduced into the multi-UHV-chamber system without breaking UHV conditions via two different directions, i.e. via the load-lock chamber connected to the radial transporter or via the load-lock chamber of the XPS system. The XPS system was designed to have its own load-lock system to allow samples to be introduced directly into the system since the XPS system is also used for general chemical analysis. Mechanical hands and grips are used for moving the sample between the sample manipulators and the sample carriers of the transporters or of the transfer rods.

In this upgrade, only the X-ray source is removed from the old photoemission system and installed on the new XPS system. ARPES, UPS, LEED and AES can still be performed in the old photoemission system. The electron spectrometer of the new XPS system employs the Thermo VG Scientific alpha 110 electron energy analyzer. Surface cleaning of the sample is also possible with Ar^+ ion sputtering in the XPS system.

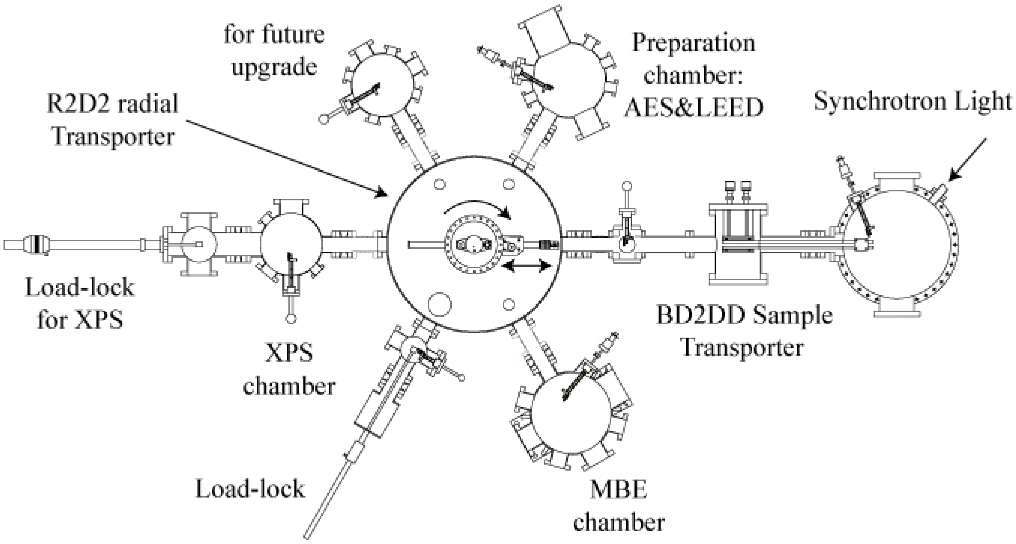

FIGURE 3. Schematic diagram of the new experimental station of the BL4 beamline at the Siam Photon Laboratory.

The additional sample preparation system is used for preparing cleaned and well-defined solid surfaces. Surface cleaning may be performed by ion sputtering and/or electron-beam bombardment heating. The system is also equipped with AES and LEED systems. The AES system employing a cylindrical mirror analyzer is used for checking surface impurities. LEED is used to verify a well-define surface. After cleaning procedures, the clean and well-defined samples may be transferred to the ARPES system for the investigation of the electronic structure or to the MBE system for growing an ultra-thin metal film.

The MBE system is equipped with two effusion cells and a mini e-beam evaporator. RHEED is used for real-time monitoring during growth. The substrate may be heated up to 1200 °C by using an electron-beam bombardment heater.

ACKNOWLEDGMENTS

The authors are extremely grateful for the advice offered by Assoc. Prof. S. Suzuki of Tohoku University. They also thank the technical staff of National Synchrotron Research Center for their support.

REFERENCES

1 P. Songsiriritthigul, W. Pairsuwan, T. Ishii and A. Kakizaki, *Surf. Rev. Lett.* **8**, 497 (2001).
2 P. Songsiriritthigul, H. Nakajima, S. Kantee, W. Wongkokua, W. Pairsuwan, T. Ishii and A. Kakizaki, *AIP Conference Proceedings* No. **705**, 372 (2004).
3 M. Domke, K. Schulz, G. Remmers and G. Kaindl, *Phys. Rev.* A **53**, 1424 (1996).

APPENDIX B

ANGLE-RESOLVED PHOTOEMISSION STUDY OF ELECTRONIC STATES IN Ni(111) SURFACE WITH OXYGEN ADSORPTION

Angle-resolved photoemission study of electronic states in Ni(111) surface with oxygen adsorption

Somchai CHUMPOLKULWONG[1,2], Hideki NAKAJIMA[2]*, Moragote BUDDHAKALA[1,2],
Rathadaporn SABRUEANGNET[1,2], Prayoon SONGSIRIRITTHIGUL[1,2] and Akito KAKIZAKI[3]

[1]*School of Physics, Suranaree University of Technology, 111 University Avenue, Muang District, Nakhon Ratchasima 30000, Thailand*
[2]*National Synchrotron Research Center, 111 University Avenue, Muang District, Nakhon Ratchasima 30000, Thailand*
[3]*Insititute for Solid State Physics, The University of Tokyo, Kashiwa, Chiba 277-8581, Japan*

We have investigated surface electronic states of clean and oxygen-adsorbed Ni(111) surfaces using angle-resolved photoemission spectroscopy. Upon oxygen adsorption, c(2x2) and p(1x1) structures appear in 0.51 ML and 0.88 ML O/Ni(111) surfaces, respectively. Comparing experimentally obtained energy dispersion of the surface electronic states with molecular-orbital and energy-band calculations, it is shown that $3d_{xz}$-$2p_x$ and $3d_{yz}$-$2p_y$ anti-bonding π states are responsible for the electronic states at the interface and enhancement of the perpendicular magnetic anisotropy in the oxygen-adsorbed Ni(111) surfaces.

KEYWORDS: angle-resolved photoemission spectroscopy, surface electronic structure, metallic nickel, oxygen adsorption, perpendicular magnetic anisotropy

1. Introduction

In the last decades, magnetic anisotropy of transition-metal thin films is one of the most attractive research fields to develop high-density recording media.1) Among a number of prototype, nickel films were found to be a valuable model because on a copper substrate, they show perpendicular magnetic anisotropy up to several dozen monolayers, which is more favorable for the device application than magnetic films with a few monolayers. It was also found that the transition thickness from in-plane magnetic anisotropy to perpendicular magnetic anisotropy was varied by surface condition of nickel films.[2,3] However, the relationship between the surface condition and the transition of the magnetization direction of the film is not fully understood yet. Since in the device production process, surfaces of magnetic films are prepared not only as clean surfaces but also as gas-adsorbed surfaces, it is important to investigate the electronic structures of gas-adsorbed nickel surfaces by surface-sensitive experimental techniques. For this purpose, we have measured the angle-resolved photoemission (ARPES) spectra of gas-adsorbed nickel surfaces as well as of clean surfaces to analyze the surface effects to the magnetic anisotropy. Molecular-orbital and energy-band calculations were also used as a complementary approach to identify the surface and interface electronic structures.

We have chosen Ni(111) surface and oxygen as adsorbate since the former reveals a closed-pack structure despite large interlayer distance compared with those in others[4] and the latter is suitable for this kind of study due to a large electron affinity as well as a good vacuum compatibility. From the magnetic anisotropy point of view, Ni(111) surface is to be sensitive to adsorbate-induced reorientation of magnetization direction, since the easy magnetization axis of bulk nickel is along [111] direction.[5] In Ni(111) surface, a surface state is observed at 0.25 eV of binding energy and identified to be *sp*-like Λ_1 symmetry states.[6,7] The energy-band dispersion of unoccupied surface states was investigated using momentum-resolved inverse photoemission spectroscopy.[8] Several works on O/Ni and NiO surfaces were reported, so far.[9,10] Experimental studies of c(2×2) O/Ni(111) structure revealed that the energy-band structures originated from O 2*p* states were in a good agreement with the result of an energy-band calculation.[9] However, detail information on the hybridization between Ni 3*d* and O 2*p* states and its relationship to the magnetic anisotropy is not fully understood.

2. Experimental

Photoemission experiments were carried out at BL4 of the Siam Photon Laboratory of National Synchrotron Research Center.[11] The ARPES apparatus consists of an ion gun, an electron gun, a temperature-controlled sample holder and an electron-energy analyzer

(ARUPS10). Pressure in the analysis chamber was below 2×10^{-10} mbar during photoemission measurements. The overall energy resolution of measured spectra resulting 170 meV at 45 eV of photon energy was confirmed on the Fermi edge of a gold sample at room temperature.

The sample treatment was carried out under the following conditions. After degassing of the sample holder, a single-crystal Ni(111) sample (99.999% purity) was bombarded by argon ion with kinetic energy of 1.0 keV with 2.0×10^{-6} mbar to remove sulphur impurity which was monitored by Auger electron spectroscopy (AES). Next, repeated cycles of argon-ion bombardment and subsequent annealing at 720 K reduced the amounts of carbon and oxygen impurities to be negligible. Finally, the long-range order of periodic surface structure was checked by low-electron-energy diffraction (LEED). The sample surface was identified as a clean surface with a very sharp and low-background p(1×1) LEED pattern. An oxygen-adsorbed Ni(111) surface was prepared by introducing oxygen gas into the chamber where a sample was heated at 450 K. During the flow of oxygen gas, the pressure was kept constant at 1.0×10^{-8} mbar. After the surface was exposed to oxygen gas, the surface was checked by LEED patterns and AES measurements prior to photoemission measurement. Upon oxygen adsorption, c(2×2) and p(1×1) structures appear in 0.51 ML and 0.88 ML O/Ni(111) surfaces, respectively. On the basis of stoichiometry analysis, c(2×2) and p(1×1) lattice structures correspond to 0.25 ML and 1.00 ML in non-reconstructed fcc-(111) surface structures.

Since a real surface has lattice-domain structures caused by steps, defects and so on, the observed LEED patterns correspond to surface structures averaged on the area irradiated with the electron beam. Therefore, the surface of c(2×2)-0.51 ML LEED pattern qualitatively corresponds to a multi-domain c(2×2)-0.50 ML O/Ni(111) surface illustrated in Fig. 1. On the other hand, the surface of p(1×1)-0.88 ML LEED pattern corresponds to p(1×1)-1.00 ML O/Ni(111) surface modified by a lack of oxygen adsorbate in the perfect monolayer surface. These correspondences between surface structures and LEED patterns are summarized in Fig. 1.

3. Results and discussion

First, we present how the oxygen adsorption on Ni(111) surface gives an effect on the spectral intensity that is directly related to the atomic and electronic structures in the surface and interface. Figure 2 shows ARPES spectra of the clean, c(2×2)-0.51 ML oxygen-adsorbed and p(1×1)-0.88 ML oxygen-adsorbed Ni(111) surfaces. The excitation light incidents on the sample at 60° and the energy distribution of photoelectrons was measured in normal-emission mode. The photon energy of 45 eV corresponds to the Γ point of bulk Brillouin zone (BZ). To investigate the effects of oxidation to the spectral profiles, each spectrum was normalized to the integrated intensity. In this normalization process, we assumed the same photoionization cross section for Ni 3*d* and O 2*p* states at the photon energy of 45 eV.12) Hence in Fig. 2, the hybridization between Ni 3*d* and O 2*p* states brought about by the oxygen adsorption is appeared as the same amount of the decrease and increase of the spectral intensity in Ni 3*d* and O 2*p* originated spectral profiles, respectively. In Fig. 2, the binding energies of spectral features are indicated by the ticks with letters from **a** to **f**.

Since the oxygen adsorption would break the symmetry of the atomic structure at the surface, the surface states which are observed in the Ni(111) surface disappear on the oxygen-adsorbed surfaces. On the other hand, interface states would appear in the oxygen-adsorbed surface by electron transfer from nickel atoms to adsorbed oxygen due to a large electron affinity of oxygen atom. This results in the surface relaxation increasing the interlayer distance between surface and subsurface layers.13) In Fig. 2, spectral features **a**, **b** and **c** near the Fermi level (E_F) are assigned to be interfacial states, which are enhanced by the oxygen adsorption in the Ni(111) surfaces. The feature **d** does not decrease in the c(2×2)-0.51 ML O/Ni(111) surface, while it decreases on the p(1×1)-0.88 ML surface. Therefore, the peak **d** is to be originated from the electronic structures of subsurface layer. The feature **e** is originated from surface electronic states because its intensity decreases monotonically with oxygen adsorption. The peak **f** is assigned to be electronic states in bulk Ni because the spectral intensity does not change much as the adsorption proceeds. The O 2*p* originated features are overlapped in the higher binding-energy side of the feature **f**. Small binding-energy shift observed in each spectral feature in different surface conditions is caused by the relaxation of the surface atomic structure by oxygen adsorption.

Figure 3 shows ARPES spectra of the clean Ni(111), c(2×2)-0.51 ML O/Ni(111) and p(1×1)-0.88 ML O/Ni(111) surfaces, which were measured along $\overline{\Gamma}$-$\overline{\Sigma}$-$\overline{\mathrm{M}}$ direction in the surface BZ. The geometry of ARPES measurements is shown in the inset of the figure. Emission angle of the photoelectron is indicated on the right-hand side of each spectrum. The $\overline{\mathrm{M}}$ zone edge at E_{F} corresponds to the emission angle around 27°. Tick markers in the normal-emission spectra indicate the spectral features shown in Fig. 2. It should be remarked in the figure that at each point in the surface BZ, the spectral profile strongly depends on the amount of oxygen adsorption. This reveals that the energy dispersion of the electronic states at the interface and subsurface is different in the O/Ni(111) system. To elucidate the effects of oxygen adsorption to ARPES spectra, we obtained difference spectra by subtracting O/Ni(111) spectra from clean Ni(111) spectra. Figure 4 shows the difference spectra of (a) c(2×2)-0.51 ML and (b) p(1×1)-0.88 ML O/Ni(111) surfaces from that of the clean Ni(111) surface. The positive area (black) corresponds to the decrease of spectral intensity due to the oxygen adsorption, while the negative area (gray) indicates the increase of spectral intensity. Tick markers in the normal-emission spectra correspond to the spectral features in Fig. 2.

In both oxygen-adsorbed surfaces, the spectral features **a**, **b** and **c** near E_{F} appear as negative areas in the difference spectra and show energy dispersion along $\overline{\Gamma}$-$\overline{\Sigma}$-$\overline{\mathrm{M}}$ direction in the surface BZ. Since their intensities are suppressed by the increase of the oxygen coverage we assigned these features as the majority-spin interfacial states due to hybridization between Ni $3d$ and O $2p$ states. To confirm this assignment we carried out the first-principle energy-band calculation by using Vienna *ab-initio* simulation package.[14)] The molecular-orbital calculation was also carried out by DV-Xα SCAT package to obtain information of the characteristics of the bonding states between Ni $3d$ and O $2p$ orbitals at the interface.[15)] In both calculations, the oxygen-induced density of states (DOS) was found at the binding energy around 0.5 eV where DOS of clean Ni(111) surface varies smoothly. Figure 5 shows the results of the first-principle energy-band dispersions on the clean Ni(111) and (2×2)-0.25 ML O/Ni(111) surfaces calculated for five-nickel layers using ultra-soft pseudo-potentials. Since the minority-spin states have no significant effect on the oxygen adsorption in the occupied states, only majority-spin states are shown in the figure. In Fig. 5, the majority-spin bands are distributed at the binding-energy region above 0.5 eV in both surfaces. It should be remarked in O/Ni(111) surface that new states appear in the binding-energy region between 0.3 eV and 0.6 eV, which are indicated by thick lines. Although the energy dispersion of the new states does not agree well with that of the observed interfacial states near E_{F}, the binding energies of these new features are in good agreement with oxygen-induced interfacial states observed in the difference spectra in Fig. 4. The results of the molecular-orbital calculation revealed that in the O/Ni(111) surface, the new majority-spin DOS appears at the binding energy of 0.2 eV and they are originated from the anti-bonding states between Ni 3d and O 2p states.

According to the reported molecular-orbital and relativistic energy-band calculations by Hong *et al.*,[2] the interfacial states correspond to the anti-bonding π states of majority spin and the filling of this anti-bonding states causes a strong surface relaxation and buckling in the subsurface layer to enhance the perpendicular magnetic anisotropy. The reorientation of the magnetization direction due to the oxygen adsorption has been explained by quenching the surface anisotropy. In O/Ni/Cu(001) surface,[2,3] the adsorbates effectively suppress the out-of-plane surface-electron orbitals, which results in the decrease of surface in-plane magnetic anisotropy brought about by spin-orbit interaction. To obtain information of the symmetry of the bonding states between Ni 3d and O 2p states in our system, we have measured the polarization dependence of ARPES spectra by changing the incident angle of the excitation light. Figure 6 shows ARPES spectra of the clean Ni(111) and p(1×1)-0.88 ML O/Ni(111) surfaces observed with incident angle of 20° (s-polarization) and 60° (sp-polarization). In the figure, the spectral features **a**, **b** and **c** in the clean Ni(111) surface show larger spectral intensities in s-polarization spectrum than those in sp-polarization spectrum. In ARPES observed in normal-emission mode, the features originated from electronic states with orbital moment perpendicular to the surface would be enhanced in s-polarization geometry. The results reveal that in the clean Ni(111) surface, electronic states near E_{F} dominantly consist of Λ_3 symmetry states.[16–18] This is consistent to the fact that the easy magnetization axis of Ni is along [111] direction.

In p(1×1)-0.88 ML O/Ni(111) surface, the spectral features **a**, **b** and **c** show larger intensities in sp-polarization spectrum than those in s-polarization spectrum. The initial-state symmetries of these features seem to be Λ_1 corresponding to $3d_{x^2-y^2}$ or $3d_{z^2}$ in terms of 3d orbital in the central field. Since Ni $3d_{x^2-y^2}$ state does not make a bond with O 2p states and σ-bonding states between Ni $3d_{z^2}$ and $2p_z$ would not show energy dispersion observed in Fig. 4, the electronic states responsible for the spectral features near E_{F} are assigned to $3d_{xz}$ and $3d_{yz}$ states, which make π bonding states with O $2p_x$ and O $2p_y$ states, respectively. Figure 6 reveals that in O/Ni(111) surface the spectral features near E_{F} are due to the hybridization between Ni $3d$ and O $2p$ states, which decreases the contribution on the out-of-plane electron orbitals and suppresses in-plane magnetic anisotropy of Ni(111) surface by spin-orbit interaction. In the Ni/Cu(001) system, the in-plane magnetic anisotropy is dominant in the sample with Ni films of a few monolayers and perpendicular magnetic anisotropy increases with increase of the Ni film thickness.2) Since ARPES is a surface-sensitive experimental technique, the electronic structures obtained from ARPES spectra reveal characteristics of those within a few monlayers from the surface. Our results obtained in this study correspond to those at the thin end of Ni film in the O/Ni/Cu(001) system, where the in-plane magnetic anisotropy of Ni is suppressed.

In conclusion, the polarization dependence of ARPES spectra elucidates the electron orbital symmetry of the hybridization between Ni $3d$ and O $2p$ states at the O/Ni(111) interface. It is shown that $3d_{xz}$-$2p_x$ and $3d_{yz}$-$2p_y$ anti-bonding π states are responsible for the electronic states at the interface and enhancement of the perpendicular magnetic anisotropy in the oxygen-adsorbed nickel surface.

Acknowledgments

Authors thank all the members of the technical staff of National Synchrotron Research Center for their support. This work was supported by NSRC Grant (1-2548/PS03).

References

1) B. Schulz and K. Baberschke: Phys. Rev. B **50** (1994) 13467.
2) J. Hong, R. Q. Wu, J. Lindner, E. Kosubek and K. Baberschke: Phys. Rev. Lett. **92** (2004) 147202.
3) K. Amemiya, E. Sakai, D. Matsumura, H. Abe, T. Ohta and T. Yokoyama: Phys. Rev. B **71** (2005) 214420.
4) F. Mittendorfer, A. Eichler and J. Hafner: Surf. Sci. **423** (1999) 1.
5) S. Kaya: Science Repts. Imp. Tohoku Univ. **17** (1928) 659.
6) F. J. Himpsel and D. E. Eastman: Phys. Rev. Lett. **41** (1978) 507.
7) F. J. Himpsel, J. A. Knapp and D. E. Eastman: Phys. Rev. B **19** (1979) 2919.
8) A. Goldmann, V. Dose and G. Borstel: Phys. Rev. B **32** (1985) 1971.
9) A. L. D. Kilcoyne, D. P. Woodruff, J. E. Rowe and R. H. Gaylord: Phys. Rev. B **39** (1989) 12604.
10) M. R. Thuler, R. L. Benbow and Z. Hurych: Phys. Rev. B **27** (1983) 2082.
11) H. Nakajima, M. Buddhakala, S. Chumpolkulwong, R. Supruangnet, A. Kakizaki and P. Songsiririt-thigul: in *Proc. 9th Int. Conf. Synchrotron Radiation Instrumentation*, ed. J-Y. Choi and S. Rah (American Institute of Physics, New York, 2007) p. 543.
12) J. -J. Yeh and I. Lindau: At. Data Nucl. Data Tables **32** (1985) 1.
13) A. Eichler and J. Hafner: Phys. Rev. B **62** (2000) 5163.
14) G. Kresse and J. Hafner: Phys. Rev. B **47** (1993) R558.
15) H. Adachi, M. Tsukada and C. Satoko: J. Phys. Soc. Jpn. **45** (1978) 875.
16) J. Igarashi, P. Unger, K. Hirai and P. Fulde: Phys. Rev. B **49** (1994) 16181.
17) A. Yamasaki and T. Fujiwara: J. Phys. Soc. Jpn. **72** (2003) 607.
18) F. Manghi, V. Bellini and C. Arcangeli: Phys. Rev. B **56** (1997) 7149.

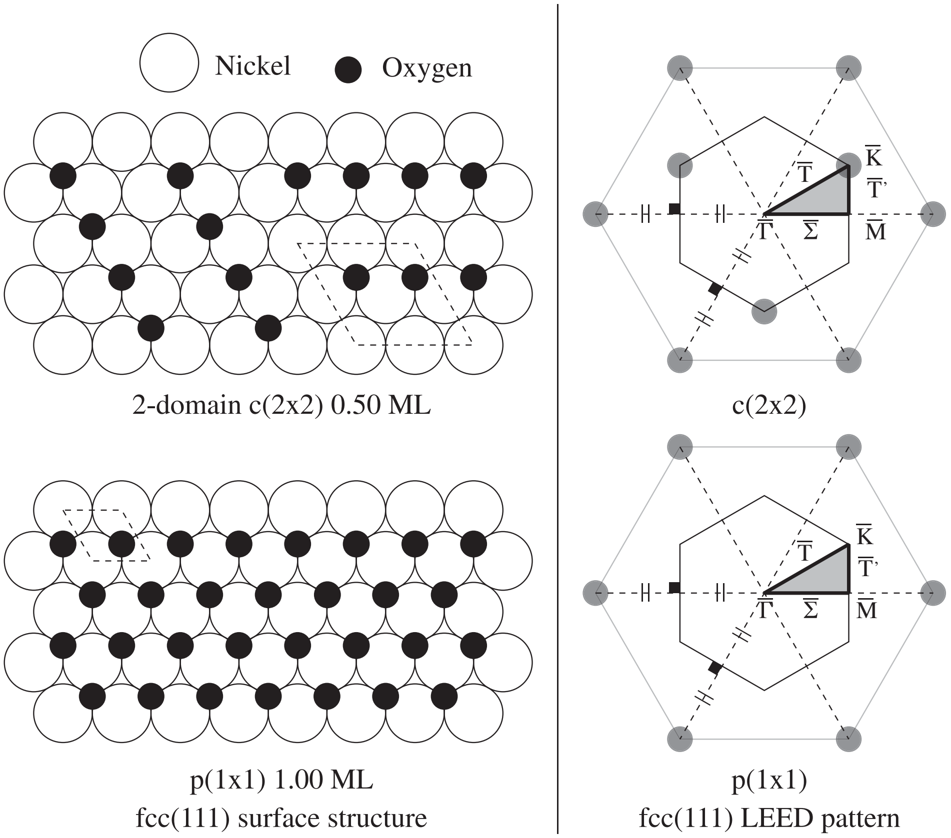

Fig. 1. Schematic illustration of atomic and reciprocal structures on O/Ni(111) surfaces. Left figure shows atomic structure of c(2×2)-0.50 ML (top) and p(1×1)-1.00 ML (bottom) oxygen-adsorbed Ni(111) surfaces. Right figure represents LEED patterns on c(2×2) (top) and p(1×1) (bottom) oxygen-adsorbed Ni(111) surfaces. First Brillouin zones are also illustrated with corresponding irreducible representations in the inset of the illustration of LEED patterns.

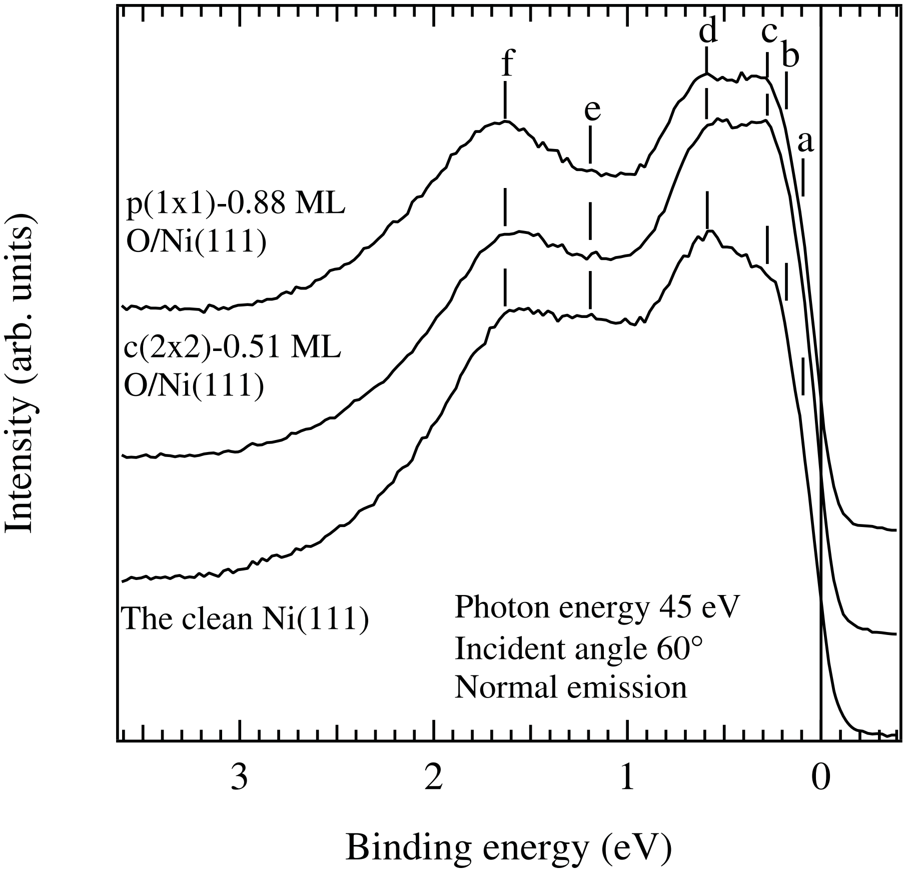

Fig. 2. Normal-emission spectra of the clean, c(2×2)-0.51 ML oxygen-adsorbed and p(1×1)-0.88 ML oxygen-adsorbed Ni(111) surfaces. Photons with energy of 45 eV incident on the sample at 60° and photoelectrons are measured in normal-emission mode.

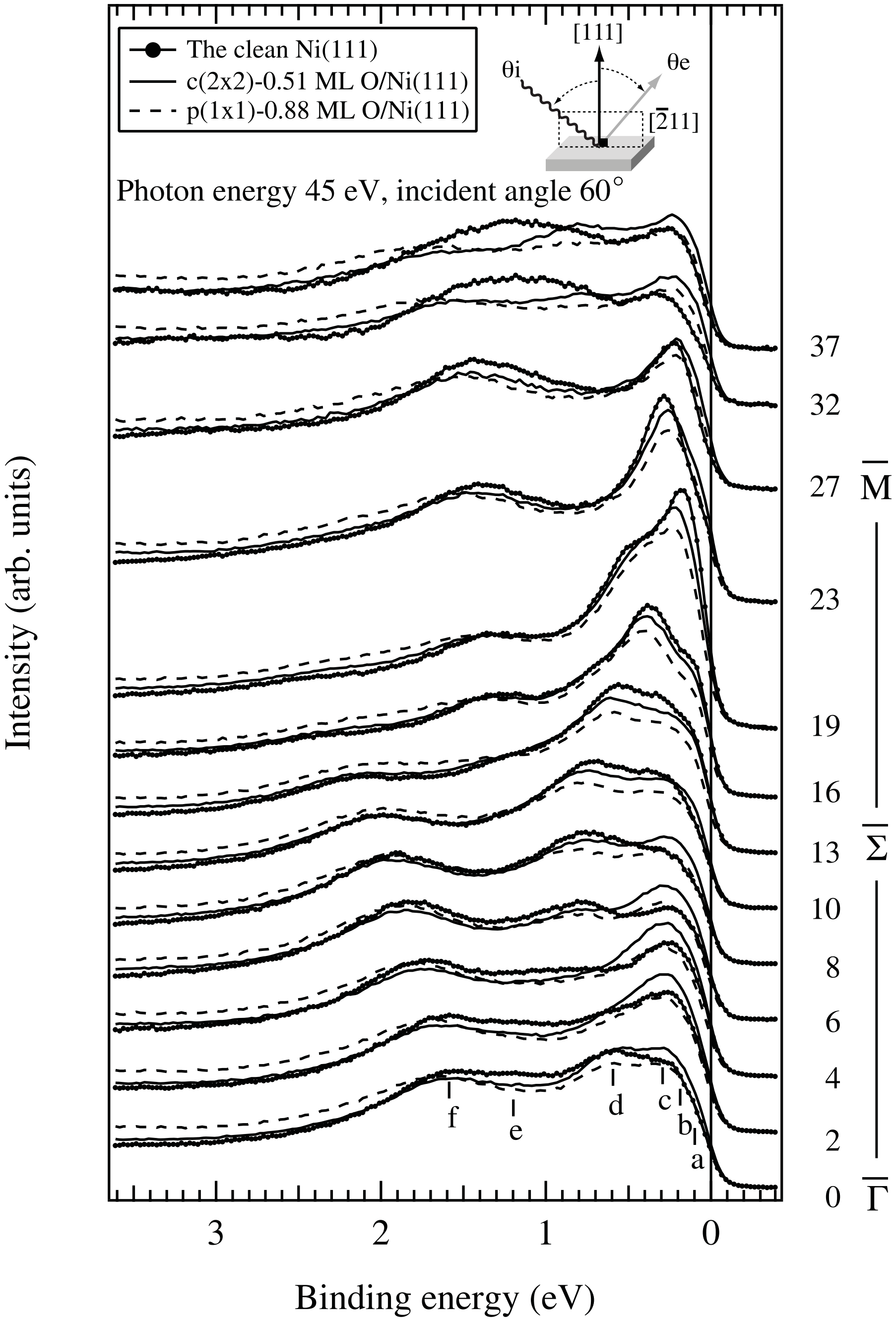

Fig. 3. ARPES spectra of the clean Ni(111), c(2×2)-0.51 ML O/Ni(111) and p(1×1)-0.88 ML O/Ni(111) surfaces along the $\overline{\Gamma}$-$\overline{\Sigma}$-$\overline{\mathrm{M}}$ direction. The geometry of ARPES measurement is also shown in the inset with incident angle of θ_i and emission angle of θ_e. Emission angle is indicated on the right-hand side of each spectrum. Tick markers in the normal-emission spectra correspond to the spectral features in Fig. 2.

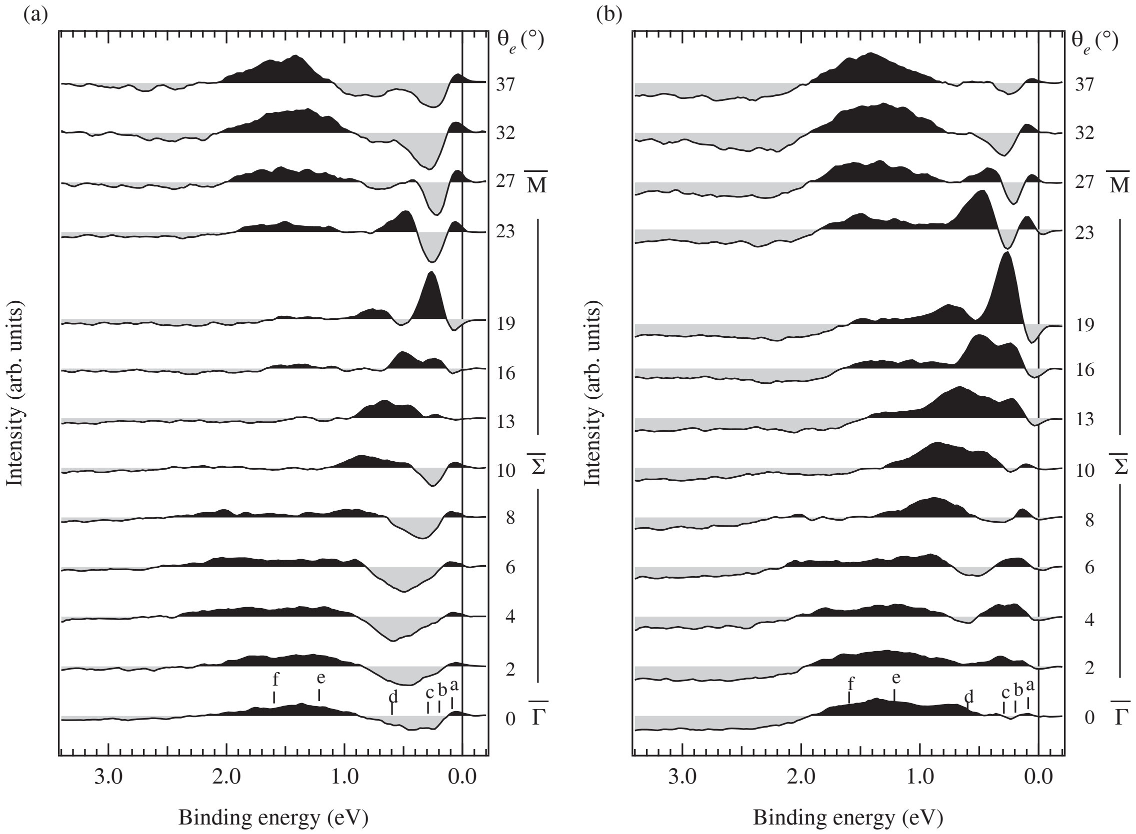

Fig. 4. Subtracted ARPES spectra of the (a) c(2×2)-0.51 ML and (b) p(1×1)-0.88 ML O/Ni(111) surfaces from that of the clean Ni(111) surface shown in Fig. 3. A positive area is filled with black, while negative area is filled with gray. Tick markers in the normal-emission spectra correspond to the spectral features in Fig. 2.

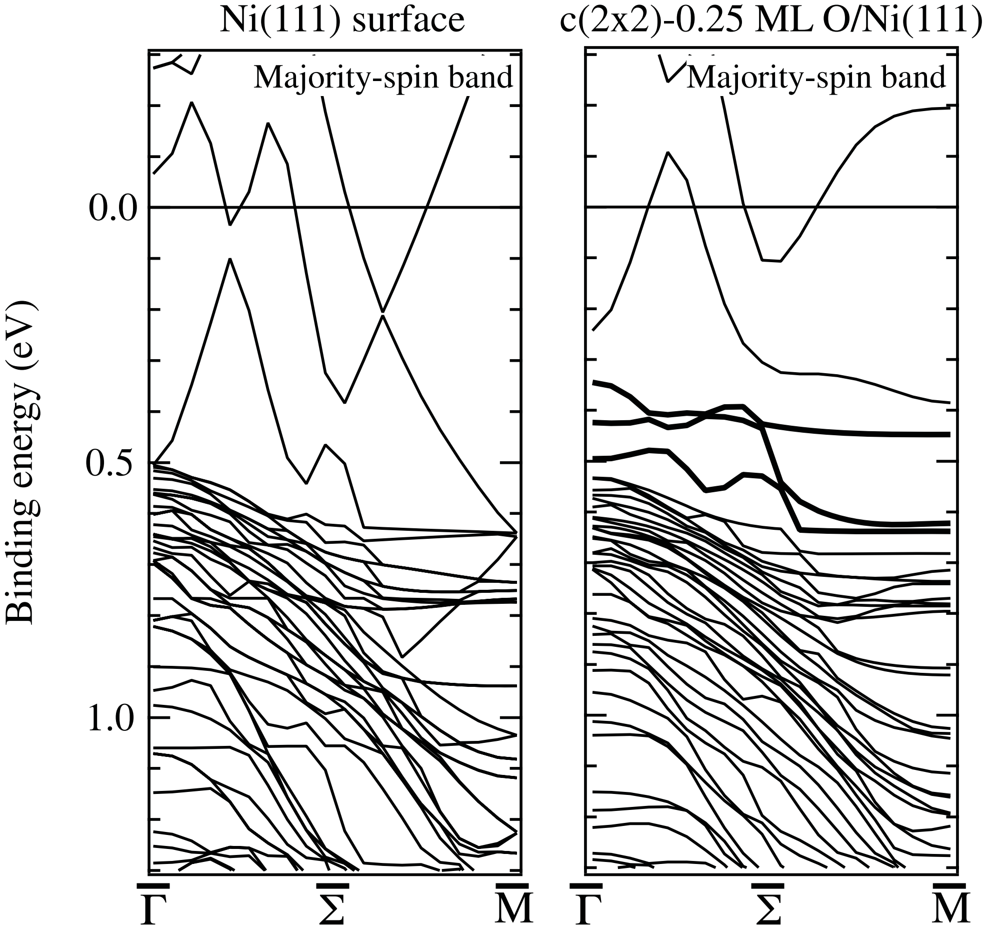

Fig. 5. First-principle energy-band dispersions on the clean Ni(111) and (2×2)-0.25 ML O/Ni(111) surfaces. Left figure represents the energy band on the clean Ni(111) surface and right figure the energy band on the c(2×2)-0.25 ML O/Ni(111) surface. Only majority-spin bands are shown in the figure.

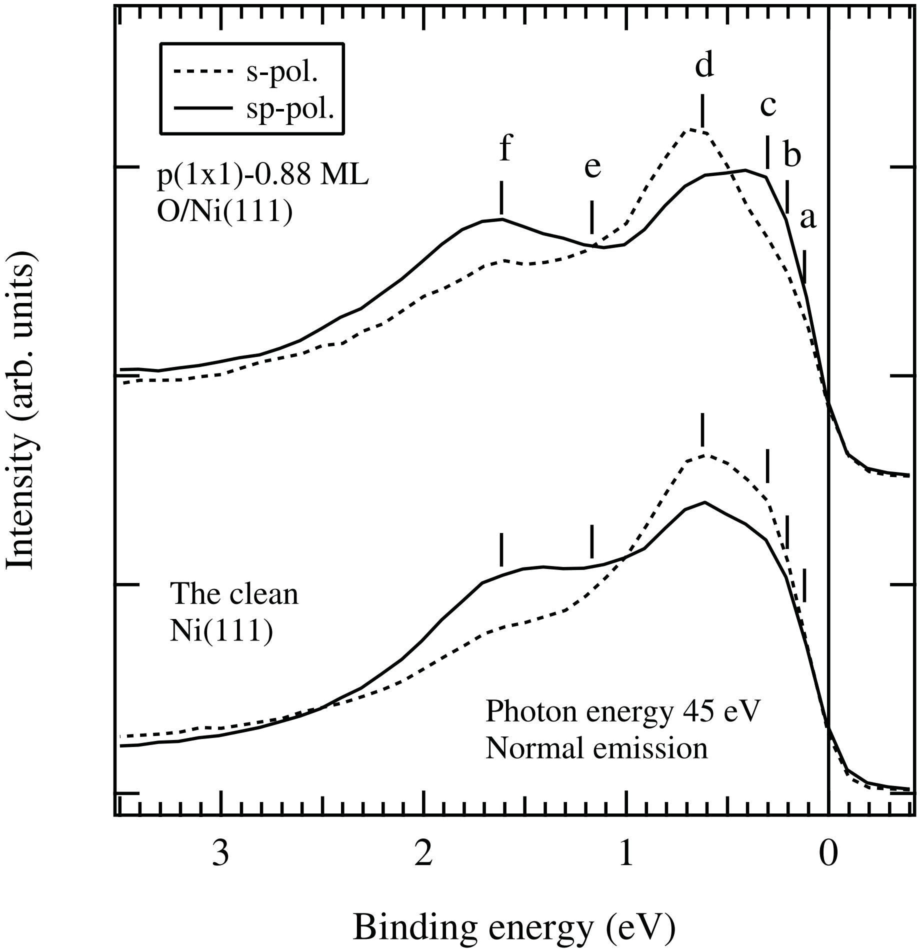

Fig. 6. Polarization dependence of ARPES spectra on the clean and p(1×1)-0.88 ML O/Ni(111) surfaces. The polarization was selected by changing angle of incidence of linearly polarized light on the Ni(111) surface. The incident angles at 20° and 60° correspond to s-polarization (dashed lines) and sp-polarization (solid lines), respectively. Tick markers correspond to the spectral features shown in Fig. 2.

CURRICULUM VITAE

FIRST NAME: MORAGOTE **LAST NAME:** BUDDHAKALA

GENDER: Male **NATIONALITY:** Thai

DATE OF BIRTH: Dec 02, 1965. **PLACE OF BIRTH:** Mahasarakham

EDUCATION BACKGROUND:

1994-1998	M.Sc. (Physics), Kasetsart University, Thailand.
1988-1991	B.Sc. (Physics), Ramkhamhaeng University, Thailand.

WORK EXPERIENCE:

1991-1992	A teacher in Science Programme, Payukkabhum Witthayakan School, Payukkabhum, Mahasarakham, Thailand.
1992-1999	Lecturer, Physics Program, Science Division, Rajamangala Institue of Technology, Tak campus, Thailand.
1999-2006	Lecturer, Department of Physics, Faculty of Science, Rajamangala University of Technology, Thanyaburi, Pathumtani Thailand.
2007-	Head of Department of Physics, Faculty of Science, Rajamangala University of Technology, Thanyaburi, Thailand.